SUB-SYNCHRONOUS RESONANCE

ANALYSIS AND DETECTION

By

IGOR BRANDÃO MACHADO MATSUO

DISSERTATION

Submitted in partial fulfillment of the requirements for the degree of

DOCTOR OF PHILOSOPHY IN ELECTRICAL ENGINEERING

THE UNIVERSITY OF TEXAS AT ARLINGTON

Arlington, Texas, USA

December 2019

SUB-SYNCHRONOUS RESONANCE

ANALYSIS AND DETECTION

By

IGOR BRANDÃO MACHADO MATSUO

DISSERTATION

Submitted in partial fulfillment of the requirements for the degree of

DOCTOR OF PHILOSOPHY IN ELECTRICAL ENGINEERING

Committee members:

Wei-Jen Lee, Ph.D. (Chair)
Ali Davoudi, Ph.D.
David Wetz, Ph.D.
Ramtin Madani, Ph.D.
Rasool Kenarangui, Ph.D.

THE UNIVERSITY OF TEXAS AT ARLINGTON

Arlington, Texas, USA

December 2019

“Be thankful for what you have;
you’ll end up having more.
If you concentrate on what you don’t have,
you will never, ever have enough.”

(Oprah Winfrey)

ABSTRACT

SUB-SYNCHRONOUS RESONANCE

ANALYSIS AND DETECTION

By

IGOR BRANDÃO MACHADO MATSUO, Ph.D.

THE UNIVERSITY OF TEXAS AT ARLINGTON

Supervising Professor: Wei-Jen Lee

With the increasing penetration of renewable generation resources, power grids have become more susceptible to sub-synchronous resonance phenomena, especially to sub-synchronous control interaction, which produces fast-growing oscillations. The power system operation requirements for a reliable, fast and accurate detection and monitoring system for protection and mitigation purposes are increasing. Besides, risk assessment analysis during grid planning and update studies can be extremely time-consuming due to a large number of possible grid configurations and small time-steps required for the simulation of detailed electromagnetic transient (EMT) models. The first part of this dissertation aims to provide an optimized tool for SSR risk assessment analysis based on frequency scanning that uses a multi-frequency signal to estimate the grid impedance at all frequencies with one simulation instead of one simulation per frequency of interest. The technique reduces the effects of nonlinearities normally present in power-electronic-based devices, is based on the harmonic injection method and can be used with black-box models. A case study based on the Texas synthetic grid and with two wind

farms and a VSC-based STATCOM was used for the validation of the proposed method, which showed superior accuracy than other studied techniques while being 11.71 times faster than multiple single-frequency injections. The second part of this dissertation provides an SSR detection system based on the power spectrum of the input signal plus frequency, magnitude, and derivative-of-magnitude estimators. All the signal conditioning techniques were also discussed and optimized to enable the detection system to efficiently and accurately work throughout the whole sub-synchronous range (5-55 Hz for a 60 Hz system). Finally, a complete monitoring system from data acquisition to data logging was implemented for the detection system in an FPGA-CPU heterogeneous platform and tested in real-time devices. The system provides several mechanisms to ensure its own reliable operation with several self-monitoring schemes and a health indicator in a dual modular redundancy scheme (primary and backup controller-units). A software-implemented voting scheme then decides which unit will forward all information to the subsystems that will use the output of the detection system. The Texas synthetic grid case was applied to the monitoring/detection system and the detection of sub-synchronous control interaction was observed with pickup times within 10 ms to 40 ms depending on the system disturbance.

ACKNOWLEDGMENTS

I thank the support of CNPq, National Council for Scientific and Technological Development – Brazil, for the full scholarship for the Ph.D. program.

I also thank my advisor, Dr. Wei-Jen Lee, for all directions and knowledge given, and my teammates at the University of Texas at Arlington, Fiacre Iragaba, Farshid Salehi, Long Zhao, and Yuhao Zhou, who were vital during my doctoral program.

Also thanks to all committee members, Dr. David Wetz, Dr. Ali Davoudi, Dr. Ramtin Madani, and Dr. Rasool Kenarangui.

Finally, I would like to express my gratitude to all members of the EE department of UTA, especially Gail Paniuski, who promptly assisted me so many times.

DEDICATION

This dissertation is especially dedicated to the memory of my mother, Maluh, who completely supported my pursuit for the doctoral degree, even if it meant we would be 5,000 miles apart. I also especially dedicate it to my father, Nelson, who is my inspiration in both my professional and personal lives.

Special thanks to my wife, Livia, who encouraged me and went through all the ups and downs with me on this path; and Marcel (brother), Eric (brother), Claire (niece), and Suzane (sister-in-law) who helped me in all things - great and small.

LIST OF FIGURES

LIST OF TABLES

LIST OF ACRONYMS

AC	Alternating Current
ASIC	Application Specific Integrated Circuit
CPU	Central Processing Unit
DFIG	Doubly-Fed Induction Generator
DMR	Dual-Modular Redundancy
DSP	Digital Signal Processing
DFT	Discrete Fourier Transform
EMT	Electromagnetic Transient
EMTP	Electromagnetic Transient Program
ENBW	Equivalent Noise Bandwidth
ERA	Eigensystem Realization Algorithm
FFT	Fast Fourier Transform
FIR	Finite Impulse Response
FPGA	Field-Programmable Gate Array
HDL	Hardware Description Language
HVDC	High-Voltage Direct-Current
IGBT	Insulated-Gate Bipolar Transistor
IGE	Induction Generator Effect
IIR	Infinite Impulse Response
ICMP	Internet Control Message Protocol
I/O	Input/Output
LCC	Line-Commutated Converter
LTI	Linear-Time Invariant
MAC	Multiply-Accumulate
MP	Matrix Pencil
MPPT	Maximum Power Point Tracking
RMS	Root-Mean Square
PLL	Phase-Locked Loop
PMSG	Permanent-Magnet Synchronous Generator
PMU	Phasor Measurement Unit

RTOS	Real-Time Operating System
SNR	Signal-to-Noise Ratio
SSCI	Sub-Synchronous Control Interaction
SSI	Sub-Synchronous Interaction
SSO	Sub-Synchronous Oscillation
SSR	Sub-Synchronous Resonance
SSTI	Sub-Synchronous Torsional Interaction
STATCOM	Static Synchronous Compensator
SVC	Static VAR Compensator
SVD	Single Value Decomposition
TA	Torque Amplification
TI	Torsional Interaction
TMR	Triple-Modular Redundancy
VSC	Voltage-Source Converter
WAMS	Wide-Area Measurement System
WPP	Wind Power Plant
WTG	Wind Turbine Generator

Table of contents

1 INTRODUCTION

1.1 Background and motivation

Historically, several technologies have been used to increase the efficiency of power system operation. One such technology involves series-compensated lines, which are still widely used to increase the power transfer capability of transmission lines, as well as to improve system stability, voltage regulation, and load flow in parallel lines. Another example involves high-voltage direct-current (HVDC) lines, which not only provide lower losses than alternating-current (AC) lines when transmitting power over long distances, but also require one less conductor, improve system controllability, limit short-circuit currents, and make asynchronous connections possible. The electrical system of these two technologies, however, may interact with the mechanical system of nearby conventional turbine-generators (usually from thermal power plants). These interactions may result in oscillations below the synchronous frequency (60Hz or 50Hz, depending on the system), generating a phenomenon known as sub-synchronous resonance (SSR), in particular sub-synchronous resonance torsional interaction (SSR TI), when it involves series-compensated lines, and sub-synchronous torsional interaction (SSTI), when it involves HVDC lines.

Currently, with the advancement of power electronic-based devices and increased penetration of renewable generation resources, the dynamic behavior of electrical grids has substantially changed. A phenomenon called sub-synchronous control interaction (SSCI) has become a great concern. SSCI consists of an interaction below the synchronous frequency between an electrical grid and a power electronic-based control system, especially such as the ones in wind farms, but also including HVDC links and static VAR compensators (SVC), among others. This is a purely electrical phenomenon, which means no mechanical interaction is involved, making it potentially much faster than torsional interaction.

Other terms defining the interaction between two or more elements of a power grid that leads to sub-synchronous oscillations (SSO) are used in literature, such as sub-synchronous interaction (SSI), and industrial and research institutions have not reached unanimity regarding the terminology. The details of the terminology used herein are described in the next chapter.

The two first known SSI events took place in Nevada, in 1970 and 1971, and were a mechanical-electrical phenomenon. Among other events, the first purely electrical phenomenon occurred in a wind farm in Texas, in 2009. This event drastically drew the attention of researchers and power grid operators not only in the USA but all over the world.

With the increased concerns about SSR in existing and in new electrical grids, power system operators worldwide, such as the independent system operators (ISO) in the USA, have been establishing protocols and methodologies to assess the vulnerability of grids to SSR phenomena, as well as enforcing study requirements in many situations, such as in some existing grids, new generation resource interconnections, and new transmission line connections. Moreover, several generation companies, transmission companies, and industries have been installing monitoring and/or protection/mitigation systems for sub-synchronous oscillations. However, there is still a great need for efficient and accurate tools to assess the risks of SSR in power grids, especially when we take into account that several grid configurations must be studied, which can result in extremely large amounts of analysis/simulation time. Besides, the real-time operation of the power system needs fast and accurate SSR monitoring and detection mechanisms for protection/mitigation purposes, especially if SSCI is involved, which can cause extremely fast-growing oscillations.

This research aims to provide a risk assessment tool to aid in the vulnerability assessment of power grids in terms of SSR phenomena in a time-efficient manner while maintaining high accuracy. Also, it develops and implements a detection system and a real-time monitoring system that can be used for protection, mitigation, and post-event analysis and that takes into account signal conditioning and the high-speed requirements when SSCI phenomena are involved.

1.2 Past sub-synchronous resonance events

The first time a sub-synchronous-resonance type of phenomenon was treated in literature was in 1937. However, the first event registered in literature occurred only in 1970, when the topic started to receive more attention. In 2009, when a different type of interaction occurred for the first time, it not only became a subject of attention of researchers again, but electric utilities, industries, and electrical system operators made it

of high concern and part of the protocols of generation and transmission planning. The main events registered in literature are briefly described in the following sub-items. The types of sub-synchronous interactions will be mentioned, but the details about each type will be presented in the next chapter.

1.2.1 SSR TI events

The first events reported in literature took place in Nevada, USA at the Mohave coal-fired power plant in 1970 and 1971. The incidents involved the interaction between a turbine-generator mechanical system and a series-compensated transmission system in a phenomenon called sub-synchronous resonance torsional interaction (SSR TI). Natural modes of the electrical system triggered mechanical modes of the generator shaft, subsequently leading to sub-synchronous currents (around 30Hz in the last case) that resulted in the breakdown of the insulation between the shaft and the collector rings of the generator [1].

1.2.2 SSTI events

In 1977, another phenomenon called sub-synchronous torsional interaction (SSTI) occurred in North Dakota, USA. Sub-synchronous oscillations of 11.5 Hz were observed during commissioning tests of a line-commutated-converter HVDC (LCC-HVDC) line that interacted with a turbine-generator (Square-Butte, in the Milton R. Young power plant). This case was then studied and the necessary modifications were made to the control system of the HVDC terminal, resulting in stable operation in subsequent tests before being put into operation [2].

Several sub-synchronous oscillations were captured by wide-area measurement systems (WAMS) in north China between 2014 and 2015. This area has a growing installed capacity of wind generation but no series-compensated networks are nearby. Also, the wind power plants (WPP) in which the oscillations were captured use direct-drive permanent-magnet synchronous generators (PMSG). These two facts remove the possibility of being an SSCI type of interaction despite the involvement of wind farms. The area is also known to have LCC-HVDC lines. Studies show that sub-synchronous torsional interaction (SSTI) may be the cause of these oscillations, although these are not

yet totally conclusive due to the involvement of PMSGs, a type of generator that previous studies had indicated that was not susceptible to sub-synchronous interaction [12].

1.2.3 SSCI events

In 2009, the first sub-synchronous control interaction (SSCI) event took place in a wind farm in Texas (ERCOT system), USA. The incident involved interaction between doubly-fed induction generators (DFIG) and a 50%-series-compensated line. Oscillations of around 20 Hz damaged the crowbar protection of several DFIGs in an estimated time of only 200 ms, when the system voltage exceeded 2 pu. Only after the voltage reached 2 pu that the series capacitor was bypassed, making the sub-synchronous currents subside. However, the currents reached over 300% of its normal levels within 400 ms of the event.

Conventional overcurrent relays are not able to protect against this type of event. If we take a digital overcurrent relay, it normally uses RMS (root-mean-square) values (usually true RMS) calculated over a cycle or half-cycle of the fundamental frequency (e.g., 32 samples with a sampling rate of 1920 Hz). Low frequencies in the calculation make the RMS value increase and decrease continuously when using only this limited number of samples, consequently making the overcurrent protection pick up and drop off repeatedly for not staying long enough to trip according to its time-current curve.

This phenomenon was the first purely-electrical type of sub-synchronous interaction and raised concerns all over the world as a fast-growing event that requires special monitoring, protection, and mitigation systems. These concerns also brought an increased need for special risk assessment tools. Such tools are required to accurately represent the highly nonlinear behavior of the control systems of DFIGs, which respond very rapidly to perturbations in the electrical system [3]-[5].

In 2010, Oklahoma Gas & Electric phasor measurement units (PMU) recorded several oscillations of 12.44 Hz and 13.33 Hz in a wind farm. It was observed that higher power outputs (above 80% of the wind farm installed capacity) were a common feature among all events [6]-[7].

Oscillations between 9 Hz and 13 Hz were also observed in the Buffalo Ridge area of Minnesota during commissioning tests of the series capacitor when one line was taken out of service, leaving a 150 MW wind farm with output of 15 MW in radial condition with a 60%-series-compensated line [8]-[9], [15].

Between December of 2012 and December of 2013, as many as 58 oscillations ranging from 6 Hz to 8 Hz occurred in the Guyuan wind power system of the Hebei province, in China, where wind farms are located [10]-[11]. The events occurred mostly when wind speeds were low and wind farm outputs were low (<10% of capacity).

To the time of writing this document, the most recent events occurred in Texas (ERCOT system), USA in 2017. Different episodes were recorded and oscillations ranging from 22 Hz to 27 Hz were captured. The incidents involved wind farms and series-compensated lines, leading to the conclusion that they were an SSCI type of interaction. Different from the 2009 event, specific actions of the protective relays and mitigation system were confirmed, which resulted in no damage to wind generators neither series capacitors in the network [13].

1.3 Dissertation structure

This first chapter provided the motivation and some background information regarding past events of SSR. Chapter 2 provides theoretical background about the different types of SSR as well as of risk assessment analysis methods and possible applications for SSR monitoring systems (protection, mitigation and post-event analysis). Chapter 3 takes the frequency scanning method to propose an optimized tool that reduces simulation time by a factor of 10 while reducing the error of the impedance estimation of the grid in the presence of several nonlinearities. Chapter 4 presents a complete SSR detection scheme for monitoring systems that can be used for protection, mitigation, and post-event analysis, including a discussion about processing technologies; data acquisition; signal conditioning techniques; the matrix pencil detection algorithm; a proposed detection algorithm based on the power spectrum of the input signal and frequency/magnitude and derivative estimators; output post-processing techniques; and field implementation considerations. Chapter 5 is an extension of chapter 4, but focusing on a redundant mechanism created to improve the reliability of the monitoring system by using two real-time devices with several mechanisms that ensure the continuation of service and lossless data in case of technical issues in one of them. Chapter 6 validates the redundant mechanisms of the monitoring system and applies a case study based on the Texas synthetic grid to the SSR detection system in an implementation using real-

time devices. The system demonstrates very good accuracy in an extremely fast detection within 10 ms to 40 ms depending on the system disturbance. Proper signal conditioning and filtering techniques showed to be as important as the detection system itself. The speed of detection could be higher or lower, being a tradeoff with the required accuracy, which depends on the system application – protection, mitigation, or post-event analysis (in the descending order of speed requirements and ascending order of accuracy requirements). This chapter also applied the developed optimized frequency scanning tool to the Texas case and the simulation time was proved to be greatly reduced while accuracy was higher than other studied techniques. Chapter 7 finalizes the dissertation with the conclusion and future work possibilities. After chapter 7, a list of publications during the doctoral program is presented.

2 SUB-SYNCHRONOUS RESONANCE

Industrial and research institutions are not unanimous about the terminology regarding sub-synchronous resonance (SSR) phenomena. Sub-synchronous resonance has been defined as “a condition where a series-capacitor-compensated system exchanges significant energy with a turbine-generator at a frequency below the synchronous frequency”, and has been often used as a general term for the interaction that involves series-compensated transmission lines [14]. It is historically associated with conventional synchronous machines (e.g., thermal units) but is also possible with other types of generation resources, such as wind turbine generators (WTG) [15]. Currently, this term is also frequently used to indicate what is called sub-synchronous interaction (SSI), which has been defined as the energy exchange between two parts of an electric system at one or more of the natural frequencies of the combined system below the fundamental frequency [3]. An also very common denomination is sub-synchronous oscillations (SSO). IEEE defines SSO as an energy exchange between an electric network and a turbine-generator at one or more of the natural frequencies of the combined system below the synchronous frequency of the system after a disturbance from an equilibrium point [16]. However, this definition became out-of-date as other types of interactions were discovered to produce oscillations in the sub-synchronous range. Nowadays, these terms are often used interchangeably for any type of interaction, but some prefer to refer to SSO as the oscillations resulted from SSI. Furthermore, a good part of the industry considers all kinds of interactions as a resonance between two parts of a system, using SSR to refer to any type of SSI, which is the definition followed by this text.

2.1 Classification

While extensive research is still being performed about the possibilities of interaction that are not registered in literature or with no actual events, a few main types of sub-synchronous interaction are currently defined [15], [17].

2.1.1 Sub-synchronous resonance torsional interaction (SSR TI)

A series-compensated network with a turbine-generator set is shown in Fig. 2.1.

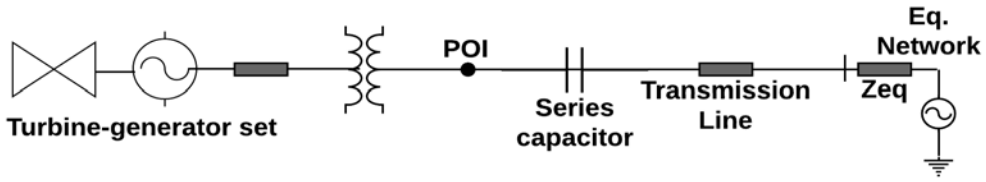

Fig. 2.1: Series-compensated network with a turbine-generator set.

The electrical resonance frequency of the network is:

$$f_{el.res} = f_s \sqrt{\frac{x_c}{x_{\Sigma \mathrm{L}}}} \tag{2-1}$$

$$x_{\Sigma \mathrm{L}} = x_G'' + x_{\mathrm{T}} + x_{\mathrm{l}} + x_{\mathrm{eq}} \tag{2-2}$$

where:

$f_{el.res}$: electrical resonance frequency

f_s: system synchronous frequency (60 Hz or 50 Hz, depending on the system)

x_c: reactance of the series capacitor

$x_{\Sigma \mathrm{L}}$: sum of series reactances

x_G'': sub-transient reactance of the generator

x_{T}: leakage reactance of the transformer

x_{l}: reactance of the transmission line

x_{eq}: reactance of the equivalent system

The degree of compensation k_C is defined in terms of the transmission line parameters and usually ranges from 25% to 75%.

$$k_C = \frac{x_c}{x_{\mathrm{l}}}\ 100\% \tag{2-3}$$

Disturbances in the grid excite transient currents flowing in the generator stator at frequencies $\pm f_{el.res}$, which are reflected in the stator flux at the sub-synchronous frequency $f_{el.res}$. Subsequently, the rotor winding currents will have modulated frequencies of:

$$f_{rotor.el.res} = f_r \pm f_{el.res} \tag{2-4}$$

where the rotor DC flux rotates at a frequency f_r, meaning:

f_r: rotor electrical frequency

Torsional interaction involves both the mechanical system of a turbine-generator set and the electrical system of a series-compensated network. The shaft of the mechanical system has natural torsional frequencies f_{nat}. Power system perturbations can create oscillations at this mechanical natural frequency, which will reflect from the rotor to the stator producing voltage components at the generator terminals with frequencies in the sub-synchronous and super-synchronous range, as follows:

$$f_{stator.mec.res} = f_r \pm f_{nat} \tag{2-5}$$

Using equation (2-5), if the sub-synchronous component of $f_{stator.mec.res}$ coincides or is close to the electrical resonance frequency $f_{el.res}$ of the grid, the torque produced will excite the shaft at its torsional natural mode. We can reach the same conclusion from equation (2-4). If the sub-synchronous component of $f_{rotor.el.res}$ coincides or is close to the mechanical resonance frequency f_{nat} of the shaft, torsional interaction will occur between the mechanical and electrical systems.

If the torque produced at these sub-synchronous frequencies is greater than the inherent mechanical damping of the rotor, the torsional interaction will become self-sustained, leading to growing oscillations which can result in shaft fatigue or failure.

SSR TI is more common in thermal power plants, in which the inertias of the turbine and of the generator are close. Hydroelectric power plants are not prone to this phenomenon because the inertia of the turbine is around only 5% of the inertia of the generator [18]. Torsional oscillations will produce speed variations mostly in the turbine while the generator shaft will be almost not affected. Wind turbines, on the other hand, are at risk of SSR TI with many torsional modes related to the blades, shaft, gearbox, tower, etc [15]. Nevertheless, these modes are generally at low frequencies due to the soft nature of the shaft, therefore requiring very high degrees of series compensation to trigger

them. Additionally, the damping values of the torsional modes are unresponsive to wind speed variations [19]-[20].

2.1.2 Sub-synchronous resonance torque amplification (SSR TA)

While SSR TI is caused by small disturbances that resonate with the mechanical modes of the turbine-generator set, SSR TA is a result of large disturbances, such as faults or switching operations. When the system is not compensated, the abrupt changes in the current usually result in, aside from the AC component at the fundamental frequency, a DC component. However, in series-compensated systems, they also result in oscillations at the resonant frequency $f_{el.res}$ of the grid. If the frequency of the torque created in the shaft by this oscillation is close to one of its natural frequencies, large transient torques proportional to the magnitude of the current oscillation will be produced.

While SSR TI may be considered a dynamic-stability type of phenomenon produced by small disturbance signals and being usually analyzed using linear models, SSR TA is considered a transient phenomenon in which the inherent damping of the mechanical shaft does not have a major role anymore. The latter phenomenon requires nonlinear models and a small-signal analysis is not possible in this case. Electromechanical and electromagnetic transient models are necessary.

As an example, series-compensated systems usually bypass the capacitor during a fault. When the fault is cleared and the capacitor is re-inserted, large disturbances may occur with this switching operation. The disturbances may trigger resonant modes of the system that contains a capacitor, subsequently leading to sub-synchronous oscillations.

2.1.3 Sub-synchronous resonance induction generator effect (SSR IGE)

SSR IGE is an electrical effect between a series-compensated network and a generator. It does not involve the mechanical system, so the associated inertia does not influence the phenomenon, making its occurrence possible in not only thermal and wind units, but also hydro units.

We know that, at the synchronous frequency, a synchronous generator has a slip of zero, as the difference between the synchronous speed and the rotor speed is zero. However, in the sub-synchronous range, the stator flux has a frequency component $f_{el.res}$ - the electrical resonance frequency of the network - which now is not the same as the

rotor electrical frequency, f_r. Hence, not only induction generators but also synchronous generators act as asynchronous machines at the sub-synchronous range. The sub-synchronous slip is given by:

$$s_{SSR} = \frac{f_{el.res} - f_r}{f_{el.res}} \tag{2-6}$$

The steady-state equivalent circuit of an asynchronous machine viewed from the stator terminals is shown in Fig. 2.2.

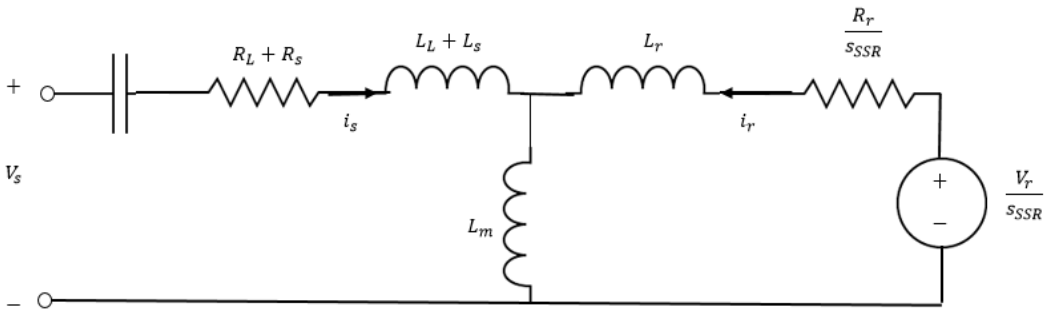

Fig. 2.2: Equivalent circuit of an asynchronous machine viewed from the stator terminals.

The equivalent rotor resistance is given by:

$$R_{r,eq} = \frac{R_r}{s_{SSR}} \tag{2-7}$$

In series-compensated networks, the following condition is normally true:

$$f_{el.res} < f_r \rightarrow s_{SSR} < 0 \tag{2-8}$$

Hence, from equation (2-7) and condition (2-8):

$$R_{r,eq} < 0 \tag{2-9}$$

Equation (2-9) shows that the equivalent rotor resistance is negative at the sub-synchronous resonant frequency. If its magnitude is greater than the summation of the stator and network resistances, the overall resistance will be negative. This results in negative damping at this frequency, which can result in self-excited increasing oscillatory voltages and currents, commonly known as IGE.

Analyzing all equations above, when the degree of compensation k_C increases, the electrical resonance frequency $f_{el.res}$ also increases. Therefore, the absolute value of the slip s_{SSR} – which is negative - is reduced. This leads to a higher magnitude of the negative equivalent rotor resistance $R_{r,eq}$ and, consequently, reduced damping of oscillations.

Additionally, if we analyze a DFIG wind turbine (type-3 wind turbine), when the wind speed gets higher, the aerodynamic behavior of the wind turbine leads to a higher torque, which in turn leads to a higher optimal rotor electrical frequency, f_r. Therefore, the absolute value of the slip s_{SSR} – which is negative - is increased. This leads to a lower magnitude of the negative equivalent rotor resistance $R_{r,eq}$ and, consequently, increased damping of oscillations. The optimal rotor electrical frequency is achieved assuming: 1) simple slip control for the rotor voltage based on a lookup table; 2) disabled rotor-side controller, which implicates that the DFIG is not influenced by the fast action of this controller (the rotor-side controller action is considered part of the SSCI phenomenon, detailed in a subsequent section of this chapter). An example of a wind turbine at a fixed pitch angle condition is given in Table 2.1 in the form of a lookup table that associates the wind speed with the rotor shaft speed, the power output, and the associated torque. In reality, the optimal rotor speed is achieved by using a torque control loop (or rotor speed control loop) with a maximum power point tracking (MPPT) algorithm [10], [19]. The MPPT aims to provide the reference torque (or reference wind speed) to achieve maximum power output according to the lookup table. Now, for the case of a traditional squirrel-cage induction generator, which is considered a fixed-speed wind turbine (type-1), the wind speed does not affect the rotor speed, which means the damping is not influenced by wind speed variations.

Table 2.1: Lookup table: wind speed, rotor shaft speed, power output, and torque [19].

v_{wind}	$7\ m/s$	$8\ m/s$	$9\ m/s$	$10\ m/s$	$11\ m/s$	$12\ m/s$
ω_m	0.75	0.85	0.95	1.05	1.15	1.25
P_m	0.32	0.49	0.69	0.95	1.25	1.60
$T_m = \frac{P_m}{\omega_m}$	0.43	0.58	0.73	0.90	1.09	1.28

2.1.4 Sub-synchronous torsional interaction (SSTI)

SSTI involves an interaction between turbine-generators and power electronic-based devices. Such devices may include HVDC converters, static VAR compensators,

power system stabilizers, electro-hydraulic speed governors (not conventional ones), and other FACTS devices.

Take the case of an interaction between a turbine-generator set and an HVDC controller. As mentioned earlier, turbine-generator sets have natural mechanical modes. These modes produce slight variations in the speed of the generator, which leads to variations in the terminal voltages and, consequently, in the currents at the HVDC terminals. The fast response of the HVDC converters leads to voltage/current variations in the DC link, which in turn produce an electrical torque variation of the generator, making it a closed-loop control interaction [21]. From this example, it is possible to see that power variations may contribute to negative damping at the sub-synchronous range due to the fast action of power-electronic-based devices, which may cause undamped oscillations.

2.1.5 Sub-synchronous control interaction (SSCI)

SSCI is the interaction between a series-compensated network and a power-electronic-based device. This phenomenon is only electrical in nature, so there is no mechanical system and associated inertias or natural modes involved. The resulting oscillations can grow very quickly and the resonant frequencies are not fixed, being dependent on the system conditions and type of controllers and associated settings. This means that the frequencies and impedances associated with the resonant modes are not fixed and may vary with different controller parameters, as well as with different power flows in the controllers and voltage levels, etc. Equations (2-6) to (2-9), used to explain the IGE phenomenon, are also valid for SSCI. Current literature has not completely reached an agreement about the differences between the SSCI and IGE phenomena. While some claim that SSCI is a special case of the IGE phenomenon applied only to asynchronous machines, and not also to synchronous machines, others prefer to distinguish them so as to apply the effect of the power-electronic devices solely for the SSCI phenomenon [15], [17], [20].

2.1.5.1 Doubly-fed induction generator (DFIG)-based wind turbine

Take the DFIG connected to a series-compensated network shown in Fig. 2.3. The rotor-side converter (RSC) and the grid-side converter (GSC) are shown in Fig. 2.4 and Fig. 2.5, respectively, being modeled as cascaded loops and based on reference [19], from

which the interested reader can obtain more detailed information on modeling of DFIG-based wind farms for SSR analysis, along with reference [10]. Both converters have two outer loops (left side of figures) and the inner loops (right side of figures), the latter being called current-tracking control loops herein, which generate the output voltages in *d*-*q* reference frames. The reference currents for the inner loop are provided by the outputs of the outer loop of each controller.

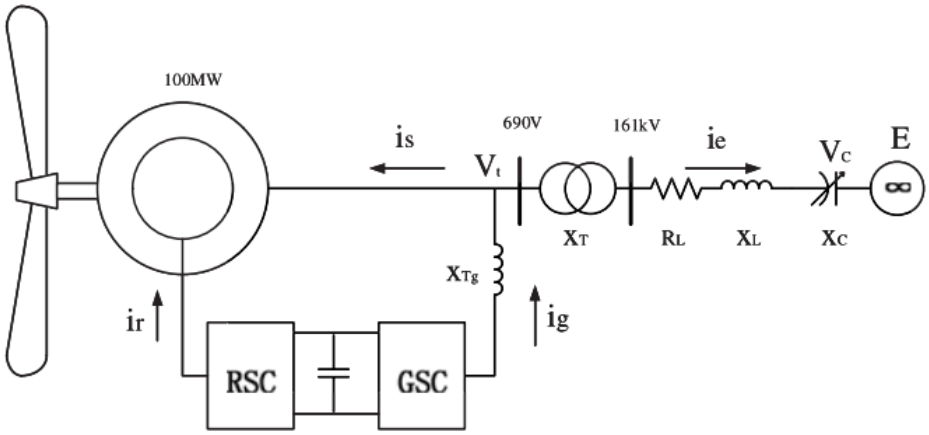

Fig. 2.3: DFIG connected to a series-compensated network (source of figure: [19] © 2010 IEEE).

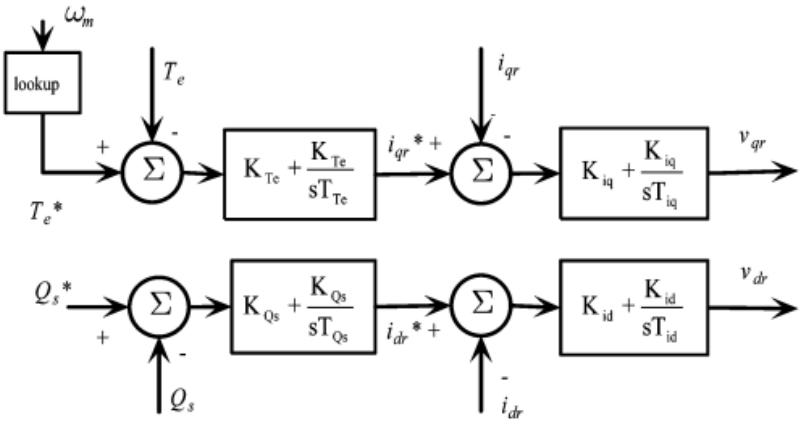

Fig. 2.4: Rotor-side converter (RSC) control loops (source of figure: [19] © 2010 IEEE).

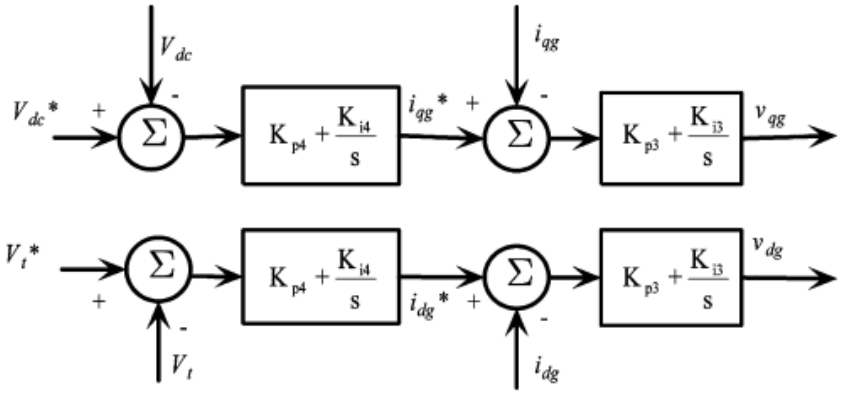

Fig. 2.5: Grid-side converter (GSC) control loops (source of figure: [19] © 2010 IEEE).

The RSC has two outer loops, namely rotor-speed control loop and reactive-power control loop. In the rotor-speed control loop, the reference rotor electrical speed w_m is obtained as described in the IGE sub-section, in which an MPPT algorithm uses a lookup table, such as the one in Table 2.1, provided for different pitch angles, and searches for the optimal reference rotor speed to deliver maximum power output. However, in this case, the converters are acting to achieve optimal rotor electrical frequency through the RSC rotor voltage outputs. In the reactive power control loop, the reactive power reference Q_s^* is usually set to zero to maintain the power factor at the generator terminals at unity.

The GSC also has two outer loops, namely DC-voltage control loop and stator-voltage control loop. These loops have the purpose of maintaining the DC-link voltage and the generator terminal voltages at their rated values, respectively.

For the interested reader, more details of DFIG models for sub-synchronous interaction analysis, including modeling of pitch angle control, DC-link between GSC and RSC, wind turbine aerodynamics, torsional dynamics, and aggregated models can be found in [10], [19], [20], [22], [23], [24].

2.1.5.2 SSCI in a doubly-fed induction generator (DFIG)-based wind turbine

While traditional IGE analyses are usually performed in terms of different series-compensation levels and wind speeds assuming no influence of the fast response of the converters, SSCI also takes into account the action of these converters.

Regarding the risks of SSCI, the GSC has a positive resistance influence (there is no effect of a slip variable, which is negative in the RSC in the sub-synchronous range),

therefore increasing the damping of oscillations. On the other side, the action of the RSC loops may lead to increased magnitude of the effective rotor resistance [10]. From equations (2-7) and (2-9), one should easily conclude that this leads to a larger negative resistance and consequently reduced damping of oscillations. To better understand this phenomenon, take Fig. 2.4 and consider the proportional gain of the proportional-integer (PI) controller in the current-tracking control inner loops. Assuming that the reference currents provided by the outer loops are constant during a disturbance Δ_{i2} in the rotor currents, the output voltage is:

$$\Delta_{\boldsymbol{vr}} = -\boldsymbol{K_{pr,ctc}}\,\Delta_{\boldsymbol{ir}} + \Delta_{\boldsymbol{vrc}} \tag{2-10}$$

where:

$\Delta_{\boldsymbol{vr}} = [\Delta_{vr,d}\ \Delta_{vr,q}]^{\mathrm{T}}$: RSC output voltages

$\boldsymbol{K_{pr,ctc}} = [K_{i,d}\ K_{i,q}]$: proportional gains of the RSC current-tracking control loops

$\Delta_{\boldsymbol{vrc}} = [\Delta_{vrc,d}\ \Delta_{vrc,q}]^{\mathrm{T}}$: disturbances due to other controller characteristics

From equation (2-10), we can see that the term $-\boldsymbol{K_{pr,ctc}} * \Delta_{\boldsymbol{ir}}$ is a voltage drop and therefore $\boldsymbol{K_{pr,ctc}}$ has the same mathematical effect of a resistance. Fig. 2.2 then becomes Fig. 2.6 with the additional voltage drop due to the effect of the proportional gain of the RSC, which plays a major role in the SSCI phenomenon.

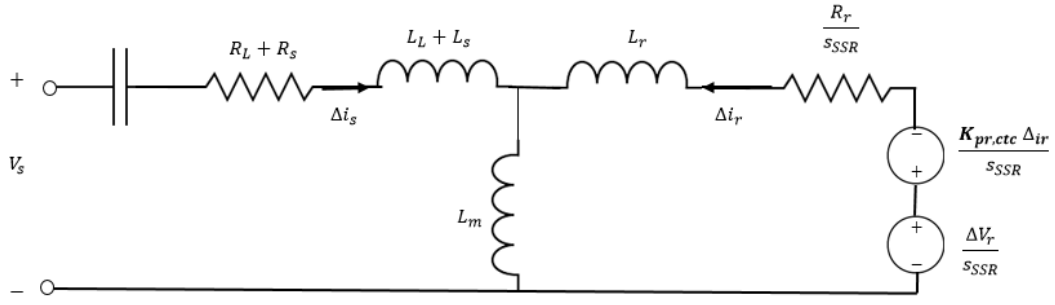

Fig. 2.6: Equivalent circuit of an asynchronous machine viewed from the stator terminals including the voltage drop due to the effect of the proportional gain of the RSC.

The equivalent rotor resistance can then be represented as in equation (2-11), which is equivalent to the representation shown in Fig. 2.7:

$$R_{r,eq} = \frac{\boldsymbol{K_{pr,ctc}} + R_r}{s_{SSR}} \tag{2-11}$$

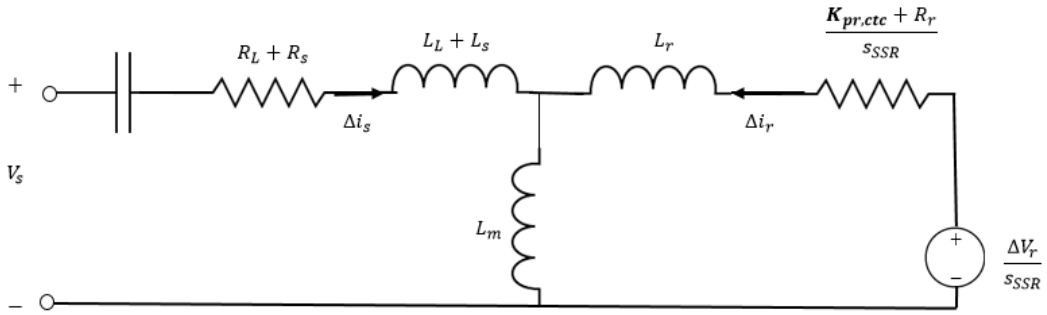

Fig. 2.7: Equivalent circuit of an asynchronous machine viewed from the stator terminals including the voltage drop due to the effect of the proportional gain of the RSC seen as an equivalent rotor resistance.

While equation (2-7) and Fig. 2.2 represent the rotor equivalent resistance for the IGE phenomenon, equation (2-11) and Fig. 2.7 are the representation for the SSCI phenomenon, now with the action of the converters taken into account. All proportional gains in the RSC have similar effects, which is: the higher the gains, the higher the magnitude of the equivalent resistance, which means a larger negative resistance and consequent less damping capability. Finally, the effects of variation in the wind speed and degrees of compensation are similar to the ones explained in the IGE section.

2.2 SSR analysis methods

In order to assess the susceptibility of electrical grids to sub-synchronous interaction and its intensities, several methods can be used. The main techniques, namely time-domain analysis and frequency scanning, and some other methods are described in the following sub-items [17].

2.2.1 Time-domain analysis

The time-domain analysis is the main technique used for detailed sub-synchronous interaction analysis. Electromagnetic transient (EMT) models with a detailed and full three-phase representation of all necessary components of the system are included. This includes the differential equations of machines; transmission/distribution lines; controllers of generators and power-electronic devices; bypass circuits of series capacitors and controllers; other nonlinear devices; etc. Either software with electromagnetic transient programs (EMTP) or with detailed representation of the nonlinear equations is necessary, which means conventional steady-state, dynamic, and

transient stability programs are not appropriate, these being commonly used for voltage stability, power flow, and short-circuit analysis, among others. The software must also be able to represent electromechanical systems for SSR phenomena that include torsional modes. PSCAD/EMTDC, MATLAB/Simulink, and EMTP-RV are examples of software with such capabilities.

The SSCI and SSTI phenomena require more detailed models for a correct and accurate analysis of the system behavior. The controllers associated with power electronic-based devices have fast switching action, often reaching thousands of Hertz. Moreover, simulations need to be run using very small time steps. Take a controller that uses an insulated-gate bipolar transistor (IGBT) with a switching frequency of 5 kHz. This means that every switching action takes 200 μs to complete. In order to accurately observe the IGBT behavior in the system, time steps much smaller than 200 μs must be used, for example, 5μs (also note that the switching period should be a multiple of the time step for an accurate simulation. In this case, 200 μs is a multiple of 5 μs). Simulations with such small time steps can be very time-consuming. Therefore, time-domain analysis is normally used only for the cases in which detailed analysis is necessary. Preliminary studies employing other techniques are usually carried out to select these cases.

2.2.2 Frequency scanning

Frequency scanning is the main technique for preliminary studies and can be used to assess all types of SSR phenomena. It consists of obtaining the frequency response in terms of impedance from a point behind the generator looking into the grid. This is equivalent to getting the equivalent impedance of the complete grid (including generator impedances) in various frequencies of interest. The point at which the reactance curve crosses the frequency axis indicates a zero reactance, if there is such crossover. The frequency at that point is a sub-synchronous frequency. If the resistance curve shows a negative value at that same frequency, the grid is prone to undamped, therefore unstable, sub-synchronous oscillations.

Systems operators and electrical agencies worldwide are making it mandatory to frequency-scan electrical grids using extremely deep contingency criteria that results in a radial condition between a generation resource and a series-compensated line, reaching N-14 (i.e., 14 concurrent outages) in the Texas ERCOT ISO, for example [25]. This is

due to the severity of oscillations and extreme damage and losses of equipment that may be incurred. Very deep contingency criteria result in an extremely high number of grid configurations. Therefore, performing complete detailed EMT simulations for each configuration is infeasible. The frequency scanning method provides a broad assessment of the risks of SSR and its details are subject of chapter "3 - Optimized frequency scanning of nonlinear devices", which develops an optimized frequency scanning tool that reduces simulation time by a factor of 10 while maintaining good accuracy.

2.2.3 Eigenvalue analysis

Eigenvalue analysis is also a considerably common technique but requires complex modeling of the system. This technique uses linearized models in the form of state-space equations of a set of differential equations, of which the general form is:

$$\dot{x} = \boldsymbol{A}x + \boldsymbol{B}u \tag{2-12}$$

The eigenvalues of equation (2-12) can be found by solving:

$$\det[\lambda \boldsymbol{I} - \boldsymbol{A}] = 0 \tag{2-13}$$

where:

$\lambda = \sigma + j\omega$: eigenvalues

$\boldsymbol{I}$: identity matrix

One calculation of equation (2-13) will directly give all frequencies of oscillation and related damping values, the former being related to the imaginary part, ω, and the latter to the real part, σ. If the real part is positive, the system is not stable and therefore undamped oscillations may occur if the associated frequency is perturbed.

One issue with eigenvalue analysis is that it requires high-order models for various system components in order to achieve good accuracy, making it a complex modeling problem. Furthermore, when dealing with practical studies, detailed information about the electrical devices, such as generator controllers, are not available, as manufacturers almost always prefer to maintain their intellectual properties intact. On the other side, EMT models of such devices are usually made available in the form of black-box models by these same manufacturers to make simulations possible. These facts make frequency scanning and time-domain simulations more popular when it concerns SSR analysis.

Besides, physical nonlinearities (such as generator magnetic saturation) and switching-device behaviors are very difficult to be linearized. Finally, although this technique can be used for almost all types of SSR, it lacks effectiveness for SSR TA analysis, as it is restricted by a small-signal analysis.

2.2.4 Perturbation analysis

This technique consists of adding a small perturbation at a sub-synchronous frequency to the fundamental frequency and running the simulation until a steady state is reached. For SSR TI, SSR TA, and SSTI interactions, in which the torsional modes of the generator are involved, the perturbation analysis can be used to get the electrical damping of the system in terms of frequency, which is obtained from the relative magnitude and angle between the measured electrical torque and the measured rotor speed (the real part of $dT_e/d\omega_r$ is the damping factor).

2.2.5 Impedance-based Nyquist stability analysis

This method is based on the impedances of the grid and generator sides, herein called Z_{grid} and Z_{gen}. The grid is modeled as a Thévenin equivalent with an ideal source, V_{grid}. The current can be calculated by:

$$I(s) = \frac{V_{grid}(s)}{Z_{gen}(s) + Z_{grid}(s)} = \frac{V_{grid}(s)}{Z_{gen}(s)} . \frac{1}{1 + \frac{Z_{grid}(s)}{Z_{gen}(s)}} \tag{2-14}$$

Assuming that the voltage source is stable and the generator response to this ideal source is also stable, the term $\frac{V_{grid}(s)}{Z_{gen}(s)}$ is stable. The overall stability of the system will then only depend on the term $1/(1 + \frac{Z_{grid}(s)}{Z_{gen}(s)})$. The denominator of this term must have all zeros in the open left-half plane. We can also plot the Nyquist map of $\frac{Z_{grid}(s)}{Z_{gen}(s)}$. The number of counter-clockwise encirclements around $(-1 + j0)$ should be equal to the number of poles in the right-half plane in order for the system to be stable. A Nyquist instability corresponds to a negative resistance in the frequency scanning method [26].

Techniques using single-input and single-output (SISO) systems and multiple-input and multiple-output (MIMO) systems may vary, but the same concepts are applied [27].

2.3 Monitoring systems and applications

After assessing that a power grid is susceptible to sub-synchronous resonance, we need to ensure that proper protection and mitigation mechanisms are installed in order to guarantee reliable operation of the grid. Moreover, post-event data analysis should be performed in case an event occurs to evaluate the causes and results and take the necessary measures to prevent future events. For any of these applications, proper monitoring systems should be developed taking into account all the steps from data acquisition and signal conditioning to the SSR detection system.

One major factor in designing a monitoring system relates to the speed of detection. Protection systems usually require the fastest possible detection, which may come at the expense of reduced accuracy. However, proper protection settings should be used depending on the system while taking into account this possible reduced accuracy. Moreover, the speed of detection is highly dependent on the types of expected SSR. Phenomena that depend on the mechanical shaft torsional modes of the generator (SSR TI, SSR TA, SSTI) have mechanic inertia that slows down the sub-synchronous oscillations. On the other side, purely electrical phenomena such as SSR IGE and SSCI can result in fast-growing oscillations, requiring higher speeds of detection. Furthermore, if the monitoring system is used for mitigation schemes that do not trip an entire line or piece of equipment, then, depending on the mitigation scheme, higher accuracy may be necessary, but this may come at the expense of time consumption in the detection scheme. Lastly, post-event analysis does not have strict time requirements, so more attention can be directed to the accuracy of the results.

3 OPTIMIZED FREQUENCY SCANNING OF NONLINEAR DEVICES

High penetration of renewable generation resources and other power electronic-based elements such as HVDC lines, series active compensation devices, and shunt active compensation devices, have considerably changed the dynamic behavior of power grids [15], [17], [19], [28]-[31]. The complex control systems of these types of equipment have introduced new challenges to the power industry [15], [19], [28].

Due to the possible severe consequences of SSR events, all independent system operators (ISO) require performing SSR screening studies to evaluate the risks for all generation interconnections and transmission expansion projects. The results of this screening are utilized to assess the risks of SSR and the needs for further detailed studies and measures in the grid implementation. If SSR risks are confirmed, fast and effective detection and/or mitigation countermeasures are necessary to prevent the SSO harmful effects [29]-[31].

Popular methods for SSR screening consist of frequency scanning and eigenvalue analysis [5], [12], [33]-[38]. Eigenvalue analysis requires a detailed model of all elements of the grid, which is normally not accessible in the industry in order to protect intellectual properties. However, all industrial manufacturers usually provide their models as electromagnetic transient (EMT) black-box modules. In this case, the best approach is frequency scanning based on harmonic injection, which consists of an input-output approach.

Harmonic injection basically consists of injecting a small signal at frequencies of interest and measuring the voltage/current response, from which the impedance can be calculated. One may choose to perform one simulation per frequency of interest or to use a signal that injects each frequency individually and consecutively over time [39]. However, this approach can be time-consuming. Instead, a multisine (multi-frequency) signal containing all frequencies of interest at the same time may be injected at once to reduce simulation time. This technique is not restricted by frequency range and can be utilized to estimate the impedance of any active element at any frequency range of interest. In [40], multi-frequency injection is used to frequency-scan a static synchronous compensator (STATCOM) - although it is carried out in the super-synchronous range

instead of in the sub-synchronous range. A multi-frequency injection may lead to harmonic injection distortion when nonlinear components are present [41]. To alleviate the effects of multisine injection, one may inject a smaller number of frequencies per simulation. In this method, the most accurate results can be obtained in an ideal situation that involves separate frequency scans for every single frequency of interest. However, two factors add up to the time and financial costs of SSR screening studies. The first one is the wide range of frequencies of interest. The second one is the small time-steps (order of a few μs) required for the simulation of EMT models to correctly simulate the high switching frequencies of power electronic devices (in the order of a few kHz).

To address this issue, it is proposed herein a technique to improve the accuracy of the harmonic injection method through the optimization of the crest factor while injecting all frequencies at one shot. This technique reduces the multisine high-peak effect by scattering the signal energy during the harmonic injection while maintaining the signal RMS unchanged. This leads to higher efficiency by a considerable decrease in simulation time while maintaining good accuracy. The technique was tested on a wind farm connected to a radial test case in this chapter and is used in chapter "6 - Application and case study" in the main case study with a portion of a modified Texas synthetic grid with multiple active elements, including two wind farms and a Voltage-Source Converter (VSC)-based STATCOM. The frequency scan results were benchmarked with both a time-domain transient simulation and the ideal multiple-single-frequency-injection case and compared with other techniques.

3.1 Frequency scan

Although different frequency scanning techniques have been proposed, the injection method is the only choice for the scan of active black-box devices. In order to protect the intellectual properties, industrial manufacturers provide their models in the form of EMT black-box modules. Normally, these models include the compiled code from the system - including the controllers of the corresponding plant - to represent its most realistic response in the simulation. The harmonic injection approach provides the characteristic impedance of the nonlinear elements, such as renewable resources, and of the transmission grid as a function of frequency over the entire range of interest. For the SSR screening, independent frequency scans are performed on the generation and transmission systems from the point of interconnection (POI), as depicted in Fig. 3.1.

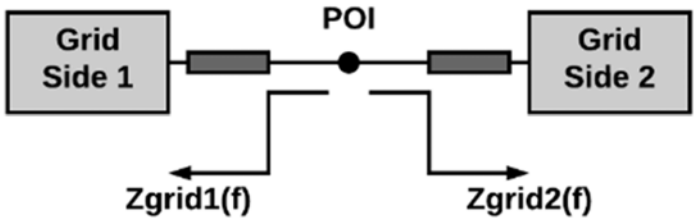

Fig. 3.1: Two sides of a generic grid connected to a POI.

The impedances can be derived in the following format:

$$Z_{grid1}(f) = R_{grid1}(f) + j * X_{grid1}(f) \quad (3\text{-}1)$$

$$Z_{grid2}(f) = R_{grid2}(f) + j * X_{grid2}(f) \quad (3\text{-}2)$$

The frequency scan results of both sides of the grid are used to calculate the cumulative resistance and reactance over the range of sub-synchronous frequencies. The cumulative resistance at a crossover frequency is an index of SSR risk [30]-[32]. To find the crossover frequency, we define:

$$R_{POI}(f) = R_{grid1}(f) + R_{grid2}(f) \quad (3\text{-}3)$$

$$X_{POI}(f) = X_{grid1}(f) + X_{grid2}(f) \quad (3\text{-}4)$$

where f is considered the crossover frequency (f_{SSR}) if:

$$X_{POI}(f) = 0 \;\&\; \frac{d}{df}\left(X_{POI}(f)\right) > 0 \quad (3\text{-}5)$$

If the resistance at this frequency, f_{SSR}, is negative, as shown in (3-6), then undamped oscillations are prone to happen.

$$R_{POI}(f_{SSR}) \leq 0 \quad (3\text{-}6)$$

The schematic of the frequency scanning tool through harmonic injection is depicted in Fig. 3.2. This method consists of the following steps:

1. Bring the scanned grid to a steady-state condition (bias point) through an equivalent source;
2. Inject a positive-sequence voltage at a frequency of interest, $V_{inj}(f)$, between the equivalent source and the terminals of the grid;
3. Measure the voltage V_{meas} and current I_{meas} at the terminals of the grid;

4. Apply the fast-Fourier transform (FFT) to both V_{meas} and I_{meas} to get $V_{meas}(f)$ and $I_{meas}(f)$ at the same frequency of the injected voltage $V_{inj}(f)$;
5. Calculate the impedance, $Z_{meas}(f)$, as in (3-7):

$$Z_{meas}(f) = \frac{V_{meas}(f)}{I_{meas}(f)} \tag{3-7}$$

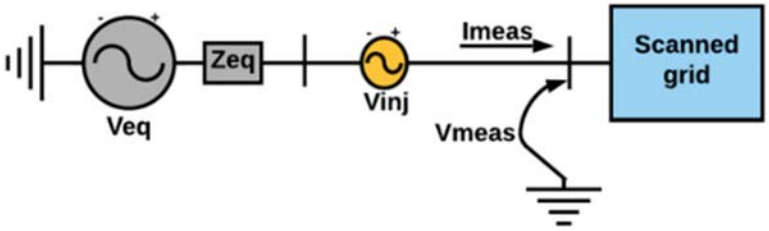

Fig. 3.2: Scheme of how to apply the frequency scanning tool.

In this scheme, V_{meas} is a phase-to-ground voltage, while I_{meas} is the current measured at the same phase.

3.2 Multi-frequency signal injection

The best outcome of frequency scanning using the harmonic injection technique is through separate frequency scans for each frequency of interest. However, whenever the goal is to estimate the impedance characteristic to active elements over a wide range of frequencies such as the SSR range, this process can take a great amount of time, especially when dealing with large grids with power electronic-based devices, in which switching frequencies may be high, in the order of a few kHz. In these situations, simulations require small time steps up to the order of a few microseconds, hence increasing simulation time. Doing the same process for every frequency of interest can become an inefficient task. The solution proposed herein involves injecting a signal containing all frequencies of interest at the same time, making it possible to scan each side of the grid with only one simulation.

3.2.1 Multisine signal

The injected voltage signal will be a multisine with period T_0, which is a sum of sine waves harmonically-related through a base frequency $f_0 = 1/T_0$ [42], as in:

$$V_{inj}(\boldsymbol{\delta}) = A * \sum_{k=k_{lo}}^{k_{hi}} sin(2 * \pi * f_k * t + \delta_k) \quad (3\text{-}8)$$

where: A: amplitude of each sinusoid

$f_k = k * f_0$, where k is an integer number

f_0: base frequency in Hz

k_{lo}: lowest harmonic of interest

k_{hi}: highest harmonic of interest

δ_k: angle at the k^{th} harmonic

$\boldsymbol{\delta}$: set of angles δ_k of all harmonics

The frequency scanning tool is used in the same way as described in the previous section. $Z_{meas}(f)$ is obtained for every injected frequency of interest after applying the FFT to the voltage and current measured signals.

3.2.2 Small-signal analysis of a nonlinear system

A linear system follows two properties, scaling and superposition. Scaling is the property of having an output amplitude proportional to the input amplitude. Superposition is the property of having an output response of two added input signals equal to the addition of the separate outputs of each input signal. Thus, a linear system with response $\mathcal{F}$ follows the following equation [43]:

$$\mathcal{F}(\alpha x_1 + \beta x_2) = \alpha \mathcal{F}(x_1) + \beta \mathcal{F}(x_2) \quad (3\text{-}9)$$

The grid may contain devices that present nonlinear behavior, as in power electronic-based controllers, such as in wind farms, LCC-HVDC lines, VSC-HVDC lines, and STATCOM devices, among others. This means that the current-voltage relationship is not linear, as seen in Fig. 3.3 for the example of an IGBT characteristic IxV output curve [44], which is one of many possible sources of nonlinearities. Other possible sources can be found in reference [45]. IGBTs are one of the nonlinear devices normally present in wind turbine controllers. From the figure, we can see that, above a certain voltage amplitude, the current response is not in the linear region anymore. Therefore, the

impedance cannot be simply calculated by the ratio between voltage and current, and equation (3-7) is not valid. Furthermore, the superposition of frequencies is not valid for nonlinear systems, which means that the sum of all individual responses for each frequency is not equal to the overall response of the system when injecting all frequencies at the same time. Thus, equation (3-8) is not applicable to (3-9), as we cannot subsequently apply an FFT to get each frequency's response when injecting many frequencies at the same time. For equations (3-7) through (3-9) to be valid, a small-signal analysis should be performed, with the voltage high enough to avoid being covered in noise (high signal-to-noise ratio – SNR), but small enough to maintain linearity and follow the superposition principle. This is possible by performing injections of small magnitude around a point of steady-state operation, called bias point [43].

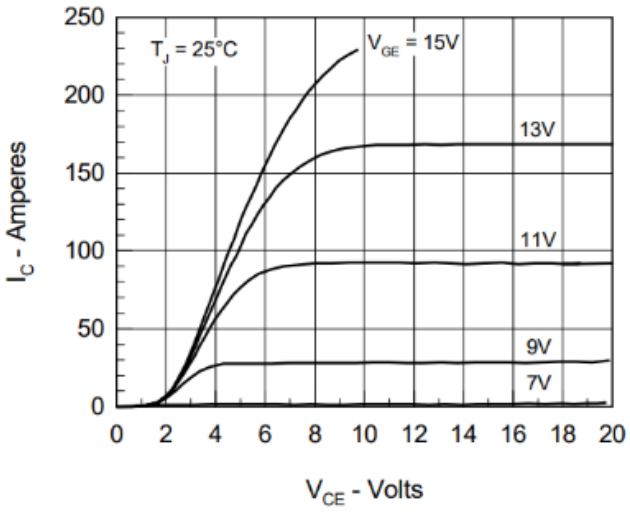

Fig. 3.3: Typical IGBT current x voltage output characteristic curve (source of figure [44]).

Assuming we have chosen an amplitude that falls within an acceptable range, if we apply the following parameters in equation (3-8), the resulting multisine signal will be as in Fig. 3.4.

$$A = 1\ \text{V}; f_0 = 1\ \text{Hz}; k_{\text{lo}} = 5; k_{\text{hi}} = 35; \delta_k = 0$$

From Fig. 3.4, we can see that, for an amplitude of 1 V, and a range of 5 Hz to 35 Hz with frequencies 1 Hz apart, if we use $\delta_k = 0$, large spikes happen every second, reaching a peak of 25.04 V. The period of these spikes is $T_0 = 1/f_0$. If instead of setting $\delta_k = 0$ for every frequency we apply variations in $\boldsymbol{\delta}$ for each frequency, the energy in the

signal will be scattered instead of concentrated in a few particular instants of time. This means that large spikes can be avoided while the root-mean-square value (RMS) of the signal remains the same, therefore maintaining the small-signal requirement. A good parameter that depicts this situation is the crest value, as defined in (3-10).

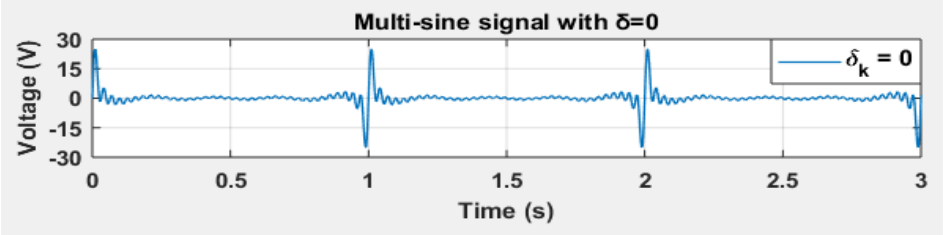

Fig. 3.4: Multisine signal with frequencies 1 Hz apart from 5 Hz to 35 Hz and $\boldsymbol{\delta_k = 0}$.

$$C(\boldsymbol{\delta}) = \frac{|Peak\ \ V_{inj}(\boldsymbol{\delta})|}{RMS\ \ V_{inj}(\boldsymbol{\delta})} \tag{3-10}$$

3.2.3 Multisine signal crest factor optimization

Smaller crest values lead to smaller peak values for the same RMS, helping to realize the necessary small signal. With that in mind, an optimization problem can be defined to minimize the crest value using the angles δ_k as variables. The general formulation is:

$$\begin{aligned} &minimize\ C(\boldsymbol{\delta}) \\ s.\ t.& \\ &g_k(\delta) = -\delta_k \leq 0^{\circ} \\ &h_k(\delta) = \delta_k - 360^{\circ} \leq 0 \end{aligned} \tag{3-11}$$

Using the nonlinear Lagrangian optimization method [46], one may achieve first-order optimality through the Karush-Kuhn-Tucker (KKT) conditions. The KKT conditions are analogous to making the gradient equal to zero, that is, to bringing the objective function to a minimum value. The Lagrangian function is as follows:

$$L(\boldsymbol{\delta}, \boldsymbol{\lambda}) = C(\boldsymbol{\delta}) + \sum_{k=k_{lo}}^{k_{hi}} \lambda_{g,k} g_k(\delta_k) + \sum_{k=k_{lo}}^{k_{hi}} \lambda_{h,k} h_k(\delta_k) \tag{3-12}$$

The KKT conditions are shown in equation (3-11) above and in equation (3-13) below:

$$\begin{aligned} \left|\left|\nabla L(\boldsymbol{\delta}, \boldsymbol{\lambda})\right|\right| &= 0 \\ \lambda_{g,k} g_k(\delta_k) &= 0 \ \forall k \\ \lambda_{h,k} h_k(\delta_k) &= 0 \ \forall k \end{aligned} \tag{3-13}$$

The optimality measures associated with (3-13) are:

$$\begin{aligned} \left|\left|\nabla L(\boldsymbol{\delta}, \boldsymbol{\lambda})\right|\right| = ||\nabla C(\boldsymbol{\delta}) + \sum_{k=k_{lo}}^{k_{hi}} \lambda_{g,k} \nabla g_k(\delta_k) + \sum_{k=k_{lo}}^{k_{hi}} \lambda_{h,k} \nabla h_k(\delta_k)\,||, \\ \left\|\overrightarrow{\lambda_{g,k} g_k(\delta_k)}\right\|, \\ \left\|\overrightarrow{\lambda_{h,k} h_k(\delta_k)}\right\|. \end{aligned} \tag{3-14}$$

However, we need to take into account that the Lagrangian method is an efficient method under a good initial estimate of the solution. This estimate can be derived from the Schroeder equation and is presented in equation (3-15) [40].

$$\delta_{k,0} = rem\left((f_k - f_{lo}) * \frac{f_k - f_{lo} + 1}{f_{hi} - f_{lo} + 1} * 360, 360\right) \tag{3-15}$$

where: $rem(a, b)$: remainder operator on a divided by b

f_{lo}: lowest frequency of interest

f_{hi}: highest frequency of interest

Depending on the software that will be used for the power system simulations, the problem can be relaxed by removing the constraints associated with $g_k(\delta)$ and $h_k(\delta)$.

The frequency scan can then be performed using a low-crest-factor multisine containing many frequencies at the same time while maintaining the small-signal requirements. Hence, we are able to perform an FFT calculation to get each individual frequency response based on the overall response output according to the superposition principle.

3.2.4 Minimum simulation time

The minimum total simulation time for multiple single-frequency injections (injecting one frequency per simulation or injecting individual frequencies consecutively) is [47]:

$$T_{sf} = \sum_{k=k_{lo}}^{k_{hi}} \left\{ \frac{1}{f_k} + Tst_k \right\} \right) \tag{3-16}$$

where: Tst_k: settling time at frequency f_k

Now, assuming that we achieved a low crest value for the multisine signal (injecting all frequencies at the same time in one simulation), the signal-to-noise (SNR) ratio will be high [42]. The minimum total simulation time in this case is:

$$T_{ms} = T_0 + \max\{Tst_k\} \tag{3-17}$$

where: $T_0 = 1/f_0$ (period of the base frequency)

A good approximation to establish the settling time can be achieved by determining the time required for the envelope of the signal to reach and remain within a certain percentage range of its final value (usually 2% or 5%) [48].

3.3 Example case

The proposed method was implemented in MATLAB, but it can also be implemented in different platforms with EMT simulation capabilities, such as PSCAD/EMTDC or ATP/EMTP. Furthermore, all the case studies include detailed models of wind farms, STATCOM and distributed parameters for transmission lines developed in MATLAB/Simulink.

In order to evaluate the performance of the proposed optimized technique, a case study including a black-box model of a 100 MVA wind farm connected to the grid through a series-compensated line is used. The system is depicted in Fig. 3.5 and the impedance data of the radial connection are in Table 3.1. As can be seen, the wind farm and its respective collection system are connected to the POI through a station transformer

and a gen-tie line. Moreover, the transmission line has 70% of compensation and connects the POI to the equivalent grid.

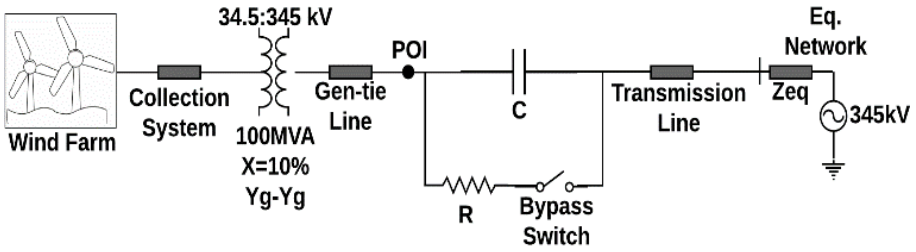

Fig. 3.5: Wind farm connected to the radial test system.

Table 3.1: Radial test system parameters.

Parameters	Collection System	Gen-tie Line	Transmission Line	Equivalent Network
R(Ohm)	0.0492	0.2106	3.17	0.74
X(Ohm)	0.0639	1.9258	39.6	4.98

The wind farm uses DFIG technology with a vector-oriented control strategy. The black-box model includes the detailed representation of the turbine aerodynamics, mass-drive train, induction machine, and rotor-side and grid-side converters with their controllers. The wind turbine control parameters and induction generator data are based on a commercial wind turbine [49].

The following sub-sections comprise three steps. Firstly, different methods, including the proposed optimized method, are used to generate the multi-frequency harmonic signals. Secondly, separate frequency scans are performed on the wind farm as well as on the grid side using the different harmonic signals generated in the first step. The frequency scan results are compared and benchmarked against ideal single-frequency injections. Also, the cumulative resistance and reactance at the POI are calculated to evaluate the risk of SSCI incidents. Finally, a time-domain transient simulation is performed to validate the accuracy of the proposed technique.

3.3.1 Generating the multisine signal for the frequency scan

To generate different harmonic signals, different formulas were applied to calculate the angles of the multisine expressed in equation (3-8). The following parameters were used:

$$A = 345\ \text{V}; f_0 = 1\ \text{Hz}; k_{\text{lo}} = 5; k_{\text{hi}} = 35$$

The frequency range was chosen based on the previous sub-synchronous oscillation frequencies observed in past events in the USA and China, as shown in the introductory section of this paper [5], [8], [10]. The small-signal voltage amplitude, 345 V, is chosen at 0.1% of the rated voltage, 345 kV. The frequencies injected are separated by 1 Hz. Different methods of angle calculation and their corresponding crest factors are depicted in Table 3.2. The plots in Fig. 3.6 show the normalized waveforms of the multi-frequency signals using different angles in $\boldsymbol{\delta}$. The normalization is done by dividing the waveforms by the amplitude of each injected sine wave, in this case, 345 V. In this way, we can easily see the effects of the multisine injection on the peak value for every 1 V injected.

As it is evident in Fig. 3.6, simply using zero for all angles leads to large spikes in the harmonic signal. These can produce errors in the frequency scan. However, more appropriate angles disperse the energy of the multisine while maintaining the RMS value unchanged. Method 2 utilizes a quadratic relation of the frequency and has been used previously in [41].

Table 3.2: Methods of different angles and respective peak, RMS, and crest values after normalization.

Method #	Equation for angle δ_k	Peak value	RMS value	Crest value
1	$\delta_k = 0$	25.04	3.94	6.36
2	$\delta_k = {f_k}^2$	16.30	3.94	4.14
3	$\delta_k = Schroeder$ (equation (3-15))	7.36	3.94	1.87
4	$\delta_k = Optimized$	5.86	3.94	1.49

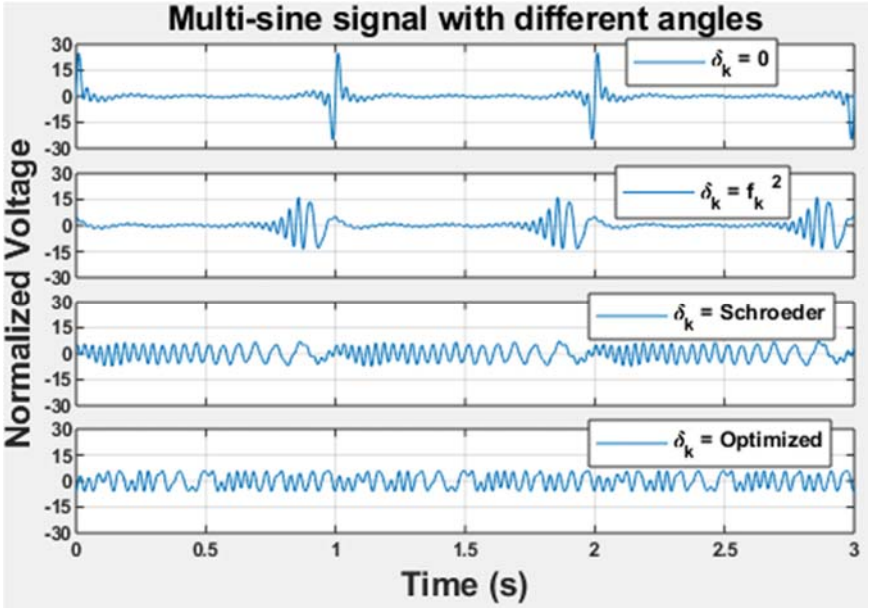

Fig. 3.6: Waveforms of the normalized multisine signals using different angles.

The methods in Table 3.2 are listed in the order of larger to smaller crest factors, being the latter the proposed optimized method. A single sine wave has a crest factor of $\sqrt{2}$, which is approximately 1.4142. We can then easily reason that, when adding more sine waves at other frequencies, the crest factor will only get larger. The proposed optimized method resulted in a crest factor of 1.49 when generating a 31-frequency signal, which is an indication that it is close to an optimal value.

3.3.2 Frequency scan results

At this step, the signals of the four methods of the multisine waves were separately injected into the wind farm black-box model as well as into the grid to perform the frequency scan. The results were benchmarked against reference results taken from multiple simulations of single-frequency injections.

In this case study, the grid side consists only of linear components, such as resistors, capacitors, and inductors; and the wind farm consists of active devices with nonlinear behavior, such as controlled IGBTs and phase-locked loops.

To evaluate the risk of SSCI, the cumulative resistance and reactance at the POI were depicted in Fig. 3.7, which also contains a zoomed-in version around the crossover frequencies. Now, using equation (3-5) we can find the crossover frequency (zero reactance) in order to assess the risk of undamped oscillations with equation (3-6). The

frequency of oscillation found for each method and respective resistance values at these resonant frequencies are shown in Table 3.3 along with the single-frequency-injection reference results.

If the differences between the resistance/reactance of each method and the reference results are defined as errors, the methods with smaller crest factors should lead to smaller errors. The cumulative resistance and reactance errors are plotted in Fig. 3.8. The average total error calculated for each method in the frequency range is shown in Table 3.4 and Table 3.5.

The results indicate that the smaller the crest factor, the smaller the error. Among all methods, the proposed optimized injection signal results in a more accurate frequency scan.

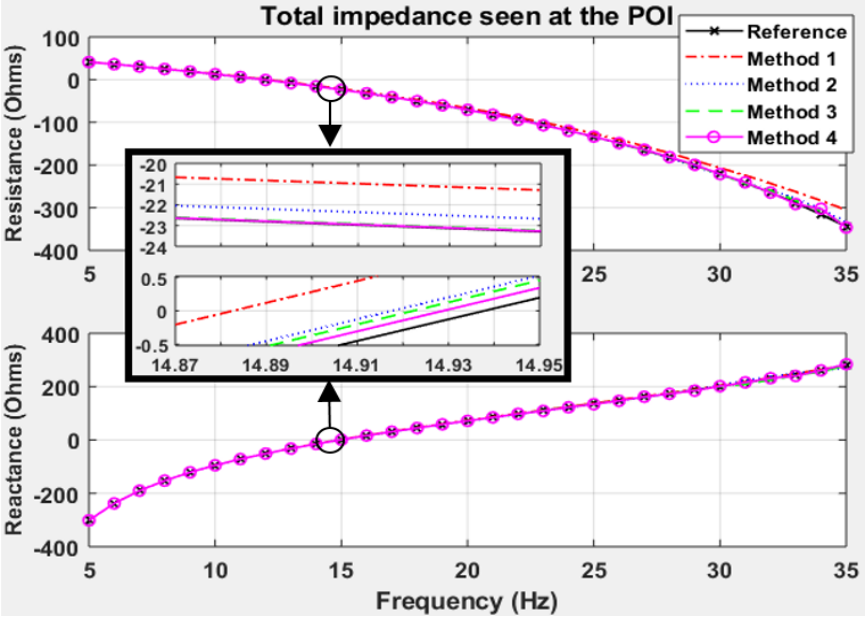

Fig. 3.7: Total resistance and reactance seen from the POI.

Table 3.3: Frequency of oscillation and resistance values.

Method #	Frequency of Oscillation (Hz)	Resistance (Ω)
1	14.88	-20.78
2	14.92	-22.40
3	14.92	-23.02
4	14.93	-23.10
Reference	14.94	-23.20

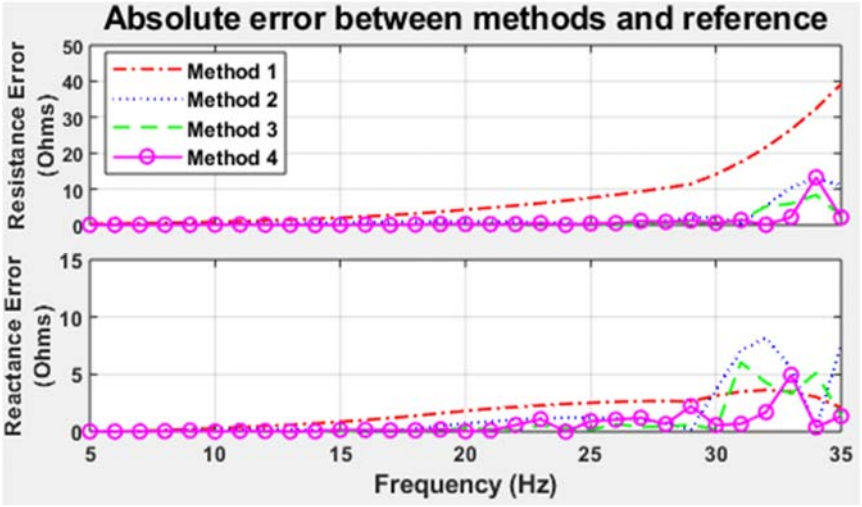

Fig. 3.8: Error of each method in relation to the reference.

Table 3.4: Total resistance error of methods in relation to the reference.

Method #	Equation for angle δ_k	Average Total Error (Ω)
1	$\delta_k = 0$	8.012
2	$\delta_k = {f_k}^2$	1.864
3	$\delta_k = Schroeder$ (equation (3-15))	0.931
4	$\delta_k = Optimized$	0.842

Table 3.5: Total reactance error of methods in relation to the reference.

Method #	Equation for angle δ_k	Average Total Error (Ω)
1	$\delta_k = 0$	1.664
2	$\delta_k = {f_k}^2$	1.417
3	$\delta_k = Schroeder$ (equation (3-15))	0.801
4	$\delta_k = Optimized$	0.600

3.3.3 Time-domain transient simulation

To validate the results of the frequency scan, a time-domain transient simulation was performed as per the following sequence:

- Series capacitor by-passed by closing the bypass switch;
- The simulation was run until t=35 seconds to ensure that steady-state is achieved;
- The bypass switch is opened at t=35 seconds to create a radial condition between the wind farm and the series-compensated line. This creates an SSCI oscillation.

The three-phase active power and instantaneous voltages and currents at the POI are depicted in Fig. 3.9.

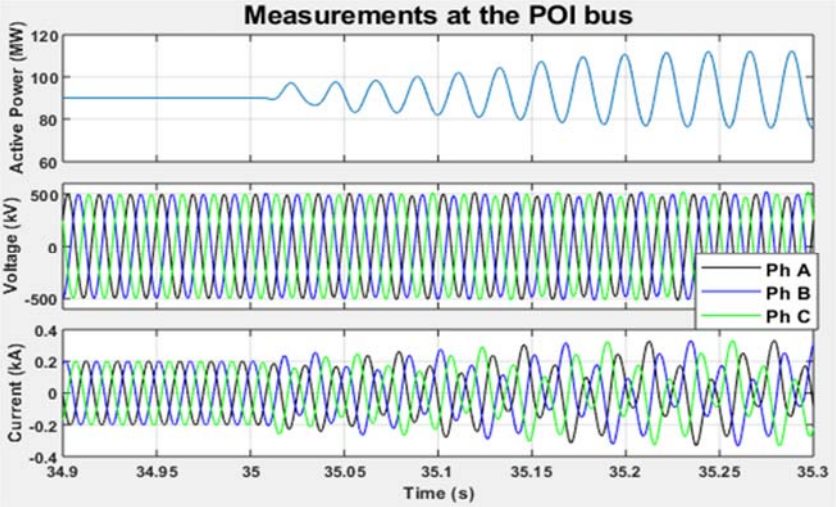

Fig. 3.9: Time-domain transient simulation results at the POI. Active power on the top. Voltage in the middle. Current on the bottom.

In line with the frequency scan results, the time-domain transient simulation shows the SSCI risk. The results from the FFT analysis performed on the current signal of the time-domain simulation shows the frequency of oscillation at 14.95 Hz. The growing behavior of the oscillation indicates an undamped oscillation, which corresponds with the negative sign of the resistance found in the frequency scan.

It can be seen that the captured resonant frequency from the optimized method is an almost perfect match with the results of the ideal frequency scan and the time-domain simulation.

4 SUB-SYNCHRONOUS RESONANCE DETECTION SYSTEM

Since the first sub-synchronous resonance event in 1970 in the Mohave station, where SSR TI was experienced, and the most recent reported SSCI event (up to the date of writing this document) in the ERCOT system, in 2017, the monitoring and protection requirements and designs have varied in several aspects, including speed of detection, accuracy of detected sub-synchronous oscillations, nature of interaction (purely electrical or with presence of mechanical/torsional modes), protection/mitigation requirements, and post-event analysis needs. This chapter proposes a complete detection system that can be used for these applications and includes processing technology, signal conditioning, detection algorithm, output post-processing, and field implementation considerations.

4.1 Processing technology

When developing an application, different processing technologies may be used depending on the requirements and costs associated. Implementation can be carried out using instruction-based hardware, which is configured via software in general-purpose circuits, or by directly specifying a hardware circuit for the specific application. The former and common approach uses architectures such as central processing units (CPU), in which the hardware is not reconfigurable and software-based programming is utilized through control-flow semantics. CPUs provide easy (re-)programmability and are usually cheap options for a wide range of applications. Contrarily, the latter approach involves hardware-circuit design through data flow semantics using hardware description languages (HDL). One circuit-design approach is to manufacture application-specific integrated circuits (ASIC), which are fully customizable chips for both analog and digital functionalities. Although ASIC technology provides high performance and low power consumption and size, the design process is much more complex and costly. Besides that, as the name states, it is application-specific, therefore not providing flexibility and re-programmability. An alternative that has been gaining a lot of attention in the market and the research community consists of field-programmable gate arrays (FPGA). Frequently, FPGAs fulfill the needs for fast response and acquisition rates; operation of high volumes of data; and customizable hardware configuration with the addition of reprogramming capabilities [51]. Development costs are not as high as for ASIC design and more research has been put into FPGA-based monitoring systems [52]. Monitoring systems are

generally CPU-based and/or use application-specific hardware, such as the one found in [53]. A CPU-FPGA heterogeneous platform can be a great option to achieve high performance while not disproportionately increasing the costs [54]. In [55], a CPU-FPGA system is used for the throughput optimization for streaming applications. In [56], a CPU-FPGA monitoring system for wind turbines is presented.

Many traditional systems use CPUs, which have a fixed hardware structure and operate through sequential processing, that is, they process tasks in sequence, one at a time. FPGAs, however, have reprogrammable hardware capabilities and are able to operate through parallel processing, that is, processing multiple tasks at the same time. Table 4.1 shows a comparison of the technical aspects of CPUs and FPGAs.

Table 4.1: CPU/FPGA comparison.

Aspects	**CPU**	**FPGA**
Processing	Sequential	Parallel
Flexibility	Software	Hardware
Data-to-clock ratio	Lower	Higher
Determinism	Lower	Higher
Computational throughput	Lower	Higher
Memory allocation	No	Yes
Less frequent tasks	Best suited	-
Sorting/searching	Best suited	-
Matrix calculations	Best suited	-
Floating-Point Arithmetic	Usually better	Depends on model

FPGAs provide the flexibility of hardware programming, while CPUs provide the flexibility of software programming with easy updating and, often, ready-to-use libraries, reducing the development costs and being a good choice for routine operations [57].

Although FPGA clock rates are usually lower than CPU clock rates, the parallel processing capability makes it possible to perform algorithms in fewer clock cycles, often resulting in increased performance. Determinism is better achieved in FPGAs, as code is programmed directly in hardware with parallel processing nature. CPUs, however, depend on other variables, such as how many tasks need to be currently performed and how many CPU resources each of these tasks will take. Besides, one task needs to be completed before the next one starts. Monitoring systems that require high acquisition rates and several inputs/outputs (I/O) will demand large volumes of data to be processed. The parallel nature of FPGAs can provide high computational throughput.

Nonetheless, CPUs are not only relevant due to reduced costs in comparison to FPGAs. Some tasks are better suited to CPUs. First, memory allocation is a major concern for FPGAs. Every piece of code written will allocate physical memory in the FPGA internal resources. This is not the case for a CPU, which only allocates its resources for the tasks being run at the moment. Hence, we need to keep in mind that less frequent tasks are better suited for CPUs. These tasks may include data logging, report generation, and data display, among others. On the other side, frequent tasks such as event detection (monitoring/protection functions), if they need to have updated results for every sample or cycle, are better suited for FPGAs. Only if the requirement of the update rate is not high that they can be in CPUs. Furthermore, sorting and searching techniques are basically sequential by nature [57], and it would provide no benefit in allocating FPGA memory resources for these tasks. Finally, FPGAs usually use fixed-point arithmetic. Hence, floating-point arithmetic is usually better suited to CPUs. However, there are FPGA models that can handle floating-point operations, but they will allocate more resources and are more expensive.

4.2 Sampling rate

Sampling rate considerations can be divided into two parts. The first part is concerning the acquisition system sampling rate, which is the one used in the data acquisition modules to which the input signals are connected. The second part is related to the data processing system, in which the monitoring/protection algorithms are implemented.

4.2.1 Data acquisition sampling rate

When choosing a sampling rate f_{sr} for the acquisition system, we must take into account the highest frequency component f_h present in the signal so as to perform the analog-to-digital conversion and accurately represent the original signal. Shannon's sampling theorem states that a sampling frequency greater than twice the highest frequency present in the original analog signal is able to perfectly reconstruct it from the sampled discrete-time signal [58]:

$$f_{sr} \geq 2 * f_h \tag{4-1}$$

where: f_{sr}: sampling rate of the acquisition system

f_h: highest frequency component in the analog signal

The Nyquist rate $f_{Ny.rate}$ is the minimum sampling rate:

$$f_{Ny.rate} = 2 * f_h \tag{4-2}$$

The Nyquist frequency $f_{Ny.frequency}$ is the highest representable frequency for a given sampling rate f_{sr}.

$$f_{Ny.frequency} = \frac{f_{sr}}{2} \tag{4-3}$$

The Nyquist interval is the representable frequency range for a given sampling rate f_{sr}:

$$\text{Nyquist interval} = [-f_{sr}/2, f_{sr}/2] \tag{4-4}$$

Note that the highest frequency component in the analog signal does not necessarily denote the highest frequency of interest in the application. If frequencies above the Nyquist frequency are present in the analog signal, these components will fold back to the Nyquist interval and overlap with the actual components in this range. The result is an overestimation of these actual components and consequent distortion of the representation of the original signal in an effect called aliasing. Therefore, any frequencies above $f_{Ny.frequency}$ need to be removed using an antialiasing filter.

4.2.2 Data acquisition: oversampling

Typical acquisition rates in digital relays are 16, 32 and 64 samples per cycle, which gives 960, 1920, and 3840 samples per second, respectively. From the data acquisition sampling rate criterion shown in the previous item, frequencies above 480 Hz, 960 Hz, and 1920 Hz need to be blocked, respectively for these cases. This is usually performed employing an analog lowpass filter. An alternative solution to analog filters is the usage of oversampling in the analog-to-digital conversion to include all frequency components present in the original signal. Subsequently, digital filtering can be utilized

to keep only the frequencies of interest, followed by downsampling, if deemed necessary. Oversampling is also a good alternative when trying to avoid large phase distortions introduced by lowpass filters, especially when a steep roll-off is necessary and considering that the phase shifts are not linear, that is, not proportional to their frequencies. This alternative solution allows the use of only simple low-cost analog lowpass filters of low order and with low roll-off rates.

4.2.3 Signal conditioning: downsampling

The previous sub-items are related to the sampling rate of the acquisition system. When it comes to the sampling rate for the data processing system, different criteria need to be considered. In this step, we need to take into account the limitations of the detection algorithms and platforms used in the system. Depending on the design, processing power is a limiting factor and the amount of data to be processed is a major concern. This is especially true when considering the following factors [59]:

- Sequential-based platforms: especially when CPU is one of the platforms used, resources are limited at the same time that processing is sequential. This means that, if one task takes too long to complete, the following tasks will be delayed. These delays can add up for every processing cycle and the program may not be able to catch up, resulting in data loss or inefficacy of the system.
- Power consumption and temperature: power consumption usually increases with processing load. Large amounts of data will require more power consumption and higher temperature levels may result.
- Computational complexity: different algorithms will require different amounts of resources, such as time, storage, communication, number of gates in a circuit, and number of processors, among other measures of complexity.

When the above factors (which are not an exhaustive list) are considered, performing all the algorithms calculations for every data sample may not be feasible. In these cases, downsampling may be considered in order to reduce the computational burden.

Downsampling consists of reducing the sampling rate by a factor D through a process called decimation, which is carried out by keeping only every D^{th} sample and discarding the $(D-1)$ samples in between. The new lower sampling rate is then:

$$f_{sr,down} = f_{sr}/D \tag{4-5}$$

However, the sampling theorem assumes that the bandwidth of the signal is limited, which implies that frequencies above the Nyquist frequency need to be filtered out [58]. When reducing the sampling rate by a factor D, the bandwidth is also reduced by a factor D; hence the Nyquist frequency is reduced by this same factor. As a consequence, it is necessary to apply a lowpass filter before the decimation process, of which the cutoff frequency is up to:

$$f_{Ny,down} = f_{sr,down}/2 \tag{4-6}$$

As the downsampling process is performed after data acquisition, the filter can be implemented in its digital form. The downsampling steps can be summed up in two steps:

1. Apply a digital lowpass filter with a cutoff frequency of up to $f_{Ny,down}$ to the digitized data;
2. Decimate the filtered signal by a factor D.

When dealing with the sub-synchronous range, we are focusing on frequencies below 60 Hz (or 50 Hz, depending on the electrical system). The Nyquist criterion states that the minimum sampling rate should be at least two times the highest frequency in the signal, which is 120 Hz. However, real-time applications typically use higher sampling rates, when possible, to achieve more accurate results and avoid aliasing whatsoever, often reaching 5-10 times the highest frequency of interest, that is, data processing sampling rates of 300 Hz to 600 Hz for a 60 Hz system.

4.3 Signal conditioning: tapered window functions

A powerful tool to perform spectral analysis of signals is the discrete Fourier transform (DFT). For a discretized time-domain signal $x(n)$ with length N, the DFT is obtained for equally-spaced samples at frequencies $\omega_k = 2\pi k/N$ with:

$$x(k) = x(\omega)|_{\omega=2\pi k/N} = \sum_{n=0}^{N-1} x(n) * e^{-j\left(\frac{2\pi k}{N}\right)n)} \quad (4\text{-}7)$$

where: $n = 0, 1, \dots, N-1$: time index (in samples)

k$= 0, 1, \dots, N-1$: index of each frequency bin

When performing a spectral analysis of signals, we can get the exact frequency content of a signal if we ideally have an infinite number of samples to perform the calculations. However, in real applications we must select a limited amount of samples to perform the spectral analysis, that is, we need a windowed signal. A window is a selection of a specified number of N consecutive samples to be used as a data set for various applications, such as spectral analysis. A given discretized signal $f(n)$ is windowed from sample N_1 to N_2 if:

$$f_w(n)|_{N_1}^{N_2} = \begin{cases} f(n), & N_1 \le n \le N_2 \\ 0, & otherwise \end{cases} \quad (4\text{-}8)$$

where:

$f_w(n)$: windowed signal

N_1: first sample inside the window

N_2: last sample inside the window

n: sample index in the time domain

$N = N_2 - N_1 + 1$: length of the window

Any spectral analysis with a finite window length inevitably leads to a phenomenon called spectral leakage. This effect erroneously creates new frequency components not existent in the actual signal, which can be seen in the sidelobes of their Fourier transform.

Tapered window functions modify the window shape and multiply the discretized signal inside the window in order to taper the signal and achieve modified shapes to get some desired feature and reduce the effects of the sidelobes created by windowing the signal. Considering only the samples inside the window, we have:

$$f_w(n) = f(n)w(n) \tag{4-9}$$

where: $f_w(n)$: function $f(n)$ after application of window $w(n)$

$w(n)$: tapered window function

Equation (4-8) is equivalent to the multiplication of signal $f(n)$ by a rectangular window, which consists of ones inside the window and zeros outside the window. If we take only the values inside the window, we have:

Rectangular window: $w(n) = 1, \quad N_1 \leq n \leq N_2$ (4-10)

The shape of a generic rectangular window and its one-sided (positive frequencies only) DFT are shown in Fig. 4.1.

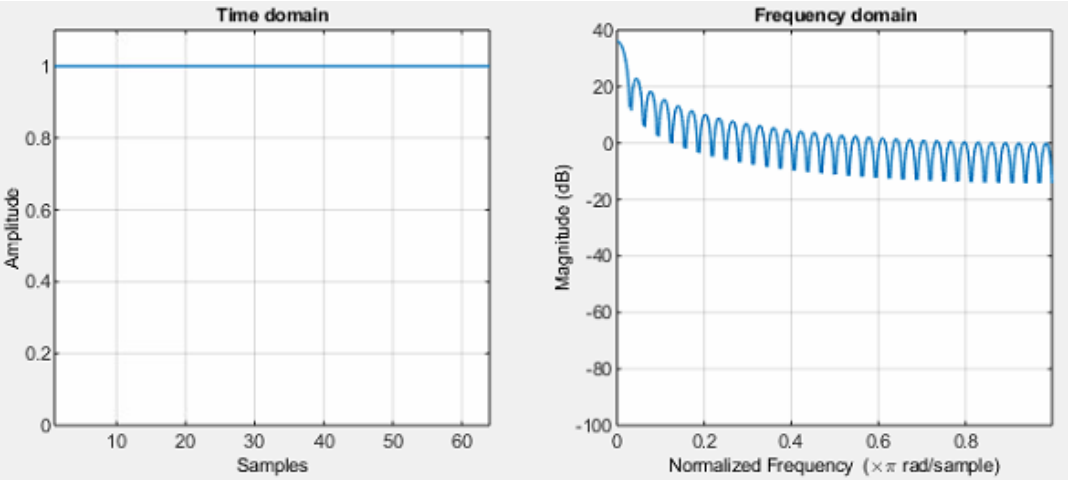

Fig. 4.1: DFT of a generic rectangular window.

Now, take a sinusoidal waveform:

$$f(n) = A\cos(\omega_f t + \theta) \tag{4-11}$$

If we use equation (4-9) to multiply (4-11) by the rectangular window in (4-10) with a length of three cycles, the time-domain waveform and frequency-domain DFT of the windowed sinusoid are as shown in Fig. 4.2:

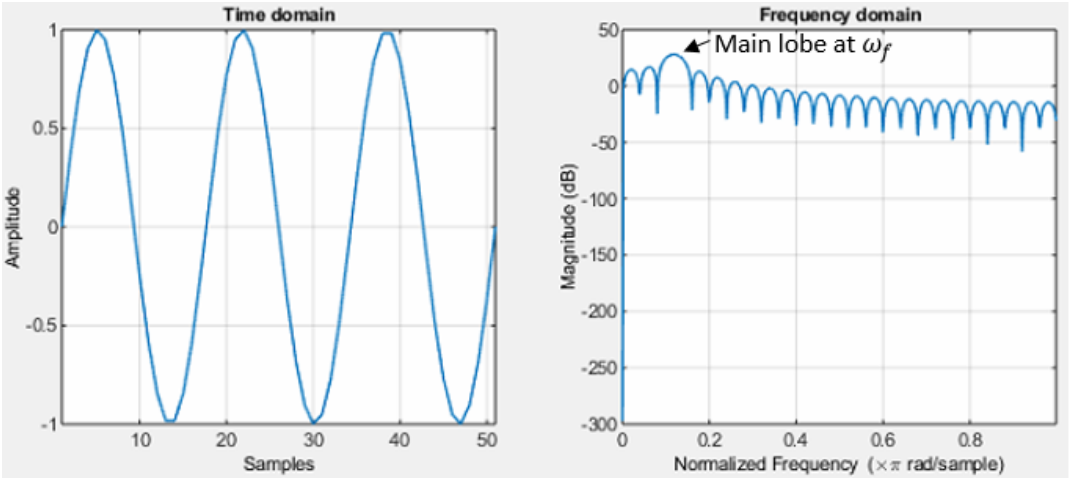

Fig. 4.2: Time-domain and frequency-domain DFT results of the sinusoid with a three-cycle rectangular window.

Although the sinusoid obviously has only one frequency component ω_f, its DFT captures the frequency content of the signal with distortion, creating sidelobes from the leakage around the main lobe. This means that the energy contained in one frequency is sensed in more than one frequency bin when applying the DFT, i.e., there is leakage from one bin to adjacent bins. The result is an incorrect representation of the frequency content of the signal, also known as a not-accurately-resolvable frequency content.

The total leakage of a window function can be measured by what is called equivalent noise bandwidth (ENBW). It is equivalent to redistributing the DFT of the window function into a rectangular shape with height equal to the maximum value of the spectra and the same area of all lobes' areas-under-the-curve added. The value of the bandwidth that results from this rectangle is the ENBW.

Different tapered windows can be applied to reduce the effects of spectral leakage. Notice, however, that it is not possible to reduce the amount of total leakage. Indeed, other windows actually have larger ENBW than the rectangular window. It is possible, however, to redistribute the leakage where it causes less ill effects. The choice of the window will depend on the application. Examples of tapered windows include the cosine-sum windows given by:

$$w(n) = \sum_{k=0}^{K_b} (-1)^k \, a_k \cos\left(\frac{2\pi kn}{N-1}\right), \qquad n = 0 \leq n \leq N-1 \tag{4-12}$$

where $K_b = 1$ is the number of non-negative frequency bins.

Two main parameters describe the characteristics of window functions. The first is the width of the main lobe; the second is the level of the sidelobes relative to the main lobe. A narrow main lobe provides higher frequency resolution around the detected frequencies in the frequency domain. This is achieved by maintaining the amplitude at its normal level in most of the window length in the time domain. The most extreme case is the rectangular window shown in Fig. 4.1. The expense is the abrupt falling and rising edges in the time domain, which produces higher sidelobe levels in the frequency domain that result in a low dynamic range (ratio between largest and smallest values). If we want to reduce the sidelobe levels, we need to smoothen the edges. The frequency resolution around the detected frequency will be lowered due to a wider main lobe, but a higher dynamic range and increased resolvability between frequency components can be achieved (two frequencies are unresolvable if they are located in the same DFT frequency bin). A Hanning window is a type of cosine-sum window (also known as a raised-cosine type of window) with an ENBW of 1.5 and can be described by its parameters in equation (4-13) and Fig. 4.3. Comparing with the rectangular window, we can see that the main lobe is wider, but the sidelobes are largely reduced.

$$w(n) = 0.5\left[1 - \cos\left(\frac{2\pi n}{N-1}\right)\right], \qquad n = 0 \le n \le N-1 \tag{4-13}$$

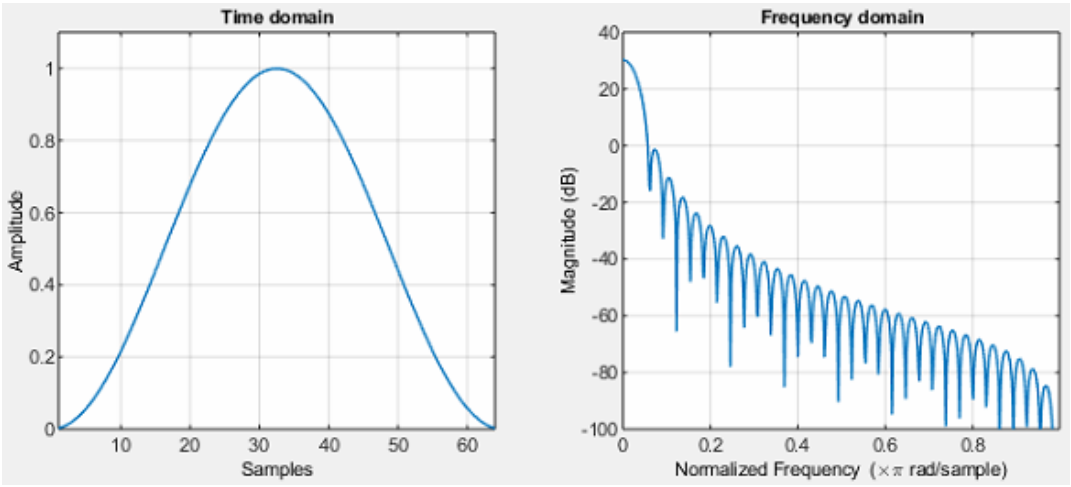

Fig. 4.3: DFT of a generic Hanning window.

A Hamming window is similar to the Hanning window, but it does not completely nullify the edges of the window. It has an ENBW of 1.362826 and can be described by its parameters in equation (4-14) and Fig. 4.4. Comparing with the rectangular window, we can see that the main lobe is wider, but the sidelobes are largely reduced. Comparing with the Hanning window, the main lobe is slightly narrower and it does not reach the same attenuation levels for the sidelobes. Therefore, the Hamming window is an intermediate tapered window between the rectangular and the Hanning window, with a higher ENBW level than the former, but lower than the latter.

$$w(n) = 0.53836\left[1 - \cos\left(\frac{2\pi n}{N-1}\right)\right], \qquad n = 0 \leq n \leq N-1 \tag{4-14}$$

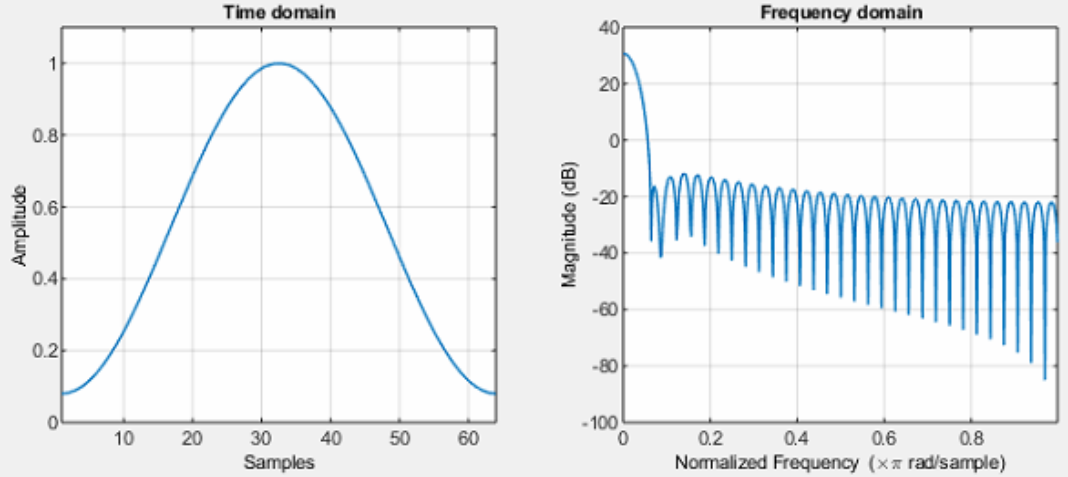

Fig. 4.4: DFT of a generic Hamming window.

Appendix A shows the ENBW values of some of the main tapered window functions.

4.4 Signal conditioning: filters

This item will focus on linear time-invariant (LTI) filters that are necessary to not only limit the signal to the frequency range of interest but also to improve the performance of the detection algorithms.

Filters can be represented by difference equations or, equivalently, by a transfer function. Different from analog filters, almost any transfer function can be implemented

in its digital form, making them a complex, but powerful tool. The limitations will depend on the processing technology/power and costs associated, as well as specific application requirements.

There are basically two main types of digital filters, linear and nonlinear. Linear filters are widely used in most applications and can be divided into infinite impulse response (IIR) and finite impulse response (FIR) filters [58]. This text will focus on the characterization of causal linear-time invariant (LTI) filters as given by their steady-state response, which has outputs that depend only on past and present inputs and follow the properties of scaling and superposition, which are shown in equation (3-9) [43], [60].

Fig. 4.5 shows a generic bandpass filter, where:

f_{sc1}: first stopband corner frequency

f_{pc1}: first passband corner frequency

f_{pc2}: second passband corner frequency

f_{sc2}: second stopband corner frequency

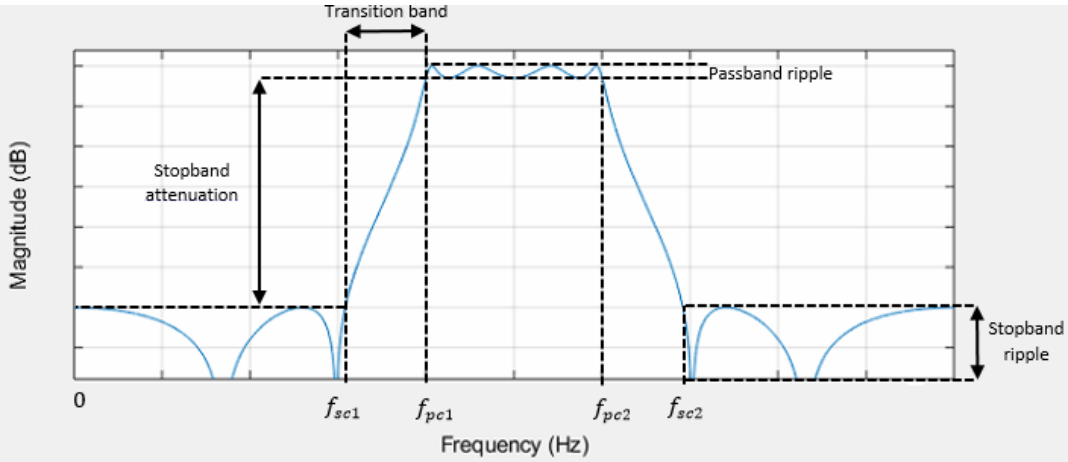

Fig. 4.5: Generic bandpass filter.

4.4.1 Magnitude and phase response

The magnitude of the frequency response of a filter is usually taken in terms of the gain in decibels (dB). One common definition in electrical circuits for a filter with transfer function $H(z)$ is:

$$Gain_{dB} = 20\ log_{10}|H(z)| = 20\ log_{10}\left|\frac{Y(z)}{X(z)}\right| \quad (4\text{-}15)$$

where:

$Y(s)$: output signal

$X(s)$: input signal

The phase response of the filter is:

$$\emptyset(s = j\omega) = \angle H(s = j\omega) \quad (4\text{-}16)$$

4.4.2 Cutoff frequency

The cutoff frequency may be set according to several criteria. A common criterion is the half-power point, which is the frequency in which the power of the signal is reduced to half of its peak value. For the signal itself, it is the same as the amplitude being reduced to $\frac{1}{\sqrt{2}} \approx 0.707$ of its peak value. The attenuation using this criterion is $-3dB$, as in:

$$Gain_{dB} = 20\ log_{10}\left(\frac{1}{\sqrt{2}}\right) \approx -3dB \quad (4\text{-}17)$$

Standard filter design tools usually consider this cutoff frequency set at the passband corner frequency.

4.4.3 Finite impulse response (FIR) filters

The output of an LTI system is the convolution of the input with the impulse response coefficients of the system [58]. The difference equation of an FIR filter can be given by:

$$y(n) = \sum_{k=0}^{K} b(k)\ x(n-k) \quad (4\text{-}18)$$

where:

$y(n)$: current output of the filter

$x(n-k)$: current and past inputs

b: coefficients of the filter

k: index of the coefficients

K: filter order

Applying the Z-transform, we get the equivalent transfer function in its discrete complex frequency-domain form:

$$H(z) = \sum_{k=0}^{K} b(k)\, z^{-k} \tag{4-19}$$

The phase shift or phase delay of a filter depends only on the phase response at a particular frequency of interest and is defined as:

$$\tau_{\emptyset}(\omega) = \frac{-\emptyset(\omega)}{\omega} \tag{4-20}$$

where:

$\emptyset(\omega)$: phase response at frequency ω

The group delay of a filter is calculated by differentiating the phase response with respect to the frequency. It can then be defined as:

$$\tau_g(\omega) = \frac{-d\emptyset(\omega)}{d\omega} \tag{4-21}$$

Virtually any filter response can be achieved by means of an FIR filter. When it comes to user-defined responses, this can be a major advantage. However, a high number of taps may be necessary, which results in higher delays. From equation (4-19), we can see that the transfer function has no poles, which is an assurance of stability. This can also be observed from equation (4-18), in which the output of the filter does not depend on previous outputs, meaning there is no feedback. This feature also results in finite-precision errors not being amplified. Another advantage is the possibility to ensure a linear-phase response, for applications in which it is important to maintain a constant delay for different frequencies (both $\tau_{\emptyset}$ and τ_g are constant). When it comes to sub-synchronous oscillations, a linear-phase response is not necessary for most applications, except when there is an intention to keep track of more than one frequency at the same time or when there is a possibility of disturbances happening at two different frequencies in the same event. Finally, many developers will consider the main advantage of FIR filters the possibility of implementation in most digital signal processing (DSP) and

FPGA units due to the easy implementation using integer math. This opens the possibility of using low-power/cost devices.

4.4.4 Infinite impulse response (IIR) filters

The difference equation of an IIR filter is given by:

$$y(n) = \frac{1}{a(0)}\left(\sum_{k=0}^{K} b(k)\, x(n-k) - \sum_{l=1}^{L} a(l)\, y(n-l)\right) \tag{4-22}$$

where:

$y(n)$: current output of the filter

$x(n-k)$: current and past inputs

b: forward coefficients of the filter

K: feedforward filter order

$y(n-l)$: past outputs

a: reverse coefficients of the filter (usually: $a(0) = 1$)

L: feedback filter order

Applying the Z-transform, we get the equivalent transfer function in its discrete complex frequency-domain form:

$$H(z) = \frac{\sum_{k=0}^{K} b(k)\, z^{-k}}{1 + \sum_{l=1}^{L} a(k)\, z^{-k}} \tag{4-23}$$

The phase delay and group delay given by equations (4-20) and (4-21) also apply to IIR filters.

One may implement an FIR filter and an IIR filter with comparable magnitude responses. However, what is often considered the main advantage of IIR filters is that they usually require less multiply-accumulate (MAC) instructions, which means they require lower-order transfer functions. This is especially important for real-time applications, in which time is a limiting factor for all steps of signal and data processing. On the other side, very specific user-defined frequency responses are usually more difficult in these types of filters and stability becomes a concern due to the presence of poles in the transfer function. This is due to the presence of feedback, which can be seen

in equation (4-22). Past outputs are multiplied by reverse coefficients and subtracted from the response taken from the current and past inputs.

4.4.5 Stability

While FIR filters are stable by nature due to the lack of poles, IIR filters have poles that bring feedback in the time domain. Positive feedbacks may cause amplification of changes in the input signal and subsequent loss of stability. However, we can ascertain stability if we place the poles inside the unit circle of the *z-plane*.

4.4.6 Phase shift

The application of detection of sub-synchronous oscillations may have different ranges of frequencies that we want to get a better response. In the case of sub-synchronous control interaction (SSCI), all previous actual cases and most of the SSCI studies in the literature have shown that usual wind-farm and grid parameters lead to frequencies of oscillation below 30 Hz. In the active power signal, such signals will appear as above 30 Hz (complementary frequency to the fundamental – see Appendix C for detailed information). Therefore, for SSCI applications, the filter design can focus on reducing the time delay in the range below 30 Hz, if using the voltage or current signal as input, or above 30 Hz, if using the power signal as input. We can then relax this constraint in the remaining part of the sub-synchronous range.

4.4.7 Causality

A filter is said to be causal if it only depends on present and/or past outputs. Filters that depend on future outputs are non-causal. Moreover, a system can only be realizable, that is, it can only be implemented for real-time systems, if it is causal.

In order to build a causal filter, one possible approach is to design a filter without the causality requirement and then apply shortening and delaying to make it causal [65]. Shortening is the process of applying a window function to the filter function, therefore shortening its length. Subsequently, if the filter still depends on up to the ${N_{dl}}^{th}$ future sample, delaying should be performed by introducing a time-shift – i.e., a delay – of N_{dl} samples in the input signal such that $x(n) = x(n - N_{dl})$.

4.4.8 Phase linearity considerations

A linear-phase filter has a linear phase response as a function of frequency. As a result, all frequency components are shifted by the same value, which is equal to the group delay $\tau_g(\omega)$, which is constant in this case. A linear phase is only necessary if no phase distortion is acceptable, such as in audio signals. However, SSR detection systems do not have such a requirement. The system needs to detect the SSR frequency independently of delays between the various frequencies present in the signal. Therefore, the filter does not have to be linear-phase and the design can be focused on reducing time delays.

4.4.9 Minimum-phase filters

Real-time applications require minimization of time delays. This can be achieved by means of a minimum-phase filter, also known as a minimum-delay filter. For the same amplitude response, these filters have less delay than linear-phase filters at the expense of phase distortion, which is an acceptable feature for SSR detection systems. A minimum-phase filter has all zeros and poles inside the unit circle.

4.4.10 Attenuation

The minimum attenuation will depend on the steady-state or nominal value of the input signal and the threshold for pickup in the SSR protection/mitigation scheme. It is expected that some margin is considered. We then have:

$$Gain_{dB}(f) = 20\ log_{10}\left(\frac{X_{pickup} * Mg}{X_n}\right) \tag{4-24}$$

where: X_n: steady-state or nominal value of the signal

X_{pickup}: pickup value used in the protection/mitigation system

Mg: between 0% to 100%

As an example, take the active power as an input signal with a steady-state level of 200 MW at the point of measurement. If we use a pickup threshold of 5 MW and Mg=50%, applying the attenuation equation, the gain level in decibels for the DC component should be:

$$Gain_{dB}(f) = 20\ log_{10}\left(\frac{5 * 0.5}{200}\right) = -38.06\ dB$$

The same reasoning can be applied to the fundamental frequency component (60 Hz) of the voltage or current signals taking into account their nominal values.

4.4.11 Roll-off

The rate at which the transition between the bandpass and stopband occurs depends on the requirements of the transition band length and depends on the input signal, as described in item "4.5 - Input signal".

4.4.12 Bandpass and stopband ripple

Non-ideal filters have ripples in both the passband and stopband or in one of them. It highly depends on the type of filter that is being used. If we want to know the frequency of sub-synchronous oscillation with high accuracy, a flat response is needed in the passband. On the other side, if we allow some ripple (on either the stopband or passband or both), we can either reduce the order of the filter (therefore reducing time delay and complexity) or increase the roll-off between the stopband and passband.

4.4.13 Filter order

The order of a filter is taken as the delay in number of samples necessary to produce its output. Take the general difference equation of an IIR filter, herein repeated:

$$y(n) = \frac{1}{a(0)}\left(\sum_{k=0}^{K} b(k)\ x(n-k) - \sum_{l=1}^{L} a(l)\ y(n-l)\right) \qquad \text{Equation (4-22)}$$

The filter depends on, besides the current input, past samples of both the input and output signals. The order of the filter is, therefore, the larger of K and L. It can also be calculated as the order of the transfer function.

The higher the order of the filter, the more precise will the desired response be. High-order filters can achieve steeper – and therefore shorter - transition bands between

the passband and the stopband (higher roll-off). They can also decrease any ripples in the output signal where necessary. However, these always come at the expense of additional delays, so a tradeoff is necessary when dealing with time-critical systems. A good design will not attempt to set the maximum possible attenuation in the stopband, shorten the transition band as much as possible, and nullify any ripples. A good design will attempt to set the necessary attenuation, transition bandwidth, and ripple so as to meet the minimum requirements of the application that will provide the desired performance while attempting to maintain the lowest possible filter order. In this way, we can minimize the time delay.

4.4.14 Standard IIR design methods

The following design methods for IIR filters provide good responses as initial designs and they are usually available in software such as MATLAB or LabVIEW.

4.4.14.1 Butterworth

The Butterworth filter is designed to provide a frequency response without ripples in both the passband and stopband, as shown in Fig. 4.6 for a generic Butterworth lowpass filter.

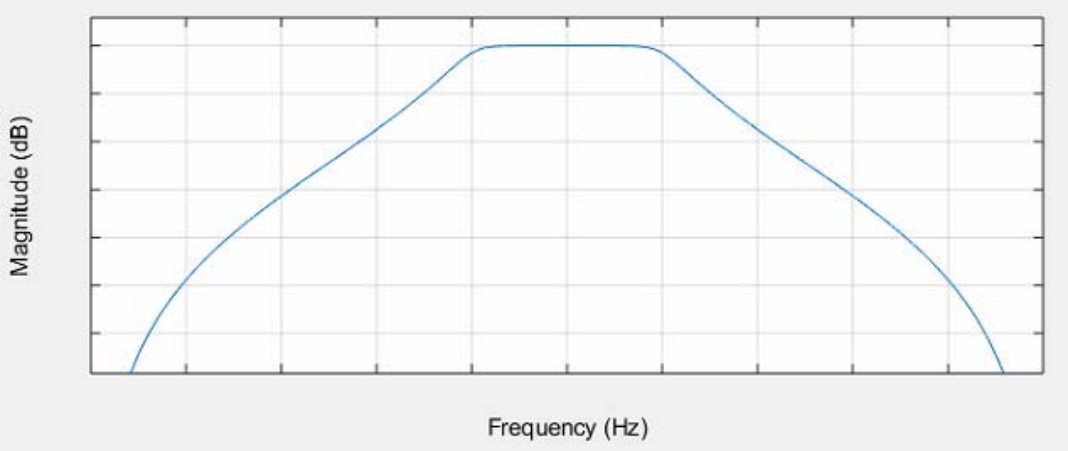

Fig. 4.6: Generic Butterworth lowpass filter.

4.4.14.2 Chebyshev type I

For the same desired filter order, the Chebyshev type I filter is able to provide a steeper roll-off than the Butterworth filter at the expense of some ripple in the passband.

The ripple can also be part of the design process. Fig. 4.7 shows a generic Chebyshev Type I lowpass filter.

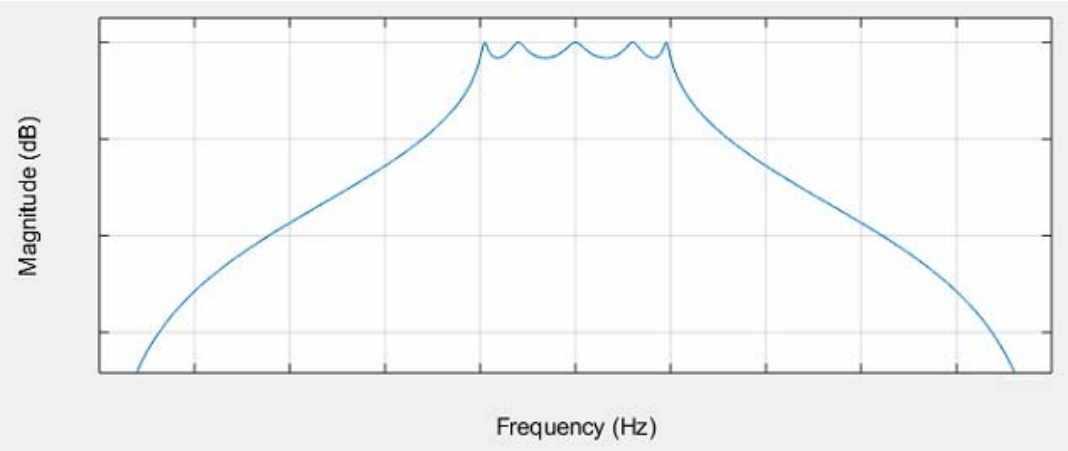

Fig. 4.7: Generic Chebyshev Type I lowpass filter.

4.4.14.3 Chebyshev type II

This type is also called Inverse Chebyshev filter and also provides a steeper roll-off than the Butterworth filter, but at the expense of some ripple in the stopband. Fig. 4.8 shows a generic Chebyshev Type II lowpass filter.

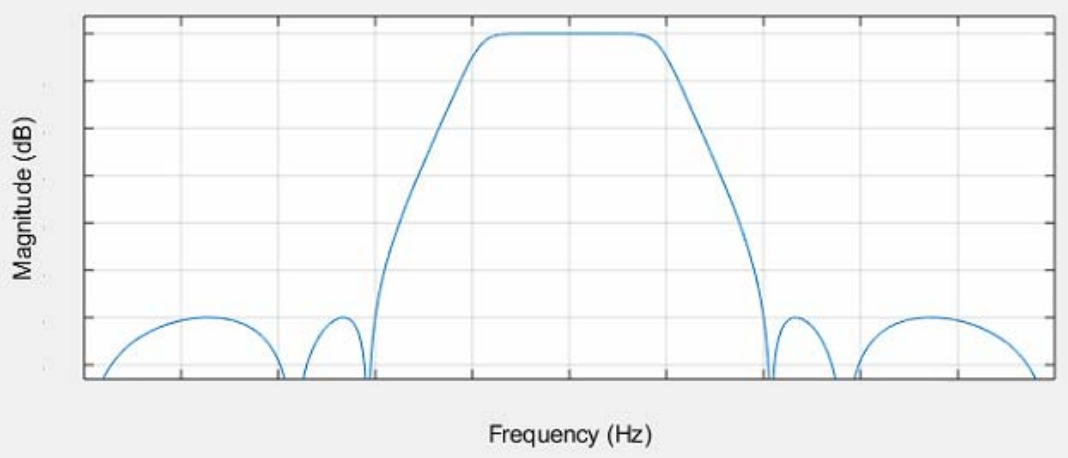

Fig. 4.8: Generic Chebyshev Type II bandpass filter.

4.4.14.4 Elliptic

The elliptic filter provides the steepest roll-off between the passband and stopband for a given filter order at the expense of ripples in both the passband and stopband, both independently adjustable. Fig. 4.9 shows a generic Elliptic lowpass filter.

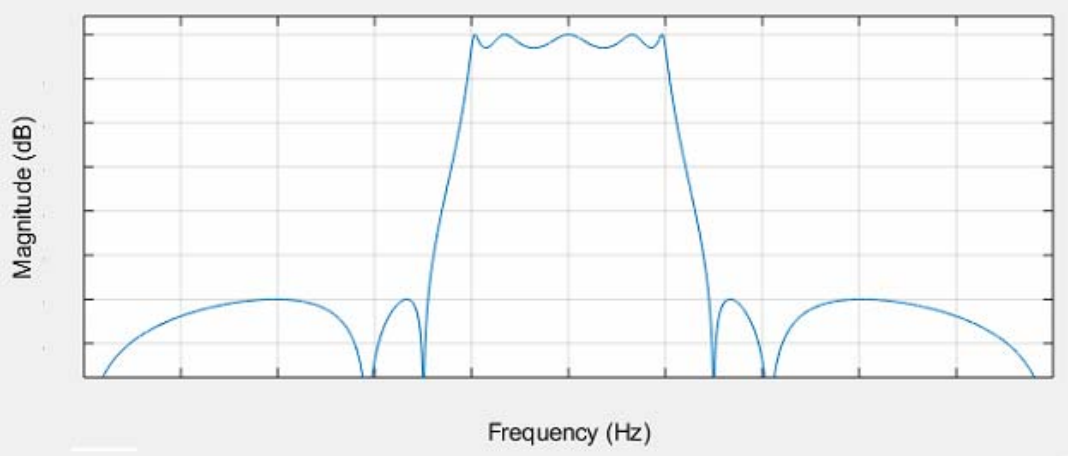

Fig. 4.9: Generic Elliptic bandpass filter.

4.5 Input signal

Sub-synchronous oscillation monitoring systems may use different signals as input. Different considerations must be made depending on the choice, especially when tuning the filters for signal conditioning. Sub-synchronous oscillations can be observed in the voltage, current, active power, and reactive power signals. Measurement points usually include the terminals of the wind generators and the point of interconnection (POI) with the rest of the electrical network after the collector system of the wind farm. SSO can also be measured at other points of the grid, although these should be carefully decided in the planning/risk assessment phase of the monitoring/mitigation/protection system in order to include the points with higher risks of SSR effects. No matter which signal is used as input for the detection system, filters should mainly keep only the sub-synchronous range of the signal, which is usually around 10%-90% of the synchronous frequency. For a 60 Hz system, it is common to consider a range of $f_{SSO,low} = 5\ Hz$ to $f_{SSO,high} = 55\ Hz$.

Some detection systems use the voltage as the input signal. Although it is possible to detect SSO in the voltage signal, the amplitude of the oscillation is usually lower relative to the normal steady-state signal levels than the oscillation that appears in the current signal [3]. The active power output signal is also a possibility for the input signal and oscillations can be easily seen due to the lack of an oscillating synchronous frequency in steady-state conditions. The three-phase instantaneous power is given by:

$$p(t) = v_a(t)i_a(t) + v_b(t)i_b(t) + v_c(t)i_c(t) \quad (4\text{-}25)$$

In steady-state, the active power signal will appear as a DC-only component, unlike the voltage and current signals, which contain a 60 Hz component. Sub-synchronous frequencies f_{SSO} in the voltage/current will appear in the power signal as the complementary frequency to the synchronous frequency, as follows (see Appendix C for detailed information)

$$f_{SSO,power} = 60 - f_{SSO} \quad (4\text{-}26)$$

where: $f_{SSO} = f_{SSO,voltage/current}$

Besides setting the filters to remove frequencies out of the sub-synchronous range, special attention needs to be taken for the following cases:

- Voltage/current signal
  - Due to the presence of a 60 Hz component in steady-state, the low-pass filter needs to have a sharp roll-off above $f_{SSO,high}$, as these frequencies are relatively close. Lowpass filters with sharp roll-offs are achieved using high-order filters, which can cause delays that affect the detection response;
  - A highpass filter removing frequencies below $f_{SSO,low}$ can be used to remove possible exponential/DC components during/after transients in the current signal (e.g. short-circuit, switch operations);
- Power signal
  - Due to the presence of a DC component in steady-state, the highpass filter needs to have a sharp roll-off below $(60 - f_{SSO,high})$, as these frequencies are relatively close. This also removes misinterpretation of other phenomena, such as low-frequency oscillation (related to the stability of interconnected systems and generators), which is usually seen as 1-3 Hz oscillations in the power signal. When comparing to a lowpass filter with

the same roll-off and same transition band, highpass filters usually require lower-order filters, which is a good feature to reduce delay;

- A lowpass filter needs to have a maximum high cutoff frequency of $(60 - f_{SSO,low})$ to remove any possible unwanted components, such as noise. In this case, the roll-off may not need to be extremely sharp, as normally there is no strong presence of components near the high cutoff frequency. Although the voltage and current signals are traditionally used as input signals for various power system protection functions, including sub-synchronous oscillation functions, this feature, along with the previously described feature, makes the power signal a good candidate for SSO detection due to the simpler and faster filters that can be used with less sharp roll-offs, which also help reduce delays;
- Utilization of the active power signal with the complementary frequency of SSCI allows for more numbers of complete analyzing cycles for the cases with frequencies of oscillation under 30 Hz (which is the case for all actual past events until the time of writing this document), as they will appear as a higher than 60-30=30 Hz signal in the active power, that is, the active power will have a higher frequency component than the voltage/current signals (e.g., a sub-synchronous oscillation that appears with a frequency of 15 Hz in the voltage/current signal will appear with a frequency of 60-15=45 Hz in the active power signal, thus more cycles are present in the power signal). This allows for improving the quality of the signal processing.
- Usually more visible to the naked eye: the oscillations are usually easy to see in the power signals, as the steady-state signal is normally only a DC component.

4.6 Matrix pencil detection algorithm

Eigenvalue analysis involves detailed modeling of the system and, in order to implement linear feedback control, the system size must be limited, often requiring system size reduction, which is also necessary due to the high computational burden (in a state-space representation it could mean matrices in the order of several hundreds). This

reduction risks loss of modal content and parameterization of the system becomes complex and, many times, infeasible. In reality, parameters may even drift over time and are dependent on operating conditions.

The matrix pencil (MP) method is an estimation technique of the linear model of the system for eigenvalue analysis and system identification. It uses the system output response and can be implemented for real-time applications. The varying parameterization over time allows for the inclusion of nonlinearities. The order of the model may be directly chosen to be lower, which will retain the most dominant modes up to the chosen order. It is also possible to implement the MP method with mechanisms that enable varying order of the estimated linearized system, which makes it possible to retain the dominant modes while reducing the computational burden. A system with hundreds of modes can, therefore, be represented by an estimated linearized system with only a few modes, making it appropriate for real-time applications.

Consider a state-space representation of a linearized system [61]:

$$\begin{aligned} \dot{\boldsymbol{x}} &= \boldsymbol{A}\boldsymbol{x} + \boldsymbol{B}\boldsymbol{u} \\ \boldsymbol{y} &= \boldsymbol{C}\boldsymbol{x} + \boldsymbol{D}\boldsymbol{u} \end{aligned} \tag{4-27}$$

where:

$\boldsymbol{x}$: state vector of the system

$\dot{\boldsymbol{x}}$: differentiation of x

$\boldsymbol{u}$: input vector

$\boldsymbol{y}$: output vector

The discrete form of (4-27) is:

$$\begin{aligned} \boldsymbol{x}(n+1) &= \boldsymbol{A}\boldsymbol{x}(n) + \boldsymbol{B}\boldsymbol{u}(n) \\ \boldsymbol{y}(n) &= \boldsymbol{C}\boldsymbol{x}(n) + \boldsymbol{D}\boldsymbol{u}(n) \end{aligned} \tag{4-28}$$

Let each state of the system be:

$$x_m(t) = \sum_{m=1}^{N} r_m \, x_{m0} e^{\lambda_m t} \tag{4-29}$$

where:

N: number of modes

m: mode index

r_m: residue of mode m

x_{m0}: derived from the influence of initial conditions

λ_m: eigenvalue of mode m of matrix A from equation (4-27)

If we represent equation (4-29) as:

$$x_m(t) = \sum_{m=1}^{N} a_m \, e^{\sigma_m t} \cos(\omega_m t + \theta_m) \tag{4-30}$$

We can then represent the output as:

$$y(t) = \sum_{m=1}^{N} A_m \, e^{\sigma_m t} \cos(\omega_m t + \theta_m) \tag{4-31}$$

A polynomial modal method, such as the Prony method, would estimate the parameters in (4-31) by fitting a function to actually observed outputs of $y(t)$. At sample time t_n, the discrete form of (4-31) is:

$$y(n) = \sum_{m=1}^{k} B_m \, z_m^n \tag{4-32}$$

where:

$k \leq N$: number of eigenvalues to be determined

The eigenvalues λ_m of each mode m are associated with z_m by:

$$z_m = e^{\lambda_m \Delta t} \tag{4-33}$$

z_m are the roots of the following equation, which have associated coefficients a_m:

$$z^k = a_1 z^{k-1} + a_2 z^{k-2} + \cdots + a_{k-1} z^0 \tag{4-34}$$

Therefore, if we solve (4-34) for z_m, we can get the eigenvalues by writing equation (4-33) as:

$$\lambda_m = \frac{\ln(z_m)}{\Delta t} \tag{4-35}$$

Finally, we have, for each mode m:

$$\begin{aligned} \text{Frequency in radians} &= \text{Im}(\lambda_m) \\ \text{Damping factor} &= \text{Re}(\lambda_m) \end{aligned} \tag{4-36}$$

Therefore, it is possible to not only determine the possible frequencies of oscillation, but also the damping factors associated with each mode, which gives an indication of the stability of the system. Positive damping factors indicate unstable systems (eigenvalues at the right-half side of the R-X plane).

Polynomial methods use the outputs of the system to fit a polynomial into equation (4-34). The coefficients a_m are built from the set of measurements and the solution of the equation will give the poles z. Differently, instead of finding the poles by fitting a function to equation (4-34), the matrix pencil method utilizes single value decomposition (SVD) of a truncated Hankel matrix formed from the outputs of the system. This method is more computationally efficient, has better estimation properties, and is less sensitive to noise. It consists of solving for the eigenvalues of a matrix in the form [62]:

$$\boldsymbol{g}(n) - \lambda_z \, \boldsymbol{h}(n) = (\boldsymbol{h}(n)^{+} \, \boldsymbol{g}(n) - \lambda_z \, \boldsymbol{I}) \tag{4-37}$$

where:

$\boldsymbol{g}(n)$ and $\boldsymbol{h}(n)$ are matrices formed from the outputs of the system

$\boldsymbol{I}$: identity matrix

λ_z: eigenvalues of equation (4-37)

$^{+}$: Moore-Penrose pseudo-inverse operator

The eigenvalues of (4-37) are not the eigenvalues of the overall system. They are equivalent to the poles of equation (4-34) of the polynomial method. Then, after applying (4-35), we are able to find the eigenvalues of the overall system.

Despite the presence of numerous eigenvalues in the system, many of them may be insignificant or are noise-related. Hence, the order of matrices $\boldsymbol{g}(k)$ and $\boldsymbol{h}(k)$ are made variable and dependent on how many singular values are large enough when compared to the largest one after applying SVD. This increases computational efficiency and reduces sensitivity to noise. References [61] and [62] provide more details regarding the implementation of the algorithm.

4.7 Proposed detection algorithm: power spectrum + frequency/magnitude/derivative estimators

Several techniques for sub-synchronous oscillation detection have been proposed in literature. Different methods include the application of phasor measurement units (PMU), non-linear time-series analysis, signal envelope filters, logic-based algorithms, and ringdown analysis, among others [30]. This sub-item will describe a proposed method that utilizes the power spectrum calculation along with frequency and derivative estimators.

The DFT calculation from equation (4-7) applied to a signal $x(t)$ that is discretized to $x(n)$ results in a complex output sequence of the form:

$$x(k) = x_{Re}(k) + jx_{Im}(k) \tag{4-38}$$

where:

x_{Re}: real component of x

x_{Im}: imaginary component of x

$k = 0, 1, \dots, N-1$: index of each frequency bin

When the input data is purely real (which is the case of measurement sampling from instantaneous voltage/current/active power/reactive power), we can apply the symmetry property, which states that:

$$x(N-k) = x(-k) \tag{4-39}$$

where the $(N-k)^{th}$ element of x contains the result of the $-i^{th}$ harmonic. In this case, the i^{th} and $-i^{th}$ harmonics are complex conjugates, hence:

$$x(N-k) = x(k)^* \tag{4-40}$$

Therefore:

$$\begin{aligned} x_{Re}(k) &= x_{Re}(N-k) \\ x_{Im}(k) &= -x_{Im}(N-k) \end{aligned} \tag{4-41}$$

In the above equations, for an even number of samples N, we have the following indices for the frequency bins:

$k = 0$: index of DC component

$1 \leq k \leq \frac{N}{2} - 1$: indices of positive frequencies

$k = \frac{N}{2}$: index of Nyquist frequency (last representable positive frequency)

$\frac{N}{2} + 1 \leq k \leq N - 1$: indices of negative frequencies

In the case of an odd number of samples N, we have:

$k = 0$: index of DC component

$1 \leq k \leq \frac{N-1}{2}$: indices of positive frequencies

$\frac{N-1}{2} + 1 \leq k \leq N - 1$: indices of negative frequencies

The fast Fourier transform (FFT) is a DFT method that can be implemented for real-time applications and takes into account the symmetry between positive and negative frequencies to obtain an efficient algorithm that does not calculate redundant components [58].

The total power of the signal $x(t)$ through the calculation of its mean squared amplitude is, using time-domain quantities [63]:

$$S_x = \frac{1}{T}\int_0^T |x(t)|^2 dt \approx \frac{1}{N}\sum_{n=0}^{N-1} x(n)\, x(n)^* = \frac{1}{N}\sum_{n=0}^{N-1} |x(n)|^2 \tag{4-42}$$

From the FFT results, we can estimate the power spectrum of the signal in the frequency domain (i.e., the power in each frequency bin) using the periodogram method. This method applied to equation (4-42) and already considering (4-40) gives:

$$S_x(k)|_{N=even} = \begin{cases} \frac{1}{N^2}|x(k)|^2, & k = 0 \\ \frac{1}{N^2}[|x(k)|^2 + |x(N-k)|^2], & k = 1, 2, \dots, \left(\frac{N}{2} - 1\right) \\ \frac{1}{N^2}|x(k)|^2, & k = \frac{N}{2} \end{cases} \tag{4-43}$$

$$S_x(k)|_{N=odd} = \begin{cases} \frac{1}{N^2}|x(k)|^2, & k = 0 \\ \frac{1}{N^2}[|x(k)|^2 + |x(N-k)|^2], & k = 1, 2, \dots, \left(\frac{N-1}{2}\right) \end{cases}$$

where the frequency bins k are defined for only the zero and positive frequencies.

From the power spectrum, we can detect any oscillations in the power system in the sub-synchronous range. This method does not need to deal with complex matrix calculations with variable size as in the matrix pencil method and can be very computationally efficient, which is a significant advantage for real-time applications. However, for the same number of samples, the FFT has a very low frequency resolution. If the sampling frequency of the discretized signal is $f_{sr,down}$ (after signal conditioning), the frequency resolution of the N-point FFT (and therefore of the power spectrum) is:

$$\Delta_{f_{FFT}} = \frac{f_{sr,down}}{N} \tag{4-44}$$

The frequencies $f_x(k)$ of the FFT calculation are:

$$f_x(k) = k\Delta_{f_{FFT}} = k\frac{f_{sr,down}}{N} \tag{4-45}$$

where:

$k|_{N=even} = 0, 1, \dots, \frac{N}{2}$

$k|_{N=odd} = 0, 1, \dots, \frac{N-1}{2}$

For better illustration, take a signal sampled at $f_{sr,down} = 320\ Hz$ and a number of samples $N = 16$. The window length is:

$$Window\ length|_{N=16}^{f_{sr,down}=320} = \frac{N-1}{f_{sr,down}} = \frac{15}{320} = 46.875ms$$

The frequency of resolution is:

$$\Delta_{f_{FFT}} = \frac{f_{sr,down}}{N} = \frac{320}{16} = 20\text{Hz}$$

Hence, the FFT results are given at frequencies:

$$f_x(k) = k\Delta_{f_{FFT}} = 20k = 0, 20, 40, 60, \ldots, 160 \text{ Hz}$$

Any frequency component present in the signal will be represented by one or more of these bins. If we take a 15 Hz signal, for example, the power of this signal will be spread in the representable bins (0, 20, 40, and so on).

For the same sampling rate, in order to increase resolution, the number of samples must be larger. If we increase N from 16 to 32 samples, the window length will increase from 15/320=46.875 milliseconds to 31/320=96.875 milliseconds, which is a considerable increase that will negatively impact the detection time, while the frequency resolution has only been reduced to 320/32=10 Hz.

In order to get a higher frequency resolution and more accurate corresponding magnitudes (which are related to the power at each frequency bin), we must correct the aliasing errors without having to increase the number of samples in the window so as to not affect the detection time. When using short windows, the reduced frequency resolution can be overcome by estimating the actual frequency present in the signal by using a weighted average of the power contained in the main detected bin and a few side bins as follows:

$$f_{corrected} = \frac{\sum_{k=m-l}^{m+l} S_x(k) * f_x(k)}{\sum_{k=m-l}^{m+l} S_x(k)} \tag{4-46}$$

where:

$f_{corrected}$: corrected detected frequency

m: index of the main bin

l: number of side bins considered in each side of the main bin

The estimated power at the corrected frequency is:

$$S_{corrected} = \frac{\sum_{k=m-l}^{m+l} S_x(k)}{ENBW} \tag{4-47}$$

where:

$ENBW$: equivalent noise bandwidth

The ENBW is set accordingly to the tapered window function used, as shown in Appendix A.

As the power spectrum does not have an intrinsic calculation of the damping factor of the mode associated with the oscillation, we must implement some mechanism to assess its stability characteristics. It is possible to evaluate the derivative of the detected magnitude over time. A positive value indicates that the oscillation is growing, rendering the system unstable. A negative value indicates that the oscillation is decreasing, rendering the system stable. A derivative value of zero may be used as an indication of sustained oscillations.

Considering the output results are given for every new sample n, we may approximate its derivative by using finite differences [64]. For a function F, a first-order centered difference with a second-order error is given by:

$$F'(n) = \frac{F(n+h) - F(n-h)}{\Delta T_{sr,down}\, 2h} + O(h^2) \tag{4-48}$$

where:

F: output function

n: sample index

h: time length in number of samples above/below the current time

$\Delta T_{sr,down} = \frac{1}{f_{sr,down}}$: time interval between samples

$O(h^2)$: error (of order two in this case)

The approximate finite difference to the derivative in equation (4-48) is obtained by throwing away the error term $O(h^2)$. If we use $h = 1$ sample, we have:

$$F'(n) \cong \frac{F(n+1) - F(n-1)}{2\,\Delta T_{sr,down}} \tag{4-49}$$

The above function is not causal, so a delay of one sample needs to be applied for real-time applications, as follows:

$$F'(n) \cong \frac{F(n) - F(n-2)}{2\,\Delta T_{sr,down}} \tag{4-50}$$

4.8 Output post-processing

Different applications will require different manipulation of the output data from the detection algorithm. If the goal is post-event analysis, we may keep all the output data intact.

If it is applied for real-time protection/mitigation systems, a few things need to be considered:

1. The trip signal can only be issued after a certain amount of time in which a sub-synchronous oscillation is detected. Possible criteria are [30]:
    a. Frequency of oscillation within the sub-synchronous range (e.g., 5 Hz to 55 Hz for a 60 Hz system);
    b. Magnitude of oscillation above:
        i. a certain threshold M_{th1} and the derivative of the magnitude (or the damping factor - depending on the technique used) is positive; or
        ii. a certain threshold $M_{th2} > M_{th1}$. In this case, the derivative of the magnitude (or the damping factor) is not considered due to the extremely high level of the magnitude of oscillation. Even if there is a negative damping factor associated, it may not be enough to cause fast decay of the oscillation;
    c. All the above criteria are met for a certain time or number of samples, for example:
        i. length of the window; or
        ii. length of the window plus a few cycles (1-3 cycles) of the synchronous frequency;
2. The results are updated for every new input sample received;
3. The detected magnitude may be corrected according to the filter response. This may be especially necessary to correct for attenuations within the considered sub-synchronous range due to the fact that the filter is not ideal. The correction can be calculated for $Y_{corrected}$ according to the following equation:

$$Gain_{dB}(f) = 20\ log_{10}\left(\frac{Y_{detected}}{Y_{corrected}}\right) \quad (4\text{-}51)$$

where:

f: detected frequency at the current sample

$Y_{detected}$: detected magnitude at the detected frequency

$Y_{corrected}$: corrected magnitude at the detected frequency

To better illustrate this method, consider a second-order IIR bandpass Butterworth filter with the cutoff attenuation set at the half-power point (-3 dB); a low cutoff frequency of 5 Hz; and a high cutoff frequency of 55 Hz. The magnitude response is shown in Fig. 4.10:

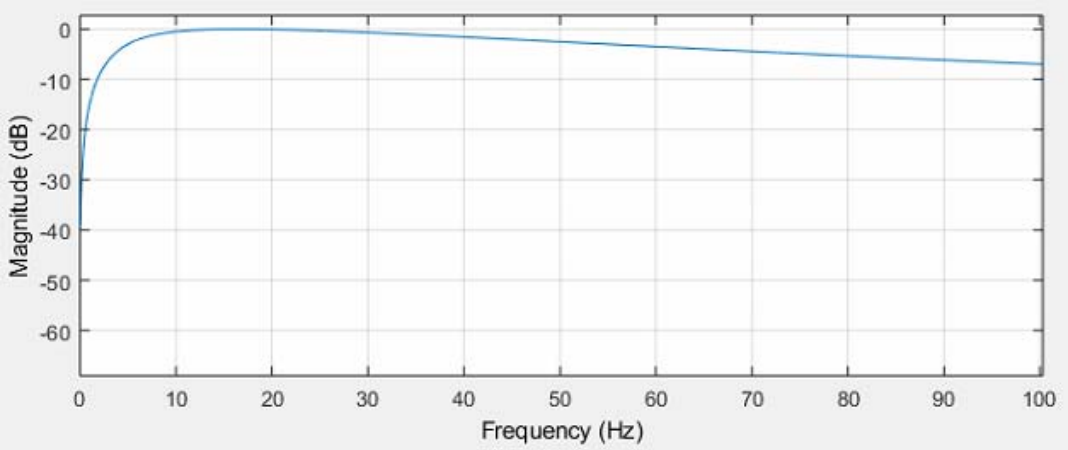

Fig. 4.10: Second-order Butterworth filter with passband from 5 to 55 Hz.

Take a detected voltage signal with a frequency of 45 Hz and a detected magnitude of 10 kV. At 45 Hz, the gain is -2 dB. According to equation (4-51), we have:

$$Gain_{dB}(45Hz) = 20\ log_{10}\left(\frac{Y_{detected}}{Y_{corrected}}\right)$$

$$-2 = 20\ log_{10}\left(\frac{10}{V_{corrected}}\right)$$

$$Y_{corrected} = 12.59\ kV$$

The voltage is then corrected from 10 kV to 12.59 kV. This correction is performed for every sample to maintain the criterion of the magnitude threshold coherent at all times.

4.9 Field implementation considerations

The proposed detection module can be placed at any point of the grid that has a potential for sub-synchronous control interaction phenomena (turbine/inverter level, POI or series capacitor level). The algorithm can be implemented after each wind turbine generator (WTG), as part of the generator's protection, or at the POI. In the case that protection is implemented at the WTG, there is no need for coordination with any other protection devices. The SSCI protection would trip only the affected WTG (meaning there is no grid behind it), therefore not opening any part of the circuit downstream, which means other WTGs and the transmission line will not be affected. Another possibility is placing the module at the POI. In this case, no coordination would be necessary with protection devices after the POI (toward the grid), that is, no coordination is necessary with the transmission line protection. However, coordination would be necessary with the WTGs protection settings, in case there are any, as they would be upstream. If there is no protection at the WTG level, then the whole wind farm will be tripped in the case of SSCI. If there is protection at the WTG level, its protection settings would need to have more sensitive settings so as to issue a trip signal faster than the POI level settings, therefore avoiding tripping of the whole wind farm. This time coordination can be achieved by adjusting the magnitude threshold and the minimum detection time. One could also use curves with tripping times dependent on the magnitude of the oscillation, similar to the ones of overcurrent relays, and perform the coordination settings accordingly. It should be noted that implementation at the WTG level requires separate SSCI analysis for each WTG, which considerably increases the volume of SSCI analysis. In this case, the expected frequency range remains the same, as the resonant modes of the overall grid remain the same, although the damping would be different for each WTG.

5 REDUNDANT MONITORING SYSTEM

In this chapter, the design of a monitoring system that can be used for protection, mitigation and post-event analysis applications is described. All the signal processing and digital monitoring methods developed in chapter “4 - Sub-synchronous resonance detection system” are implemented within this system.

5.1 Introduction

Monitoring systems are one of the most important parts of almost any power system, either in the industrial field or in the power generation, transmission and distribution fields. They are able to provide real-time data and identify potential problems in the monitored system for protection/mitigation purposes, as well as provide historical data for all types of further analyses. While these systems are installed to make sure that the power system is working properly, they also need to be monitored and be reliable.

Reliability is a major concern in any system nowadays, and its assessment ranges from utility automation systems, such as in [66], to industrial automation applications, such as in [67]. The reader who is deeply interested in finding out more about reliability aspects - many of them used in this paper - should investigate reference [68].

Not all systems utilize FPGAs, thus simpler redundant schemes are necessary and they have fewer points of possible failures. Herein, the first proposal is a design of a CPU-FPGA heterogeneous platform that uses the advantages of both platforms, as described in section “4.1 - Processing technology”.

In current monitoring systems of power grids, redundancy studies are mainly focused on communication networks, device allocation and architecture. Study [69] applies the parallel redundant protocol (PRP) for a communication network in a distribution and generation microgrid system. The authors in paper [70] introduce methods for synchronization on a redundant communication network. Meanwhile, communication redundancy protocols have also been integrated into various power system monitoring and automation equipment by different companies, such as in [71]. Some other papers apply N-modular redundancy schemes, such as the triple modular redundancy (TMR) [72]. In [73], the reliability of systems is calculated for hardware triple and five-modular redundancy. In [74], dual modular redundancy (DMR) is developed in

an electronics level. In [75], a DMR design for general applications that require hardware redundancy is proposed.

In this work, redundancy was not only considered for communication networks and architectural designs, but also for the implementation of the inner mechanisms that monitor the monitoring system itself. Hence, as the second proposal of this paper, a DMR scheme was implemented along with a data storage redundancy scheme. The design has self-monitoring capabilities, which makes it an independent system with improvements in reliability [76]-[77].

5.2 CPU-FPGA heterogeneous platform

A CPU-FPGA heterogeneous platform-based monitoring system is herein proposed and implemented as a solution to get the best of both FPGA and CPU resources while costs are not increased drastically. The proposed monitoring scheme divides different functions according to Fig. 5.1 and the following subsections.

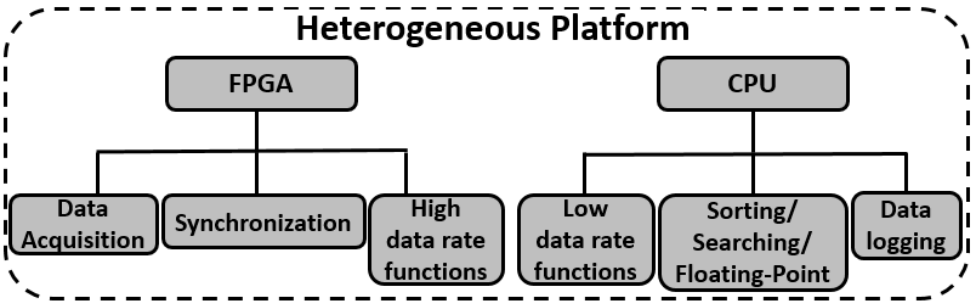

Fig. 5.1: CPU-FPGA heterogeneous platform.

5.2.1 Implemented on the FPGA

The first function better suited for FPGAs is data acquisition. When dealing with large quantities of data, the FPGA will be able to provide higher determinism than the CPU, especially when dealing with multiple I/Os. This is due to the features of parallel processing and of not usually responding to asynchronous events, which results in much more predictability [79].

The second function is synchronization between units in a monitoring system, either redundant units or other units. This is a time-critical task that should rely on the determinism and reliability provided by FPGAs.

Thirdly, functions that require a great number of calculations are also performed in the FPGA. In this way, many calculations and different functions can operate on their

own simultaneously due to the parallel processing capabilities. The signal processing and the SSR detection systems have to calculate new results for every new sample received, and are therefore best suited for the FPGA. The results are subsequently sent to the CPU, which receives a reduced volume of data and does not need to handle a high data rate.

5.2.2 Implemented on the CPU

Functions that do not require high data rates for processing are well suited for CPUs, which are non-deterministic. When an algorithm is implemented in the FPGA, logic resources are allocated for it, even if the algorithm is not being used. Thus, generally, functions that do not need to run continuously or are not frequent may be performed in the CPU. In this way, FPGA resources are not going to be idle most of the time. Thus, functions well suited for the CPU include data display, which may have a relatively low update rate (e.g., one update per second); and data logging, which is run when a sub-synchronous oscillation is detected in order to record data about the event for post-event analysis.

Finally, although not implemented in this project, it is interesting to note that some algorithms, such as the ones that use sorting/searching techniques, are sequential by nature, so they do not benefit from the use of parallel resources of FPGAs.

5.3 Dual modular redundancy

Having multiple pieces of hardware performing the same tasks can be one of the most reliable solutions when it comes to increasing the reliability of a system. Triple modular redundancy (TMR) is a popular scheme in which a sub-system is triplicated, and a single result is voted by a majority criterion, as shown in Fig. 5.2 [68]. However, triplicating pieces of hardware may be too costly. This is often the case for monitoring systems, which may use expensive hardware, especially when FPGA resources are needed in place of series-produced or non-customizable hardware. Dual modular redundancy is a way of achieving high degrees of reliability in a less costly solution, as it only duplicates pieces of hardware. An even number of sub-systems prevents it from using a majority-based voting system [68]. Hence, methods such as simply switching to the secondary system or self-voting techniques may be used. In the design proposed herein, this issue is resolved by building a health indicator for each device, which will be

detailed in section “5.5 - Self-monitoring schemes” of this chapter. The interested reader can find additional information on self-voting schemes in an electronics level in papers such as [74] and [80].

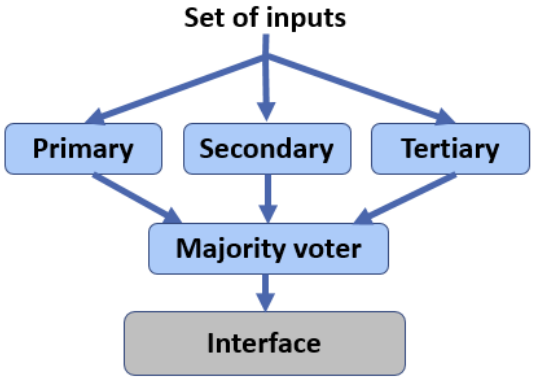

Fig. 5.2: TMR configuration with a majority voter switch.

Fig. 5.3 (a) shows a DMR configuration using a hardware voter. Whenever the primary unit fails, the system switches to the secondary unit through the voter switch. The proposed scheme, shown in Fig. 5.3 (b), eliminates the hardware voter, thus reducing the costs of the overall system and removing one possible point of failure (note that there is no duplication of the voter switch, which is usual). The voter is then not implemented in a hardware switch, but in software within the interface system. If the system will interface with equipment for control purposes, the interface with the voter needs to be installed in a real-time operating system (RTOS)

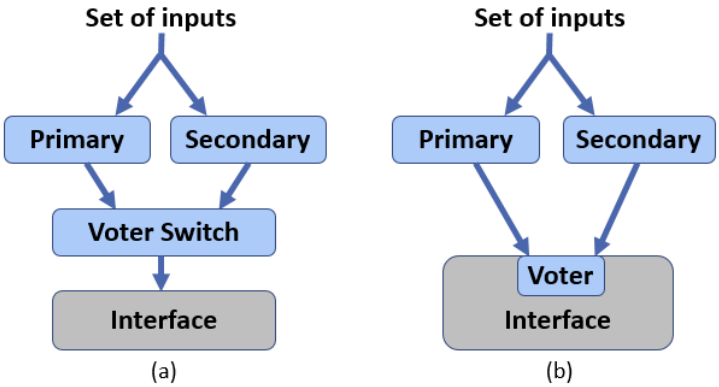

Fig. 5.3: (a) DMR configuration with hardware voter, (b) DMR configuration with software voter (proposed configuration).

In any DMR configuration, synchronization between units is necessary. This can be achieved using cabled synchronization, a solution that provides the best accuracy. However, timestamps are not referenced to a global source, i.e., it uses an internal clock. Besides that, the distance between units and other parts of the monitoring system to be synchronized is often a constraint, making the use of cables not viable. In these cases, it is still possible to achieve high accuracy using GPS synchronization, which enables the time-stamping of signals to a global standard [81]. This solution not only synchronizes two redundant units but also enables synchronization between any other units in a monitoring system that comprise large areas.

For the proposed GPS synchronization scheme, the acquisition sampling rate of both units must be the same. The GPS receiver update rate depends on the GPS module used. The standard for most receivers is 1 Hz. Hence, a standard module synchronizes with the GPS signal every second. An internal clock rate is used accordingly to the sampling rate with timestamps generated internally between the synchronization steps, as shown in Fig. 5.4. The timestamped waveform will slightly skew between synchronization update steps by a time Δt, so faster update rates will generate less skew and provide higher accuracy.

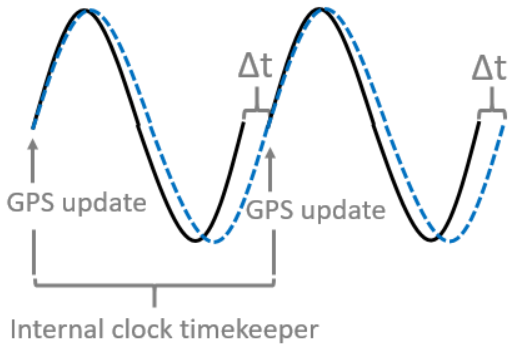

Fig. 5.4: An internal clock timekeeper timestamps each sample between GPS synchronization updates, when the skew Δt is then corrected.

5.4 Data redundancy

Regarding data storage, the proposed scheme achieves redundancy by using a network-attached storage (NAS). A NAS is basically a data storage server providing data access to various clients. Both primary and secondary units will continuously store data into the NAS. The data interface system can then retrieve data only from the dataset which

is deemed currently healthy and in use. In normal operation conditions, both datasets will be identical, but only one of them will be deemed active, whichever is signaled by the DMR scheme. A NAS with Redundant Array of Independent Disks (RAID) capabilities can not only provide improvements in data redundancy but also performance, depending on the configuration [68].

In a RAID 0 configuration, data striping (logically-sequential-data segmentation into different physical storage devices) is performed into all disks with concurrent reading/writing operations, improving performance, but with no added redundancy. In a RAID 1 configuration, data will be mirrored in two or more disks, thus with added data redundancy. Although there may be added reading performance, the writing performance remains the same or equal to the writing speed of the slowest disk.

The proposed configuration uses four disks in a RAID 10 (RAID 1+0) configuration, as shown in Fig. 5.5. Data striping is first performed between two pairs of disks (RAID 0) and then mirrored in each pair (RAID 1). In this case, we are able to achieve both redundancy and performance improvements. We must note that 50% of the storage capacity is used for new data, as the other 50% contains a copy of it. In this configuration, the loss of up to two disks will not result in loss of data, as long as they are not an exact mirrored pair of disks (i.e., disk 1 and 2 or disk 3 and 4).

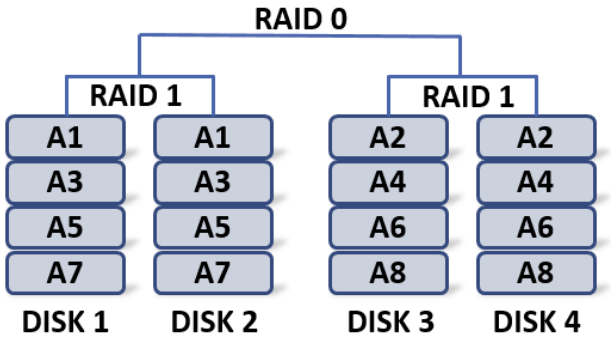

Fig. 5.5: RAID 10 configuration.

5.5 Self-monitoring schemes

This section focuses on self-monitoring schemes implemented in both units in the DMR configuration. Not only can a unit monitor some parameters in itself, but also in the other unit. Depending on which unit is currently active, which is herein understood as having its output dataset read by the subsequent subsystems, the decision of switching to

the other unit is made based on the voter decision, which takes into account a health indicator based on all self-monitoring schemes.

For the proposed design, a controller with a CPU running in an RTOS environment and an FPGA is used, as shown in the scheme in Fig. 5.6. The figure also shows the architecture of the proposed design. The gray thick arrows show the flow direction of the monitored equipment data. The FPGA collects the data through the input ports, sends them continuously and synchronously to the CPU. The data is then finally stored in the NAS through a network switch (which is different from the voter switch mentioned in previous items), from where the interface will get the information. The blue thin arrows show the flow of data related to self-monitoring schemes, which will be detailed in the following subsections. It should be noted that the I/O cards could interface with either the FPGA or the CPU, depending on the controller. In this case, we are taking advantage of the re-programmability and processing power of FPGAs. Hence, the monitored equipment data is collected through the FPGA.

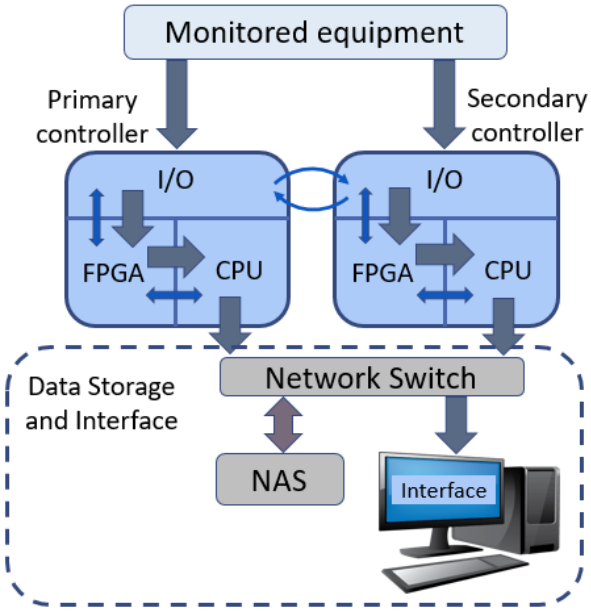

Fig. 5.6: Proposed complete DMR architecture and controller units.

5.5.1 Health indicator

Herein, the proposed design takes into consideration several self-monitoring schemes that will be described in the following subsections and builds a health indicator for each unit. The schemes are herein itemized:

1. Controller: CPU temperature
2. Controller: FPGA temperature
3. Controller: CPU usage
4. Controller: RAM usage
5. DC power supply
6. Controller power supply and battery
7. FPGA-FPGA monitoring scheme
8. CPU-FPGA monitoring scheme
9. CPU-CPU monitoring scheme
10. Time-out functions

In schemes 1, 2, 3, 4, and 8, each device monitors itself. In other words, the monitoring device and the monitored device are the same unit, that is, unit 1 is monitoring the parameters of unit 1, while unit 2 is monitoring the parameters of unit 2. In schemes 5, 6, 7 and 9, a cross-check is applied, that is, unit 1 monitors unit 2, while unit 2 monitors unit 1. Scheme 10 is applied within schemes 7, 8 and 9.

For each unit, each scheme may report a normal or abnormal status. If a unit has all schemes with normal status, its health indicator will be at 100%. Schemes 1 through 4 have either a warning level or a critical level. For each scheme, a warning level will drop the health by 5%, while a critical level will drop it by 10% in total. For schemes 5 through 10, an abnormality will drop the health by 10%.

5.5.2 Voter

For an N-modular redundancy scheme in which N is an odd number, one could simply use a majority-based voting system, for example in the case of a TMR scheme, in which N=3. However, in a DMR scheme, we have N=2, which is an even number, making it difficult to decide which unit should be active when they do not agree. To solve this impasse, one possible design is delegating the secondary unit as the only voter. In this case, the secondary unit would concentrate all the health information from both units in order to decide which one should be active. The only decision in the primary unit would be, if it does not receive any decision from the secondary, it makes itself the active unit

while sends out an alarm that the secondary has failed. Although this method is one possibility, the proposed design concentrates the health information in the interface system, which decides in real-time which dataset to forward to other real-time parts of the system, such as display, and which stored dataset is healthy (main unit or backup unit). If the health indicators from both units are equal, the main unit is considered the active one.

5.5.3 Controller temperature, CPU usage and RAM usage

One should always take advantage of the health parameters internally implemented in controllers. Temperature is usually one of them, both in the CPU and in the FPGA. Along with the hardware specifications, it is possible to set limits and forecast whether the controller will be reaching a temperature above acceptable. Considering that the manufacturer of the hardware specifies a temperature T_c as the maximum operating temperature, two limits can be set:

$$\begin{aligned} T_{meas} > T_n + p_w * (T_c - T_n) &\rightarrow \text{Warning alarm} \\ T_{meas} > T_n + p_t * (T_c - T_n) &\rightarrow \text{Critical alarm} \end{aligned} \tag{5-1}$$

where:

T_c: Maximum operating temperature

T_n: Measured temperature in normal operation conditions

T_{meas}: Measured temperature (monitored)

p_w: Warning percentage of the distance between T_n and T_c

p_t: Critical percentage of the distance between T_n and T_c

Similar reasoning can be applied to CPU and RAM memory usage. We can then avoid system crashes and take any necessary actions before the failure of a unit.

5.5.4 DC power supply monitoring

Output cards typically have a voltage range within which they should be operating, which can be taken from their datasheets. When output cards are powered by a DC power supply, this power supply should be monitored using minimum and maximum voltage limits set accordingly to the output card specifications. We can then have a monitoring scheme as follows:

$$V_m < p_l * V_{ll} \rightarrow \text{Undervoltage alarm}$$
$$V_m < p_h * V_{hl} \rightarrow \text{Overvoltage alarm} \quad (5\text{-}2)$$

where:

V_{ll}: Minimum low voltage limit

V_{hl}: Maximum high voltage limit

V_m : Measured voltage (monitored)

p_l: Margin percentage for lower limit (p_l > 100%)

p_h: Margin percentage for higher limit (p_h < 100%)

5.5.5 Controller power supply and battery monitoring

The scheme should also monitor the battery and main power supply of the controller. If the latter fails and the battery is not able to supply enough or reliable power, that is, the battery voltage is below a limit set accordingly to the controller specifications, then the system cannot rely on this unit to continue operation. The battery is monitored in the same way as the low voltage limit of the DC power supply monitoring scheme previously described.

5.5.6 FPGA-FPGA monitoring

The FPGA in one unit can monitor the FPGA in the other unit. The proposed design implements a waveform generator with a few different offset values with specified durations, which is programmed into the FPGA. The waveform can be seen in Fig. 5.7. The FPGA of the first unit sends the waveform to the second unit. The FPGA of the second unit receives the signal and simply sends it back to the first unit. The first unit then checks if the other unit received the same waveform, taking into account the amplitudes and durations in each amplitude value. These signals are sent from one FPGA to the other through the I/O cards to which the FPGAs are connected. It should be noted that other waveforms may be used for this verification too.

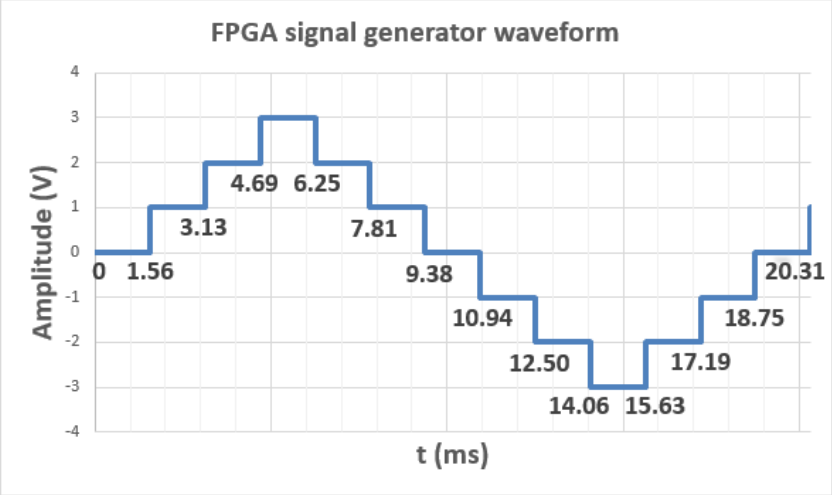

Fig. 5.7: Waveform generated for FPGA-FPGA monitoring.

5.5.7 CPU-FPGA monitoring

The CPU may check if the FPGA in the same controller is responding correctly and has not lost communication with it. The proposed design generates a random number in the CPU and sends it to the FPGA, which in turn sends it back to the CPU. This same action is performed for every processing cycle of the CPU with the constraint that consecutive numbers must be different. Hence, the returned value should be different from the one sent in the previous processing cycle. If two consecutive values are the same, it means that the CPU is not receiving an updated value from the FPGA and got stuck in the previous task, which is recognized as a failure by the CPU-FPGA monitoring scheme. If the value that was received back is not the same but is still different from the last one sent, other failures, such as CPU-FPGA interface issues, are happening. This is also recognized as a failure.

5.5.8 CPU-CPU monitoring

The CPU in one unit may check if the CPU in the other unit is responding correctly and within a time limit. In the proposed design, the CPUs of the units are connected through an Ethernet connection in an IP-addressable network. A ping test using the Internet control message protocol (ICMP) is an established and efficient test to not only serve as a watchdog, that is, check if the other unit is alive in the network, but as a network check [82]. The ping test is performed every second and sends a specified number of packets to the IP address of the other unit. Three parameters are then considered:

- Watchdog: if the host is unreachable → unit not alive;
- Packet loss: if more than 5% of the packets sent are not received back → network unreliable;
- Latency: if latency is above a predetermined limit → network unreliable.

It should be noted that the latency will be usually in the order of a few milliseconds, depending on the network, especially considering that redundant units are usually close to each other, so the predetermined limit can usually be set at a few hundred milliseconds.

If any of these parameters show a problem, the CPU-CPU monitoring scheme will report a failure.

5.5.9 Time-out function

For the FPGA-FPGA, CPU-FPGA and CPU-CPU monitoring schemes, there should always be a time-out function to verify whether the applications are running within acceptable time limits. Obviously, the time-out settings will depend on the specific application and technologies used. It is important to comment here that time-out functions are an important part of any monitoring functions and data acquisition systems. Hence, it is understandable that time-out functions are an important part of any monitoring scheme, including self-monitoring schemes.

5.6 Additional possibilities to improve reliability

There are redundancy schemes and components that could be implemented other than the ones previously described to improve reliability. Obviously, in general, they will result in additional costs. Thus, they will depend on the specifications, budget, and assessed reliability-cost ratio of the companies installing the monitoring system.

5.6.1 DC power supply duplication

Having a backup DC power supply in case the main supply fails is one possibility of increasing the reliability of the monitoring system. There are several possibilities for implementation. One example is, for the DC power supply of the primary controller unit,

we could have the secondary controller-unit monitor the power supply. Should it fail, the secondary controller sends a signal to switch to the backup DC power supply. Another possibility is implementing an automatic switching circuit such as the one shown in Fig. 5.8. This circuit uses a main DC power supply and a backup one. If the main supply loses power, the relay coil loses excitation, automatically switching both the input source to the input of the backup DC power supply and the overall output to the output of the backup supply (i.e., contacts 1 and 2 are usually connected to ‘a’ and are then switched to ‘b’). The resistances in series with the diodes have, for protection purposes, high values compared to the impedance of the output cards to where the DC power supply will be connected.

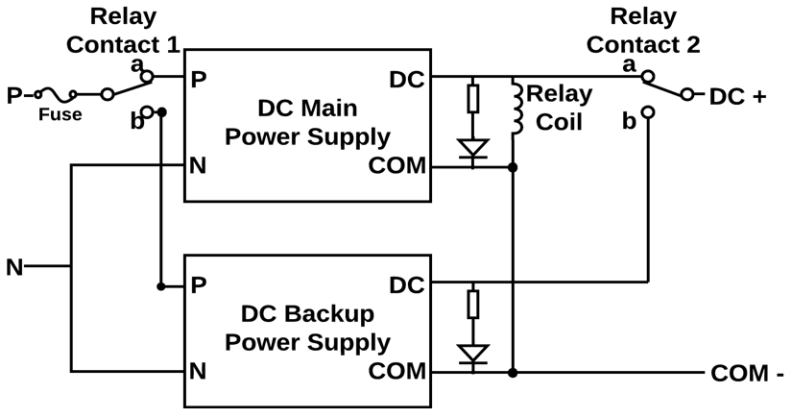

Fig. 5.8: Automatic switching circuit for DC power supply redundancy.

5.6.2 Controller power supply and backup batteries

Using redundant duplicated power supplies for the controller-units is also an alternative. In this case, we would avoid critical conditions that would power off the entire monitoring system. The same reasoning applies to the batteries, even though these batteries are already a backup plan in case the power supply is lost.

5.6.3 Communication channels

Another possibility is the design of redundant communication channels, for example between the controller-units and the NAS. One could either simply duplicate the channel used or use two different communication systems for the redundant channels (e.g., Ethernet cable and serial cable). The benefit of using two different technologies in one redundant scheme is that it removes possible points of common failure.

6 APPLICATION AND CASE STUDY

In the first part of this chapter, the dual modular redundancy scheme presented in chapter “5 - Redundant monitoring system” is validated. Then, a case study using a portion of the Texas synthetic grid (see item 6.2 for the grid information) is presented. This optimized frequency scanning tool is then applied to this case study. Finally, the sub-synchronous resonance detection scheme is implemented within the monitoring system and different filter designs are tested and a comparison of the proposed power spectrum method is made with the matrix pencil method.

6.1 Dual-modular-redundant monitoring system validation

The implemented scheme was tested using a laboratory setup and the architecture showed in Fig. 6.1, with a 120 Vrms wall outlet being used as monitored equipment for the validation part. The laboratory setup is shown in Fig. 6.1. A DC power supply is used to simulate several of the self-monitoring schemes. The DC power supply has a regulated output range of 0-30 V with 0-10 A [83]. The DAQ (Data Acquisition) controllers are used as the monitoring equipment with a sampling frequency of 2000 Hz. In this setup, the CPUs have a 1.91 GHz quad-core processor, 16 GB nonvolatile storage, and 2 GB DDR3 memory [84]. Also, they have an embedded FPGA with 4,000 Kb of maximum Distributed RAM and 16,020 Kb of Block RAM [85]. One GPS antenna [86] per monitoring device is used for synchronization and timestamping purposes. The controllers are then connected to a 4-bay NAS with 2 TB per hard drive [87] through a managed network switch [88].

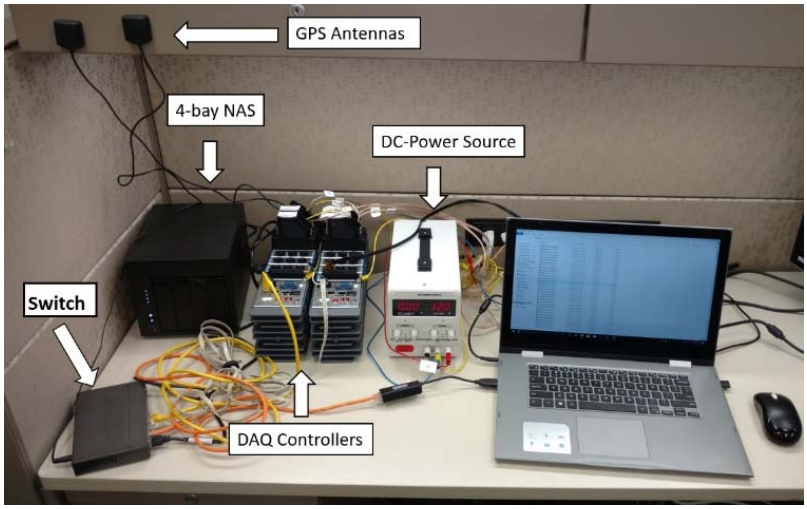

Fig. 6.1: Laboratory setup.

Data integrity was confirmed in the NAS and the CPU-FPGA heterogeneous platform worked efficiently with no jitters. Table 6.1 shows part of the files recorded by the main and backup units. Both files are recording the same signal acquired from the 120 Vrms outlet.

Table 6.1: Voltage measured by the main and backup units.

Timestamp (hh:mm:ss)	Main Unit Voltage (V)	Timestamp (hh:mm:ss)	Backup Unit Voltage (V)
12:35:23.313149	-100.13	12:35:23.313360	-108.23
12:35:23.313649	-119.22	12:35:23.313860	-129.06
12:35:23.314149	-144.25	12:35:23.314359	-152.00
12:35:23.314650	-156.83	12:35:23.314860	-157.41
12:35:23.315150	-158.05	12:35:23.315359	-159.13
12:35:23.315650	-160.99	12:35:23.315859	-162.00
12:35:23.316149	-162.51	12:35:23.316360	-161.52
12:35:23.316649	-157.37	12:35:23.316860	153.10

Although the monitoring equipment and input cards are of the same model for the main and backup units, obviously they cannot be exactly the same. Added to the fact that data acquisition does not start at exactly the same instant, we can expect a slight difference in the time of the sampled points. In this case, the sampled points between both units differ by approximately 210 microseconds. However, we can verify synchronization by calculating the phasor of the voltage signal for each unit in relation to a common time reference. This is the same concept applied in phasor measurement units (PMU) [89]. Calculating the phasors using one second of data we get:

$$V_{main} = 167.02\sin(2\pi 60t + 206.11°)$$
$$V_{backup} = 167.02\sin(2\pi 60t + 206.10°)$$

From the results, we can see that both units depict the same signal, resulting in the exact same amplitude and only 0.01° of phase difference. We can then conclude that synchronization was achieved.

In order to test the behavior of the redundant mechanism regarding controller temperatures, CPU usage, and RAM usage, the actual objects of these variables in the algorithm were replaced by an input and connected to a DC power supply where we can control the values, which were then multiplied by a constant value each so as to reach the order of magnitude of such variables. The same method was applied to simulate an under-voltage of the batteries.

The failures of both the DC power supply and the controller's main power supply were executed by simply turning them off. A failure was simulated for the FPGA-FPGA scheme by disconnecting the cables between the I/O ports of both controllers for this scheme. To test the CPU-FPGA scheme, an artificial variable forced the algorithm to receive identical values in two consecutive processing cycles, which is understood as the value not having been updated. For the CPU-CPU scheme, an Ethernet failure was carried out by disconnecting the cable between both CPUs. The time-out functions were tested in all schemes by forcing the algorithms to time out. This can be done by setting the time-out limits to zero.

The following equations show an example of how the test was carried out for the temperature monitoring scheme, applying equation (5-1):

$T_{meas} > 40 + 50\% * (55 - 40) = 47.5$ → Warning alarm
$T_{meas} > 40 + 80\% * (55 - 40) = 52$ → Critical alarm

T_{meas} was simulated using the DC power supply. Because the power supply has a voltage limit of 30 V, a multiplier constant of 2 was implemented in software to reach the desired values. A value of 53 for T_{meas} in the main unit made its health value drop by 10%, as shown in Fig. 6.2.

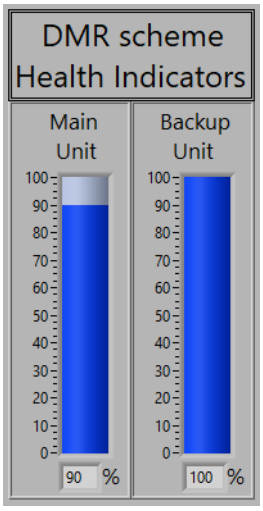

Fig. 6.2: Health indicators when the main unit has one failure in one scheme.

Fig. 6.3 and Fig. 6.4 depict the results after each experiment for failures in the main unit. As we can see, Fig. 6.3 shows a time period in which both the main and backup units are working normally. The active unit then shows a copy of what the main unit shows, as it should.

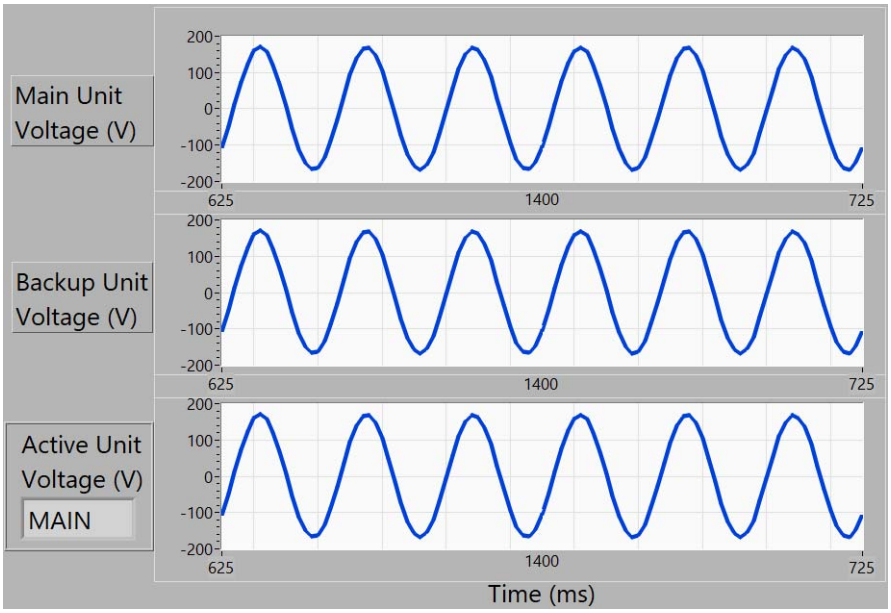

Fig. 6.3: Voltage acquired by the main and backup units – both operating normally. The active unit waveform is identical to the main unit waveform.

In Fig. 6.4, the main unit fails at almost 1400 ms of the experiment. The health value calculated by the DMR scheme for the main unit is lower than for the backup unit,

as shown in Fig. 6.2. Therefore, the active unit shows a copy of what the backup unit shows, as it should.

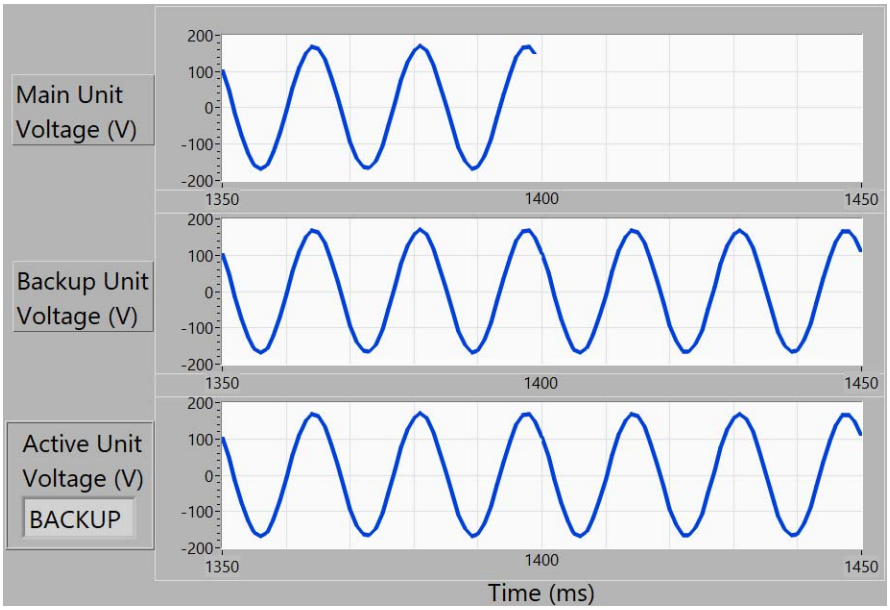

Fig. 6.4: Voltage acquired by the main and backup units – failure in the main unit. The active unit waveform is identical to the backup unit waveform.

These results can be understood as presenting no data loss, which is the goal of a redundant scheme such as a dual modular redundancy scheme.

Finally, data redundancy was obtained by means of a NAS with four disks. In the RAID 10 configuration, despite the fact that there is data mirroring, we do not visualize duplicate data. After randomly removing one of the hard disks, the exact same data (same folders/files stored) could be observed, meaning no data loss happened.

6.2 Case study: modified Texas synthetic grid

The frequency scanning tool and the detection system were applied to a portion of a modified Texas synthetic grid, as depicted in Fig. 6.5, and all the time analyses were performed for both the risk assessment analysis and the real-time application. The original model was developed by Texas A&M University and is not an actual depiction of the Texas grid, but is based on public data to synthetically represent the network [50]. It allows researchers to test their algorithms on large-scale cases. In order to create the SSR condition, a series capacitor with a compensation level of 70% was added on the line

between the Miami and Denton stations. Also, three nonlinear elements were added to the case as follows:

- 210 MW Wind Farm 1: this wind farm involves 140×1.5 MW type-3 turbines which are connected to the Miami 1 161 kV station (POI);
- 100 MVA voltage source converter (VSC)-based STATCOM connected to the Miami 1 161 kV station;
- 90 MW Wind Farm 2: this wind farm involves 25×3.6 MW type-3 turbines which are connected to the Panhandle 3 (PH3) 161 kV station.

The remaining grid data can be found in Appendix B.

In this case study, the objective is to perform a frequency-scan-based screening for Wind Farm 1 to evaluate the SSR risk (in this case, SSCI) of this specific wind farm while the system involves two other active elements (Wind Farm 2 and STATCOM). As a first step, a contingency was defined to create a radial connection between Wind Farm 1 and the series-compensated line. The radial contingency is an N-3 contingency and involves tripping/opening of three transmission lines as below:

- 161 kV line between the PH2 1 and PH6 stations;
- 500 kV line between the PH4 and Ralls 1 stations;
- 500 kV line between the Miami and Wichita Falls stations.

The contingency is depicted with black dashed lines in Fig. 6.5. If these lines are tripped/opened, the only path to export power from the Panhandle area (within the blue oval shape), which also includes the wind farms, is through the series-compensated line between the Miami and Denton stations.

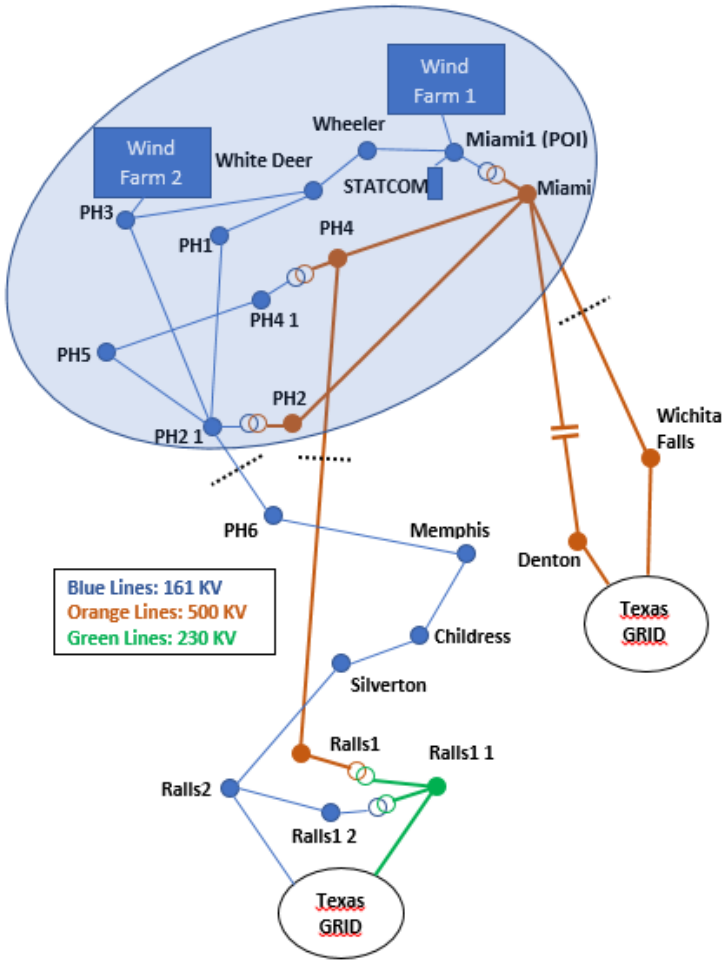

Fig. 6.5: Portion of the modified Texas synthetic grid (grid data in Appendix B).

6.3 Optimized frequency scanning

The screening process for Wind Farm 1 at the 161 kV Miami station (POI) is performed as per the following steps:

1. Perform an independent frequency scan on Wind Farm 1 from the POI;
2. Perform an independent frequency scan on the VSC-based STATCOM from the POI;
3. Calculate the equivalent sub-synchronous impedance (resistance and reactance) of Wind Farm 1 and the VSC-based STATCOM based on their parallel connection at the POI. Hereafter, this impedance is called plant-side impedance (grid side 1);
4. Perform a frequency scan on the network side that involves Wind Farm 2 and the rest of the grid under the predefined N-3 contingency. Hereafter, this impedance is called network-side impedance (grid side 2);

5. Calculate the cumulative impedances based on the plant-side and network-side impedances as per equations (3-3) and (3-4);
6. If the cumulative resistance at the crossover frequency (zero reactance frequency) is negative or zero (equations (3-5) and (3-6)), there is a potential risk of SSCI.

Note that the steps above perform independent frequency scans on Wind Farm 1 and on the STATCOM despite their point of common connection (at the POI). This requirement reduces the error, as the influence of the voltage injections in one element will not affect the response of the other.

6.3.1 Frequency scan results

The multisine harmonic signal angles were generated as described in section "3.3.1 - Generating the multisine signal for the frequency scan", with the difference that the amplitude for each sine wave is now 161 V (0.1% of the POI rated voltage of 161 kV). The cumulative resistance and reactance for all methods can be found in Fig. 6.6 and the errors in Fig. 6.7.

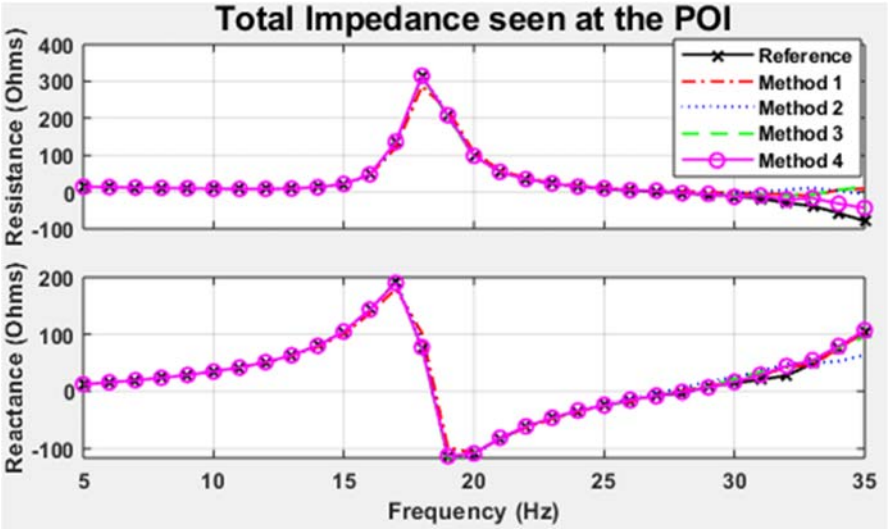

Fig. 6.6: Total resistance and reactance seen at the POI.

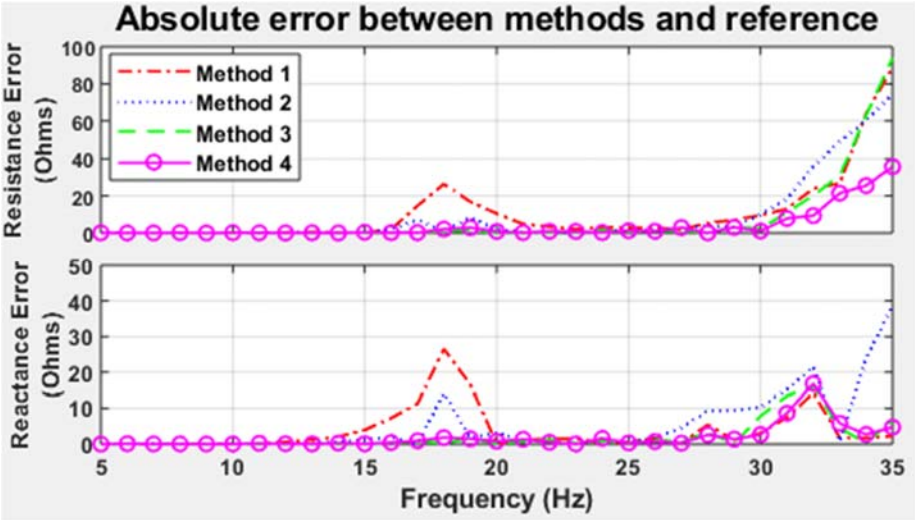

Fig. 6.7: Error of each method in relation to the reference.

In this case study, several nonlinear components are present on both sides of the frequency scan. The plant side contains not only a wind farm but also a VSC-based STATCOM. As can be observed in Fig. 6.6, the presence of a second wind farm on the network side adds a high-impedance transition from an inductive response to a capacitive response seen at the POI. Fig. 6.7 shows that, during this transition between 15 Hz and 20 Hz, the error in the frequency scan may increase. However, the optimized method (method 4) is still able to maintain very low error values. Table 6.2 and Table 6.3 show the average total errors seen at the POI for the resistance and reactance, respectively, and confirm the better performance of the optimized method in a test case with a larger grid with more nonlinear components in both sides of the scan.

Table 6.2: Total resistance error of methods in relation to the reference.

Method #	Equation for angle δ_k	Average Total Error (Ω)
1	$\delta_k = 0$	10.652
2	$\delta_k = {f_k}^2$	9.211
3	$\delta_k = Schroeder$ (equation (3-15))	7.554
4	$\delta_k = Optimized$	3.807

Table 6.3: Total reactance error of methods in relation to the reference.

Method #	Equation for angle δ_k	Average Total Error (Ω)
1	$\delta_k = 0$	3.657
2	$\delta_k = {f_k}^2$	5.272
3	$\delta_k = Schroeder$ (equation (3-15))	1.959
4	$\delta_k = Optimized$	1.813

Fig. 6.8 shows the zoomed-in plot of the total impedance around the crossover frequency (zoomed-in plot of Fig. 6.6 around the crossover frequency). Table 6.4 shows the frequency of oscillation and resistance results for all methods.

Table 6.4: Frequency of oscillation and resistance values.

Method #	Frequency of Oscillation (Hz)	Resistance (Ω)
1	27.85	2.45
2	27.36	2.42
3	28.09	-3.23
4	28.18	-3.24
Reference	28.34	-4.55

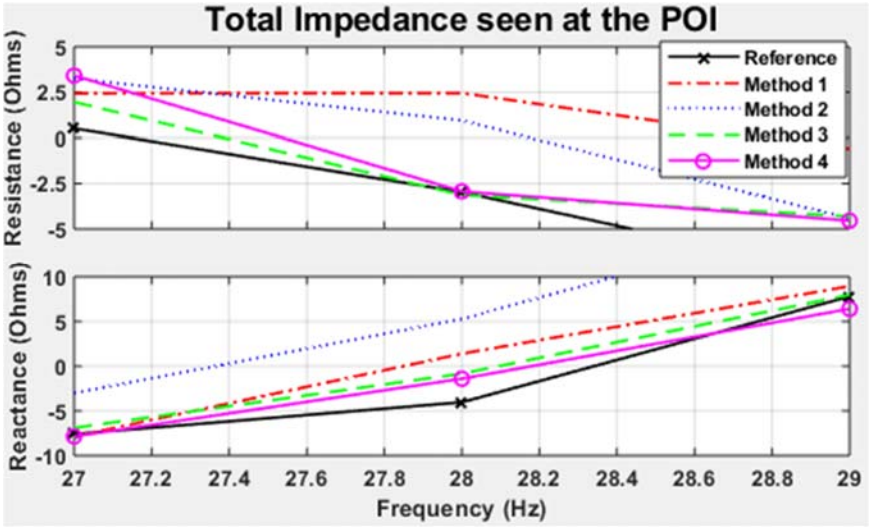

Fig. 6.8: Zoomed-in plot of Fig. 6.6 around the crossover frequency.

Very important observations can be made from the results. Firstly, the optimized method has the closest results to the reference for both the frequency of oscillation and the resistance value at the respective frequency. Secondly, methods 1 and 2 resulted not only in frequencies of oscillation farther from the reference but in positive values of the resistance. This shows that poor choices for the angles of the multisine signals injected can even lead to completely inaccurate conclusions. In this case, methods 1 and 2 show that the oscillations would be damped; while methods 3, 4 and the reference show that the oscillations would be undamped. To further verify the frequency scan results, a time-domain transient simulation needs to be performed, as is usually mandated by protocols for SSR risk assessment, such as the ERCOT nodal protocols [25].

It should be noted that the grid might contain different nonlinear elements and, as a result, different nonlinear characteristics. Besides, the voltage levels on each device might differ depending on their location in the grid. One specific signal might maintain the approximate linearity around the initial steady-state condition of one device while pushing another device's response to the nonlinear boundaries. This means that the small-signal analysis is maintained for the former, but will still result in some error for the latter. Therefore, there is no ideal choice of amplitude and angles for the multisine signal that will not yield errors to some extent. The choice of 0.1% amplitude level of the rated voltage used herein has shown to be a good choice for most cases. The main goal is to reduce the average total error for both the resistance and reactance values so as to keep the best possible impedance estimation throughout the entire range of frequencies.

6.3.2 Time-domain transient simulation

A time-domain transient simulation with the application of a three-phase fault that will lead to the predefined N-3 contingency was performed per the following sequence:

- The simulation starts with lines PH4-RALLS1 and MIAMI-WICHITA FALLS out of service, for instance, for maintenance purposes;
- The simulation is run until t=19.95 seconds to ensure that steady-state is achieved;
- At t=19.95 seconds, a three-phase fault is applied to line PH2 1-PH6;
- At t=20 seconds, a circuit breaker opens line PH2 1-PH6.

The three-phase active power and instantaneous voltages and currents at the POI are depicted in Fig. 6.9. An FFT analysis is performed on the current signal after the oscillation starts. As shown in Fig. 6.11, the SSCI signal has a frequency of 29.34 Hz. Fig. 6.10 shows the frequency in the power signal as 30.66 Hz, as expected, which is complementary to the fundamental frequency (60 – 30.66 = 29.34 Hz). Again, the reference and optimized method provide the closest results to the time-domain simulation results.

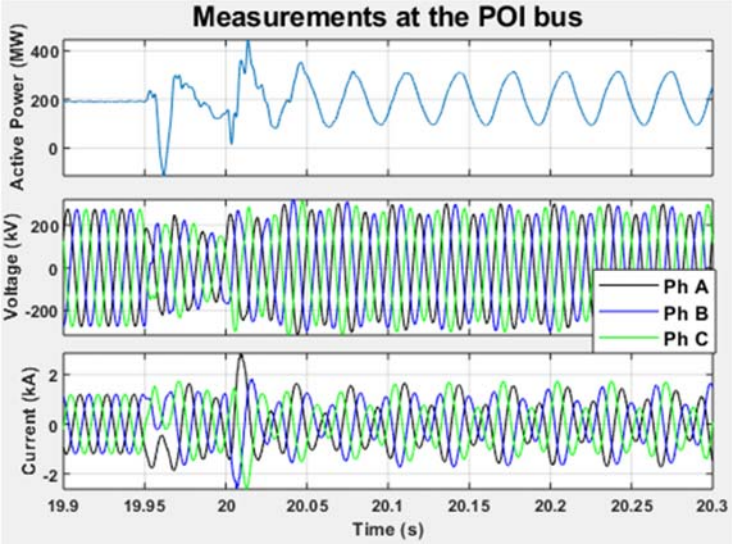

Fig. 6.9: Time-domain simulation results at the POI. Active power on the top. Voltage in the middle. Current on the bottom.

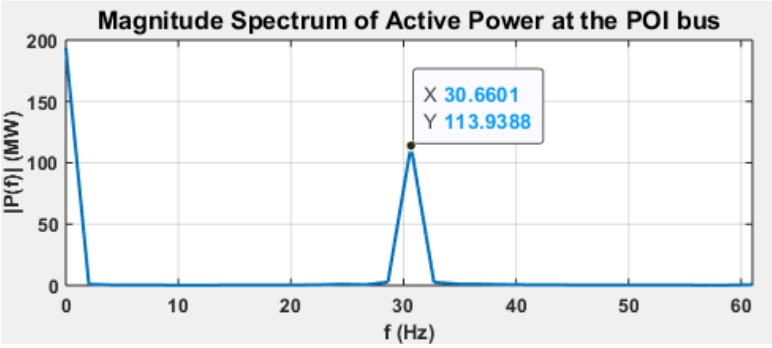

Fig. 6.10: Amplitude of the FFT spectrum of the power signal.

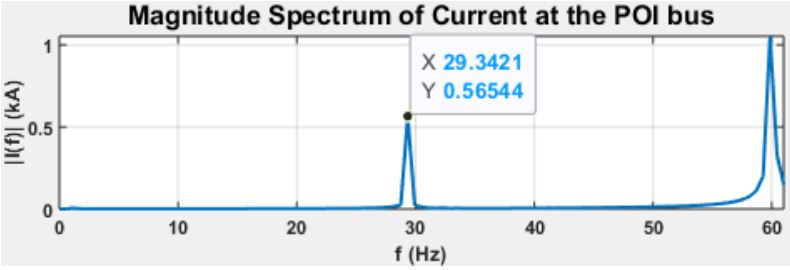

Fig. 6.11: Amplitude of the FFT spectrum of the current signal.

6.3.3 Frequency scanning simulation time

When we inject a signal on top of a steady-state operation point of a system, a transient period precedes the new steady-state. The impedance estimation can only be calculated after this transient period ends in order to achieve an accurate estimation through the harmonic injection technique. The three-phase active power output of the grid

at the POI is a good index to evaluate the new steady-state condition. The system is considered to settle to a steady state if the envelope of the active power reaches and remains within a certain percentage range of its final value (normally 2% or 5%) [48]. This settling time can be utilized to calculate the minimum simulation time.

Using equations (3-16) and (3-17), we can compare the minimum simulation times between multiple single-frequency injections and the proposed multisine injection. Fig. 6.12 shows the normalized transient response of the network-side active power after injecting a single sine wave of 30 Hz. The magnitude is normalized to set the final value of the upper envelope to 1 (by dividing all values by its final value). A $\pm$5% range from the final value is used as the settling limits. We can see that the settling time for 30 Hz is 0.197 s. The settling time results of all frequencies are shown in Table 6.5:

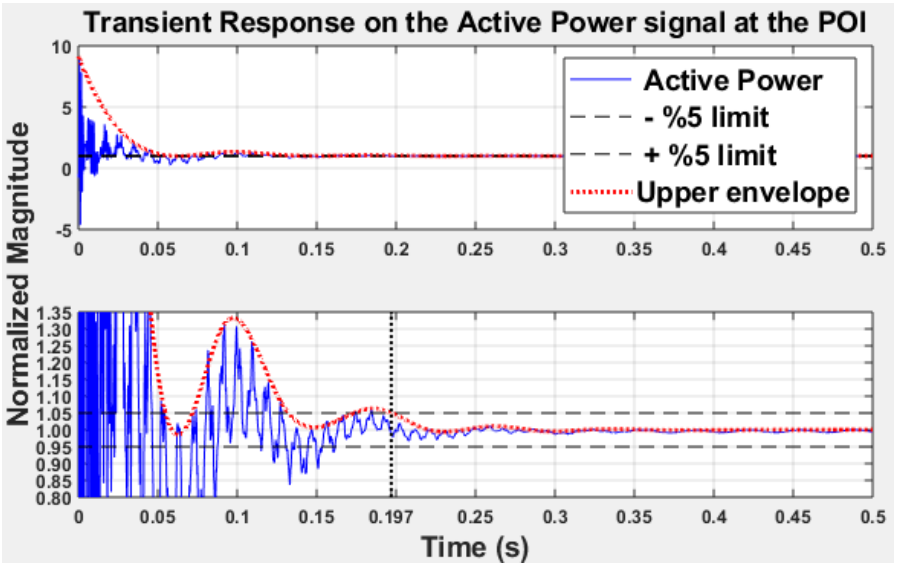

Fig. 6.12: Normalized transient response for an injection of a single sine wave of 30 Hz. Bottom plot is a zoomed-in version of the top plot.

Table 6.5: Settling times for each injected frequency.

$f_k(Hz)$	$Tst(s)$	$f_k(Hz)$	$Tst(s)$	$f_k(Hz)$	$Tst(s)$	$f_k(Hz)$	$Tst(s)$
5	0.186	13	0.184	21	0.194	29	0.193
6	0.188	14	0.193	22	0.194	30	0.197
7	0.187	15	0.192	23	0.192	31	0.201
8	0.178	16	0.194	24	0.195	32	0.188
9	0.192	17	0.19	25	0.194	33	0.194
10	0.192	18	0.192	26	0.193	34	0.2
11	0.191	19	0.195	27	0.191	35	0.203
12	0.184	20	0.194	28	0.186	-	-

From the values of Table 6.5, equations (3-16) and (3-17) give the minimum simulation time for multiple single-frequency injections and for one multisine injection with period $T_0 = 1\ s$:

$$T_{sf} = \sum_{k=5}^{35} \left\{ \frac{1}{f_k} + Tst_k \} \right\} = 8.010\ s$$

$$T_{ms} = T_0 + \max\{Tst_k\} = 1 + 0.203 = 1.203\ s$$

We can see that performing multiple single-frequency injections takes at least 6.66 times longer than one multisine injection. This is the minimum ratio considering the minimum settling times for each single-frequency injection. In industrial practice, when performing frequency scanning studies, because we do not know the exact settling times for each frequency in every grid to be scanned, we need to assume a fixed Tst with a certain margin to ensure that the transient response has settled. For instance, using fixed $Tst = 0.5\ s$ in the above case study for all frequencies, the settling times are:

$$T_{sf} = \sum_{k=5}^{35} \left\{ \frac{1}{f_k} + 0.5 \right\} = 17.563\ s$$

$$T_{ms} = T_0 + 0.5 = 1 + 0.5 = 1.500\ s$$

In this case, the proposed method is 11.71 times faster.

The simulations were run in a computer with a processor Intel Core i7-7700 @ 3.60 GHz with 8 GB of RAM memory. This computer took approximately 47.5 real-world seconds to run 1 simulation-second using time steps of 5 μs for this case study. This means that the results of T_{sf} and T_{ms} take in reality 47.5 times the simulation time. When performing frequency scanning studies for SSR risk assessment, a high number of contingencies are considered. ERCOT, for example, establishes a contingency criteria of up to N-14 [25]. It is possible to see that the real-world time to simulate a large number of cases can be extremely high. Thus, the proposed method can greatly reduce it while maintaining good accuracy.

6.4 Sub-synchronous resonance detection system

All filter designs will consider an acquisition system with a sampling rate of f_{sr} = 1000 Hz. It is assumed that the acquisition system contains an analog lowpass filter with a cutoff frequency of $f_{Ny.frequency}$ to avoid aliasing. In order to maintain the processing sampling rate between the desired 300 Hz and 600 Hz range while reducing the computational cost, a decimation factor of $D = 3$ is used. The sampling-related parameters are as follows:

Table 6.6: Sampling-related parameters

f_{sr} (Hz)	$f_{Ny.frequency} = \frac{f_{sr}}{2}$ (Hz)	Decimation factor: D	$f_{sr,down} = \frac{f_{sr}}{D}$ (Hz)	$f_{Ny,down} = \frac{f_{sr,down}}{2}$ (Hz)
1000	500	3	333	167

Using a sub-synchronous bandpass range $[f_{SSO,low}, f_{SSO,high}] = [5\text{ Hz}, 55\text{ Hz}]$, the active power signal will contain the complementary frequency relative to the fundamental (see Appendix C for detailed information), that is:

- $f_{SSO,low} = 5\ Hz \rightarrow f_{SSO,filter,high} = 60 - 5 = 55\ Hz$
- $f_{SSO,high} = 55\ Hz \rightarrow f_{SSO,filter,low} = 60 - 55 = 5\ Hz$

Hence, the filter bandpass range for the active power signal is:

$$[f_{SSO,filter,low}, f_{SSO,filter,high}] = [5\text{ Hz}, 55\text{ Hz}]$$

The digital lowpass filter must have a maximum cutoff frequency $f_{SSO,filter,high}$ lower than $f_{Ny,down} = 167$ Hz, so this setting is feasible. The selected range will remove any possible unwanted components above the frequency range of interest, such as noise, and remove the steady-state DC component of the active power signal.

IIR filters will be used, as they can obtain similar responses to FIR filters using a lower-order filter, which is desirable for time-critical applications. Herein, we will use MATLAB Filter Designer Toolbox to get the first design and then customize it to get the desired response.

The designs in this item will consider the active power as the input signal, which also facilitates visualization of the sub-synchronous oscillations on waveform plots. The DC component is the main one in the active power, so a higher attenuation level needs to be set for this component. Taking X_n as the maximum steady-state value taken at system configurations prone to SSCI at the point of measurement, we have X_n = 192 MW (same steady-state value of the top plot of Fig. 6.9). Using equation (4-24), a pickup threshold value for the protection system of 4 MW and Mg = 50%, we have:

$$Gain_{dB}(f) = 20\ log_{10}\left(\frac{X_{pickup} * Mg}{X_n}\right) = 20\ log_{10}\left(\frac{4 * 0.5}{192}\right) = -39.65\ dB$$

Therefore, an attenuation level of 39.65 dB needs to be set for the DC component. A certain frequency margin should still be considered. Herein, this attenuation will be minimum for frequencies from 0 Hz to 0.3 Hz, in which 0.3 Hz is also referred to as the stopband corner frequency. The transition band is therefore between the stopband corner frequency and $f_{SSO,filter,low}$, that is, between 0.3 Hz and 5 Hz.

6.4.1 Filter design 1: standard bandpass Butterworth filter

A standard procedure will be considered using a low and a high cutoff frequency to delimitate the passband, as shown in Table 6.7. The order of the filter was set to be minimized.

Table 6.7: Butterworth bandpass filter parameters.

Type	Butterworth
Order	Minimized = 4
Low cutoff frequency (Hz)	5
High cutoff frequency (Hz)	55

The resulting filter is a fourth-order filter with the zeros/poles locations and frequency response as shown in Fig. 6.13 and Fig. 6.14, respectively.

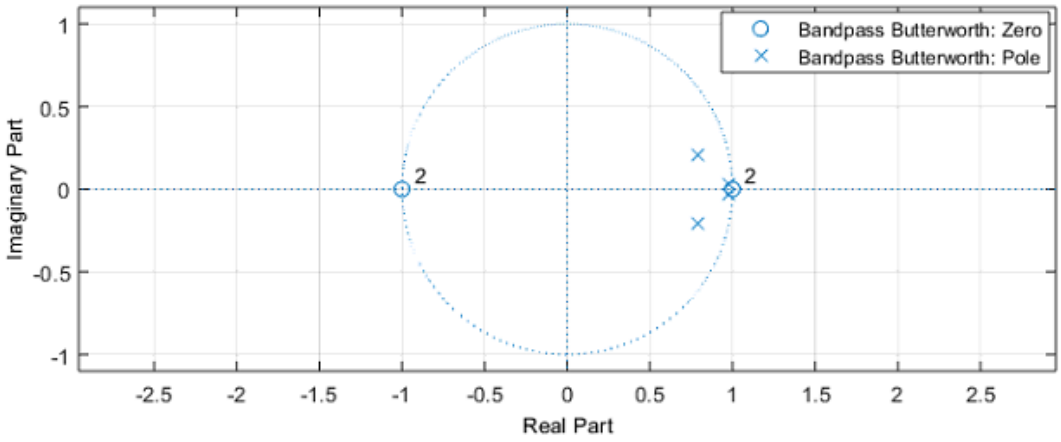

Fig. 6.13: Butterworth bandpass filter → poles/zeros location.

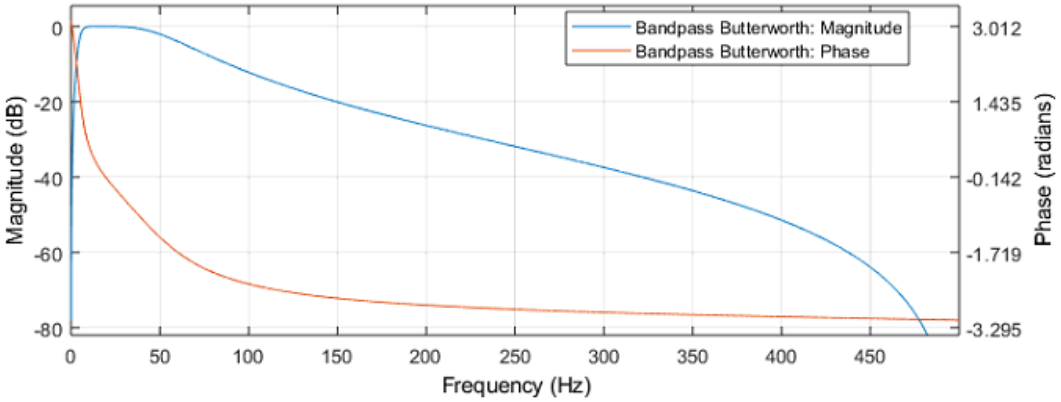

Fig. 6.14: Butterworth bandpass filter → frequency response.

Fig. 6.15 is the zoomed-in frequency response until 70 Hz.

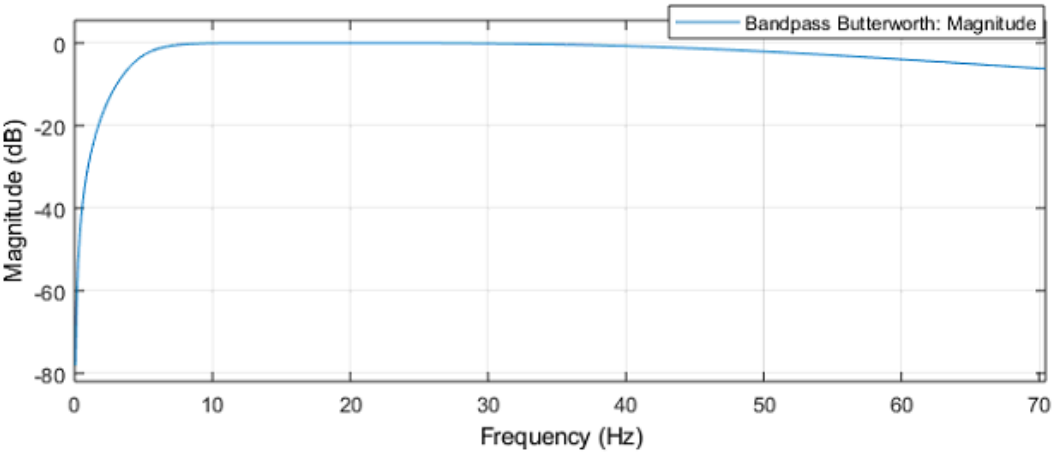

Fig. 6.15: Butterworth bandpass filter → zoomed-in frequency response until 70 Hz.

We then get the following transfer function:

$$\frac{0.02008\,z\text{^}4\ -\ 0.04017\,z\text{^}2\ +\ 0.02008}{\text{z\^{}4}\ -\ 3.542\,\text{z\^{}3}\ +\ 4.728\,\text{z\^{}2}\ -\ 2.828\,\text{z}\ +\ 0.6414}$$

The zeros and poles are at

$$z_1 = -1$$
$$z_2 = -1$$
$$z_3 = 1$$
$$z_4 = 1$$
$$p_1 = 0.978520\ +\ 0.025831i$$
$$p_2 = 0.978520 -\ 0.025831i$$
$$p_3 = 0.792253\ +\ 0.204175i$$
$$p_4 = 0.792253 - 0.204175i$$

6.4.2 Filter design 2: standard bandpass Chebyshev Type II filter

This design will use an Inverse Chebyshev (type II) filter to provide a steeper roll-off between the stopbands and the passband. This type of filter allows for ripples in the stopband but attempts to maintain a flat response in the passband. The first stopband is between 0 Hz and the first stopband corner frequency at 0.3 Hz, which requires an attenuation level of 39.65 dB. Then, there is an ascending transition range between 0.3 Hz and the first cutoff frequency at 5 Hz. The passband starts at 5 Hz and ends at the second cutoff frequency at 55 Hz. A descending transition band between 55 Hz and the last stopband corner frequency at 500 Hz (maximum resolvable frequency for a sampling rate of f_{sr} = 1000 Hz) ensures a smooth attenuation at high frequencies, which reduces the requirement on the filter order as these frequencies do not need high attenuation when using the active power as input. Table 6.8 sums up all filter parameters. The order of the filter was set to be minimized.

Table 6.8: Inverse Chebyshev bandpass filter parameters.

Type	Chebyshev Type II
Order	Minimized = 4
First stopband corner frequency (Hz)	0.3
Attenuation at first stopband corner (dB)	39.65
First cutoff frequency (Hz)	5
Second cutoff frequency (Hz)	55
Second stopband corner frequency (Hz)	500
Attenuation at second stopband corner (dB)	20

The resulting filter is a fourth-order filter with the zeros/poles locations and frequency response as shown in Fig. 6.16 and Fig. 6.17, respectively.

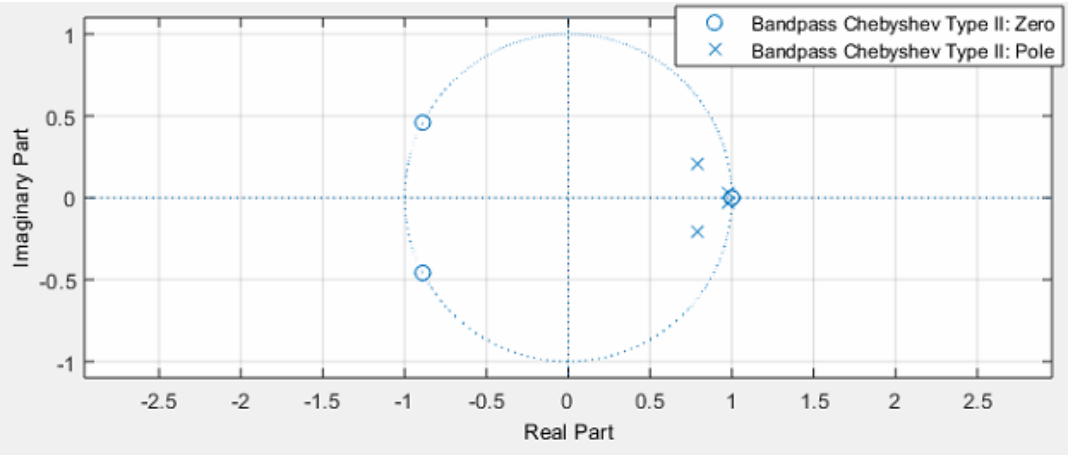

Fig. 6.16: Inverse Chebyshev bandpass filter → poles/zeros location.

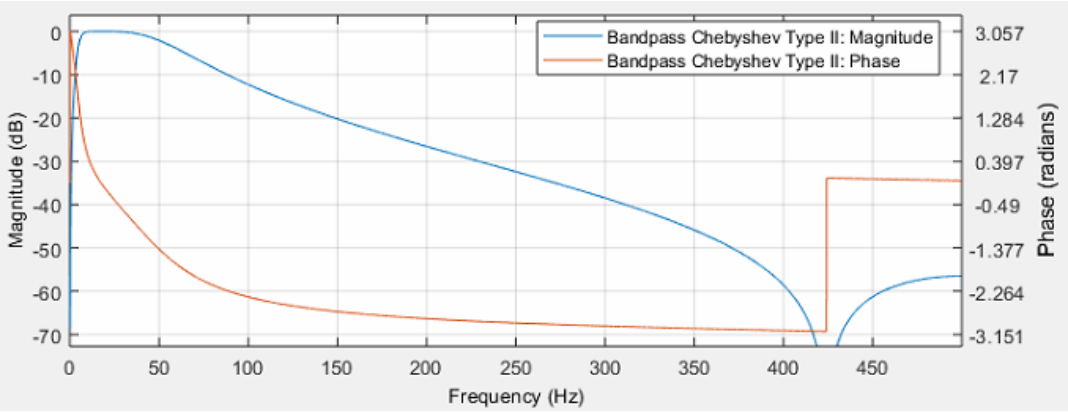

Fig. 6.17: Inverse Chebyshev bandpass filter → frequency response.

Fig. 6.18 is the zoomed-in frequency response until 70 Hz. Fig. 6.19 is the zoomed-in frequency response until 10 Hz. We can see a smooth decay for higher frequencies and ripples at frequencies above around 400 Hz and below around 0.5 Hz, which allow for steeper roll-offs and a flatter response in the passband.

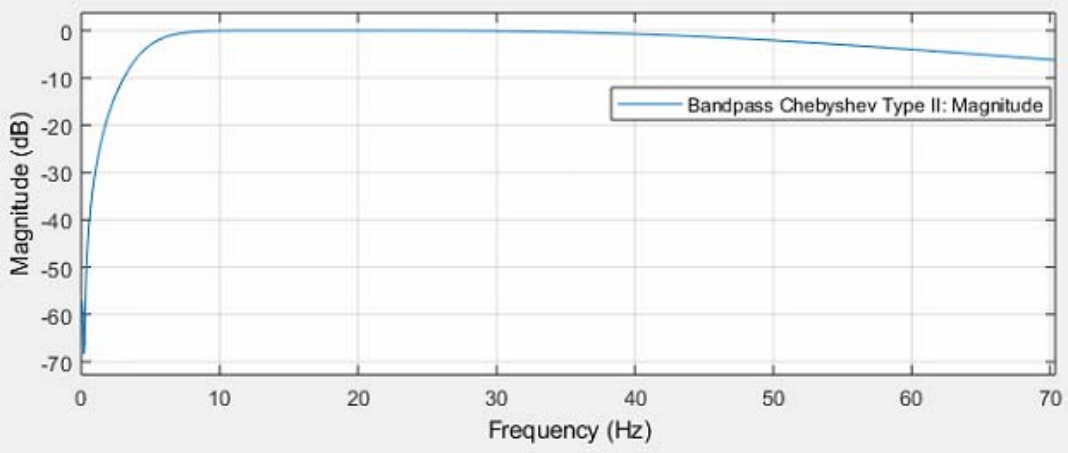

Fig. 6.18: Inverse Chebyshev bandpass filter → zoomed-in frequency response until 70 Hz.

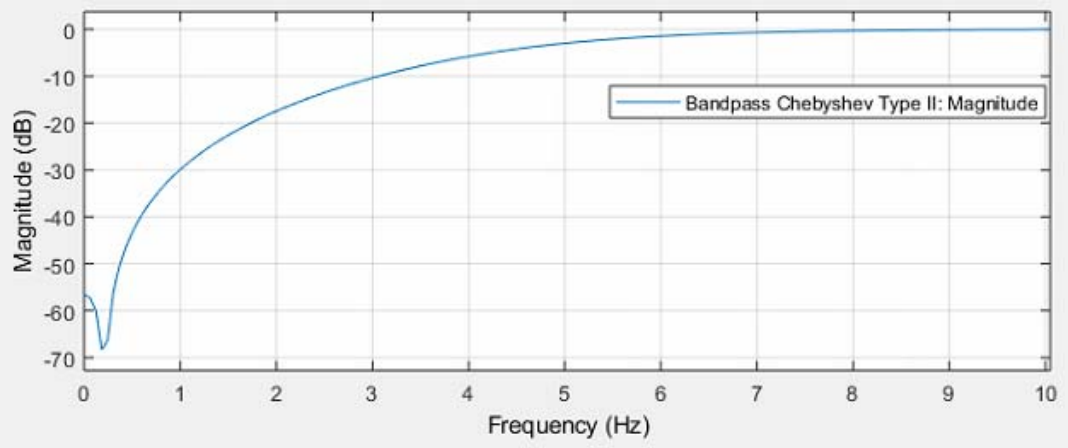

Fig. 6.19: Inverse Chebyshev bandpass filter → zoomed-in frequency response until 10 Hz.

We then get the following transfer function is:

$$\frac{0.02135\,z\text{^}4\ -\ 0.004766\,z\text{^}3\ -\ 0.03317\,z\text{^}2\ -\ 0.004766\,z\ +\ 0.02135}{\text{z\^{}4}\ -\ 3.541\,\text{z\^{}3}\ +\ 4.727\,\text{z\^{}2}\ -\ 2.827\,\text{z}\ +\ 0.641}$$

The zeros and poles are at

$$z_1 = -0.888390 + 0.459090i$$
$$z_2 = -0.888390 - 0.459090i$$
$$z_3 = 0.999999 + 0.001333i$$
$$z_4 = 0.999999 - 0.001333i$$
$$p_1 = 0.978570 + 0.025789i$$
$$p_2 = 0.978570 - 0.025789i$$
$$p_3 = 0.791900 + 0.204559i$$
$$p_4 = 0.791900 - 0.204559i$$

6.4.3 Filter design 3: customized filter

First, for the design of the lowpass section of the filter, we will use the following parameters.

Table 6.9: Lowpass section: initial design parameters.

Type	Butterworth
Order	1
Cutoff frequency (Hz)	55

The zeros/poles locations in the z-plane are shown in Fig. 6.20 and the frequency response is shown in Fig. 6.21.

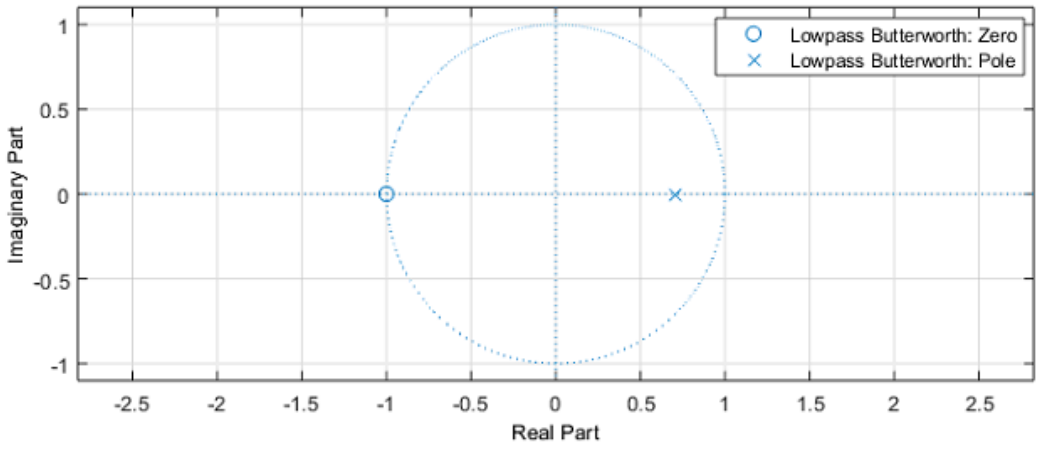

Fig. 6.20: Customized filter lowpass section: initial design → poles/zeros location.

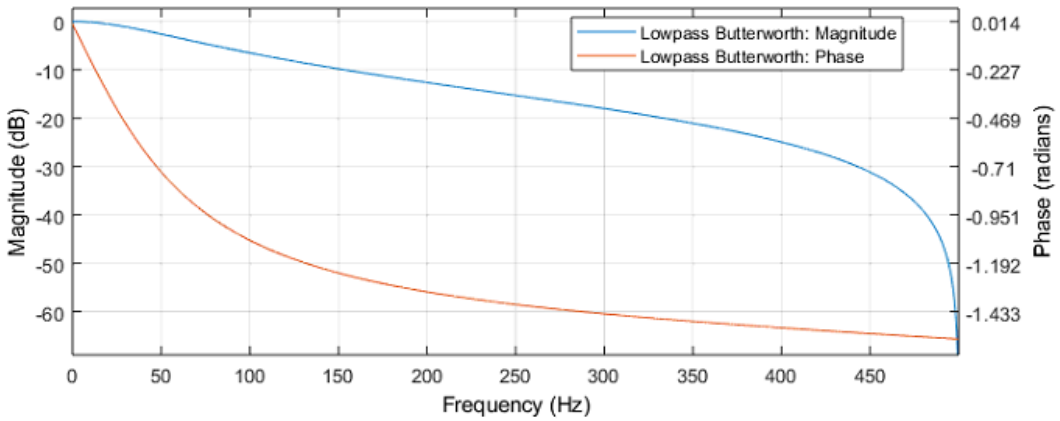

Fig. 6.21: Customized filter lowpass section: initial design → frequency response.

The transfer function of the initial design is:

$$\frac{0.1486\,z\text{^}2\ +\ 0.1486\,z}{\text{z\^{}2}\ -\ 0.7028\,\text{z}}$$

The zeros and poles are at

$$z_1 = 0$$
$$z_2 = -1$$
$$p_1 = 0$$
$$p_2 = 0.7028$$

By the location of the poles and zeros, we can see that the system is stable (all poles inside the unit circle) and marginally minimum-delay (zeros also inside the unit circle). Because the zero $z_1 = 0$ cancels the influence of the pole $p_1 = 0$, the order of the filter is 1, which provides a very fast response. Fig. 6.22 is the zoomed-in frequency response until 70 Hz.

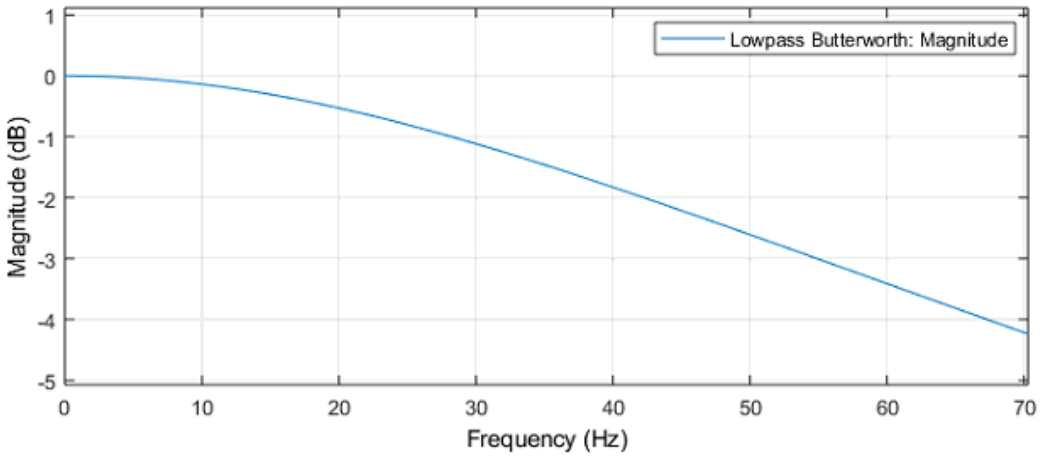

Fig. 6.22: Customized filter lowpass section: initial design → zoomed-in frequency response until 70 Hz.

If we want the response to remain flat until a frequency close to 55 Hz, we need to increase the influence of the pole toward -1, which is also the location of the zero. Pulling the pole $p_2 = 0.7028$ to the locus at $p_2 = 0.3239$, we have the zeros/poles loci shown in Fig. 6.23 and the frequency response of Fig. 6.24. Fig. 6.25 is the new zoomed-in frequency response until 70 Hz. We can see that the magnitude decays slower and the order of the filter is maintained at 1. The lowpass filter does not need to have a steep roll-off when the active power is the input signal.

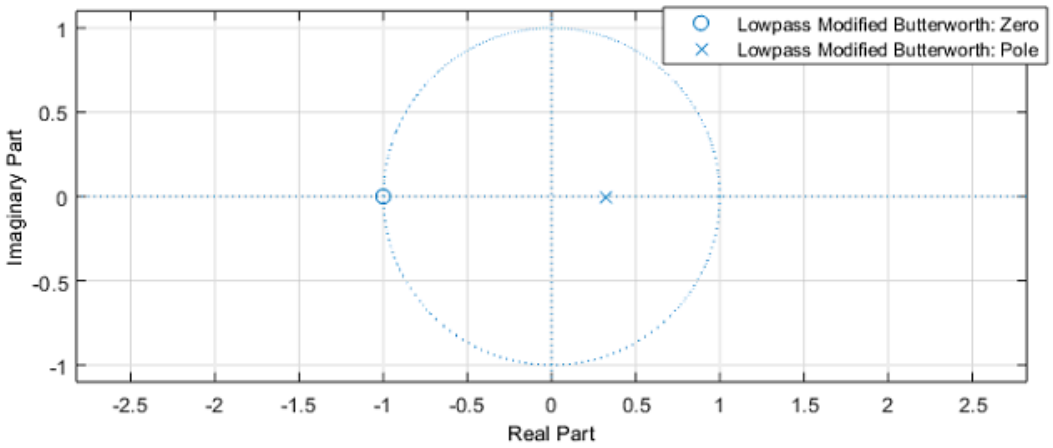

Fig. 6.23: Customized filter lowpass section: modified design → poles/zeros location.

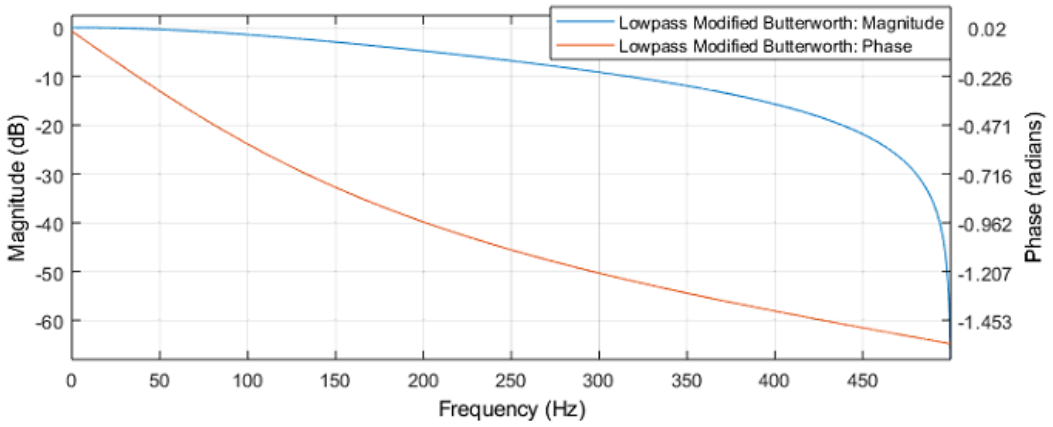

Fig. 6.24: Customized filter lowpass section: modified design → frequency response.

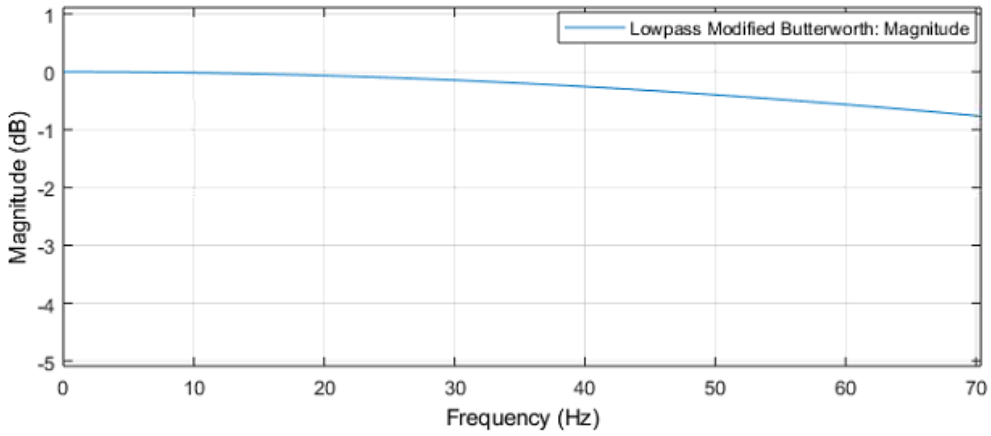

Fig. 6.25: Customized filter lowpass section: modified design → zoomed-in frequency response until 70 Hz.

The transfer function of the modified lowpass filter design is:

$$\frac{0.3381\ z\text{^}2\ +\ 0.3381\ z}{\text{z\^{}2}\ -\ 0.3239\ \text{z}}$$

For the design of the highpass section of the filter, a much higher steepness is necessary, as the DC component in the active power signal is at a high level and needs to be removed with an attenuation level of 39.65 dB at the same time that the passband already starts at 5 Hz. Due to the fast necessary roll-off, an Inverse Chebyshev (type II) filter will be used, which allows for ripples in the stopband but attempts to maintain a flat response in the passband. Table 6.10 shows the parameters of the initial design of the highpass filter, in which a 39.65 dB attenuation was set at the stopband corner frequency at 0.3 Hz. The transition band is between 0.3 Hz and 5 Hz. Additionally, this design was

set to minimize the response error in the passband using a desired optimal value of 0 dB throughout the whole passband - including the passband corner - so as to get the flattest possible response in the passband.

Table 6.10: Highpass section: optimized design parameters.

Type	Chebyshev Type II
Order	2
Stopband corner frequency (Hz)	0.3
Attenuation at stopband corner (dB)	39.65
Passband corner frequency (Hz)	5
Attenuation at passband corner (dB)	0

The zeros/poles locations of the optimized Inverse Chebyshev filter in the z-plane are shown in Fig. 6.26 and the frequency response is shown in Fig. 6.27.

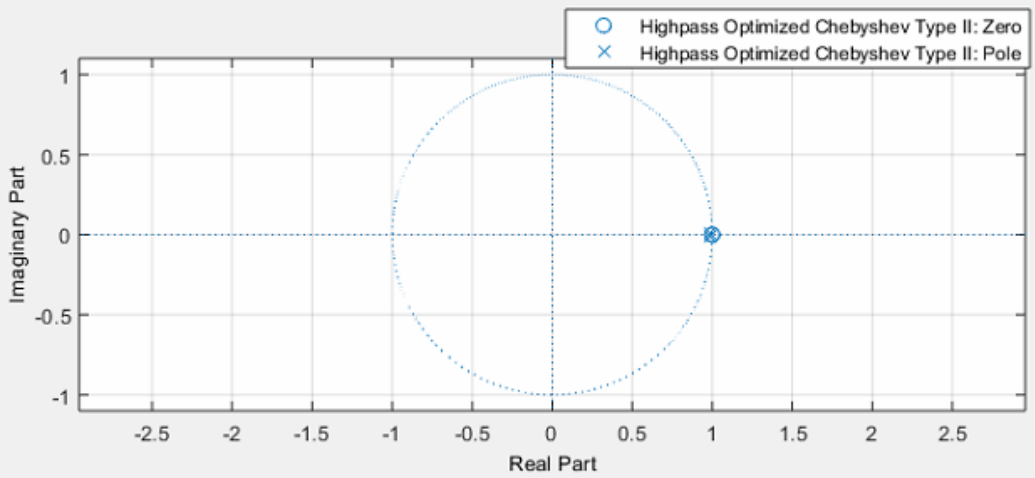

Fig. 6.26: Customized filter highpass section: optimized design → poles/zeros location.

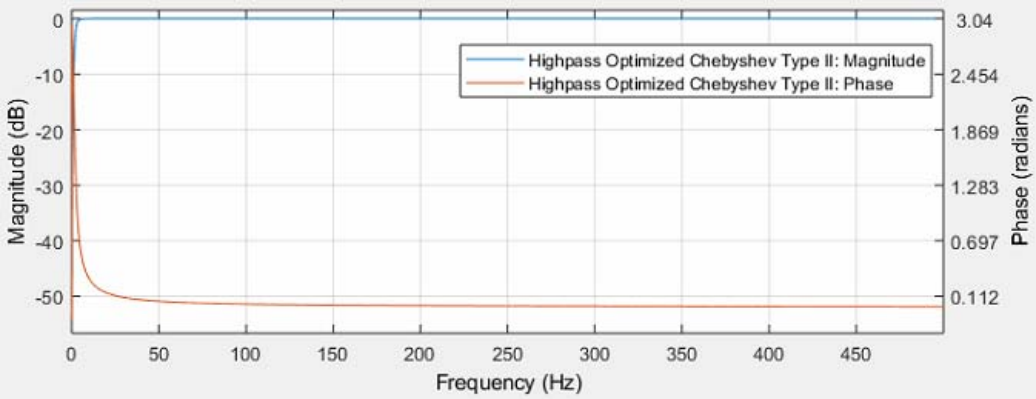

Fig. 6.27: Customized filter highpass section: optimized design → frequency response.

The transfer function of the optimized Inverse Chebyshev design is:

$$\frac{0.9909\ z\text{^}2\ -\ 1.982\ z\ +\ 0.9909}{\text{z\^{}2}\ -\ 1.982\ \text{z}\ +\ 0.9818}$$

The zeros and poles are at

$$z_1 = 0.999999\ +\ 0.001333i$$
$$z_2 = 0.999999\ -\ 0.001333i$$
$$p_1 = 0.990811\ +\ 0.009120i$$
$$p_2 = 0.990811\ -\ 0.009120i$$

By the location of the poles and zeros, we can see that the system is stable (all poles inside the unit circle) and minimum-delay (all zeros inside the unit circle). Fig. 6.28 is the zoomed-in frequency response until 10 Hz. It is possible to see the ripple in the stopband which allows a steep roll-off in the transition band. The range between 0 Hz (DC) and 0.3 Hz is even below the desired -39.65 dB. Moreover, this design was optimized to reduce the error in the passband and the attenuation at 5 Hz (start of passband) is very close to 0 dB.

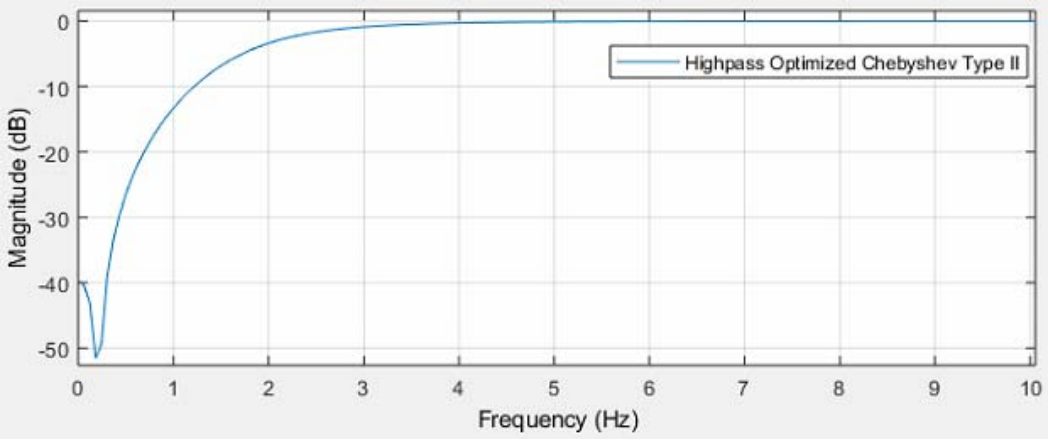

Fig. 6.28: Customized filter highpass section: optimized design → zoomed-in frequency response until 10 Hz.

By cascading the optimized Inverse Chebyshev filter to the customized lowpass filter, we get the following transfer function:

$$\frac{0.335\,z\text{^}4\ -\ 0.335\,z\text{^}3\ -\ 0.335\,z\text{^}2\ +\ 0.335\,z}{\text{z\^{}4}\ -\ 2.305\,\text{z\^{}3}\ +\ 1.624\,\text{z\^{}2}\ -\ 0.318\,\text{z}}$$

The zeros and poles are at

$$z_1 = 0$$
$$z_2 = -1$$
$$z_3 = 0.999999\ +\ 0.001333i$$
$$z_4 = 0.999999 -\ 0.001333i$$
$$p_1 = 0$$
$$p_2 = 0.3239$$
$$p_3 = 0.990811\ +\ 0.009120i$$
$$p_4 = 0.990811 -\ 0.009120i$$

It is very difficult to build perfect control systems and place the zeros and poles exactly where we want them when dealing with analog filters. Such situations can lead to an unstable or undesired system response. However, in the case of digital filters, pole/zero cancellation is possible and will, in this case, lead to a filter of order 3 instead of order 4, therefore reducing time delay. We then get the following transfer function:

$$\frac{0.335\,z\text{^}3\ -\ 0.335\,z\text{^}2\ -\ 0.335\,z\text{^}1\ +\ 0.335}{\text{z\^{}3}\ -\ 2.305\,\text{z\^{}2}\ +\ 1.624\,\text{z\^{}1}\ -\ 0.318}$$

The zeros and poles are at:

$$z_1 = -1$$
$$z_2 = 0.999999\ +\ 0.001333i$$
$$z_3 = 0.999999 -\ 0.001333i$$
$$p_1 = 0.3239$$
$$p_2 = 0.990811\ +\ 0.009120i$$
$$p_3 = 0.990811 -\ 0.009120i$$

6.4.4 Proposed detection method: power spectrum + frequency/magnitude/derivative estimators

The power spectrum method was used with a Hamming window function of length N = 30 samples to reduce spectral leakage without completely nullifying the edges of the window and, therefore, avoiding high ENBW levels. Equation (4-46), used for the frequency and magnitude estimation, is set with $l = 1$ bin in each side of the main detected bin. Equation (4-50) is used for the derivative of magnitude estimation. Filter designs 1, 2 and 3 for the active power input signal were used and the same time-domain procedure of item "6.3.2 - Time-domain transient simulation" was used for the SSCI simulation.

6.4.4.1 Case without the application of a fault

Fig. 6.29 and Fig. 6.30 show the results without the application of a fault (just tripping the transmission line at t = 20 s) until 20.8 s and 20.3 s of simulation time, respectively.

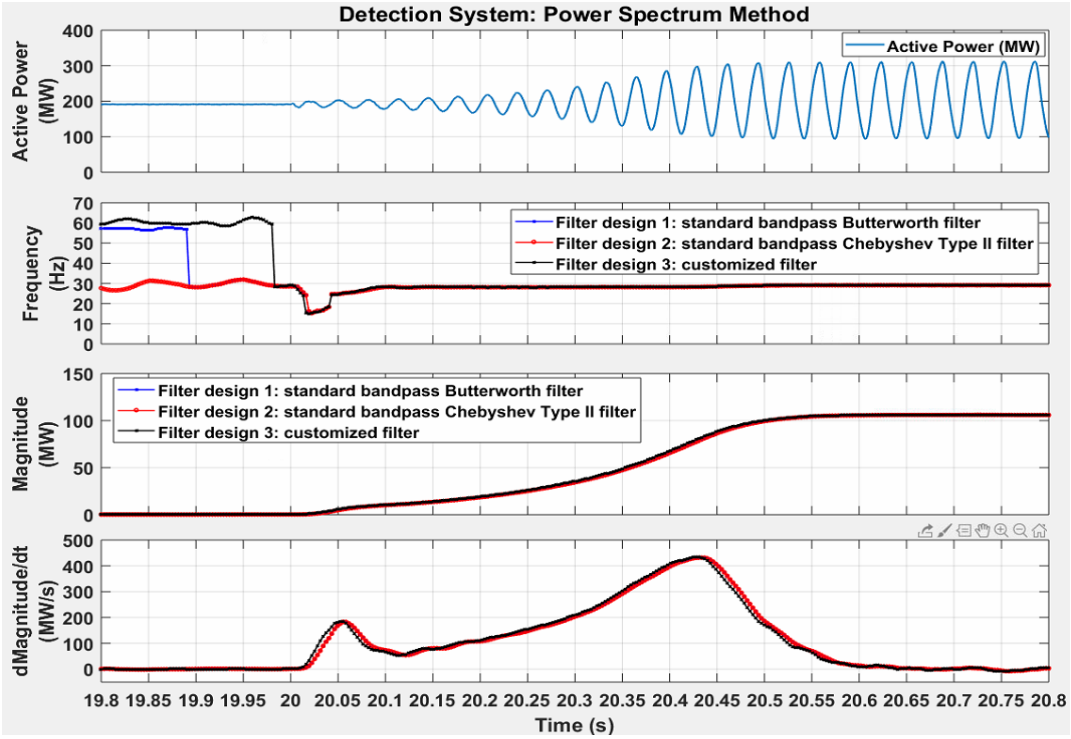

Fig. 6.29: Power Spectrum detection method with different filter designs without fault condition until 20.8 s.

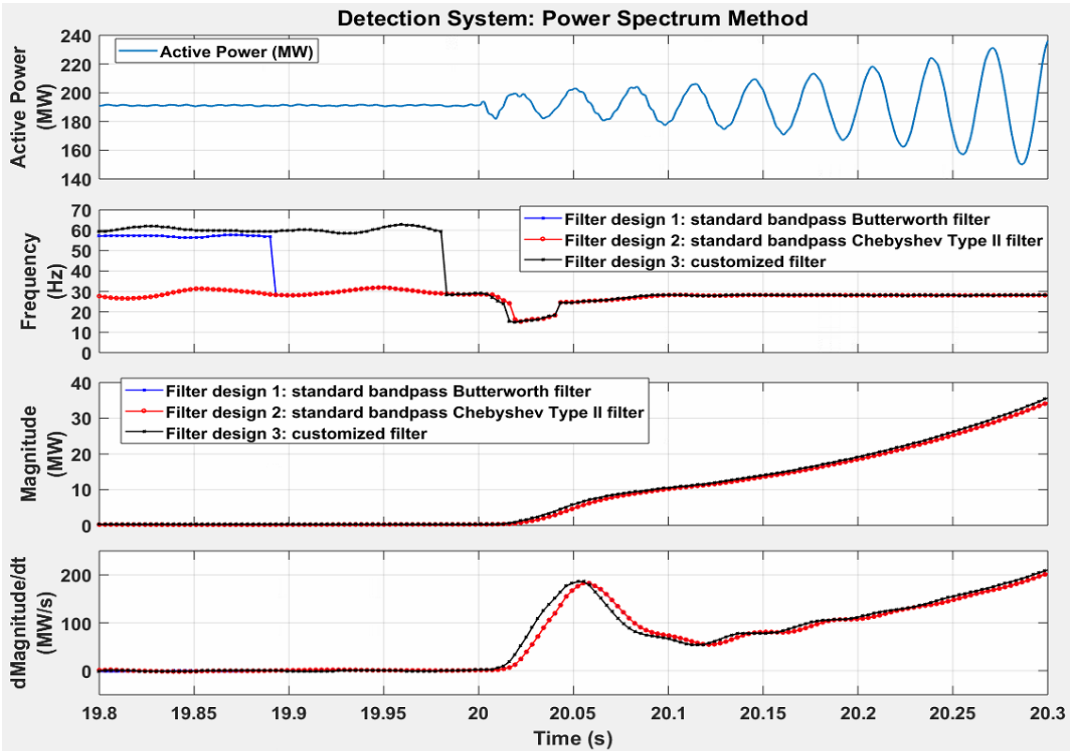

Fig. 6.30: Power Spectrum detection method with different filter designs without fault condition until 20.3 s.

The final results for the no-fault case are shown in Table 6.11 for the pickup times and for the final values taken at t=20.8 s.

Table 6.11: Power spectrum method results for the no-fault case.

Design 1 pickup time instant	20.045 seconds
Design 2 pickup time instant	20.045 seconds
Design 3 pickup time instant	20.040 seconds
Frequency of oscillation – final value	29.12 Hz
Magnitude of oscillation – final value	106.08 MW

We can see that the proposed detection method quickly detects the oscillation due to sub-synchronous control interaction between the wind farms and the series-compensated network that starts at t = 20 s. At this time, the Panhandle area - which contains the two wind farms – becomes radially connected to the series-compensated line between the Miami and Denton stations after the tripping of the transmission line between Miami and Wichita Falls. At t = 20.045 s, only 45 ms after the radial condition, the detection system using either the standard bandpass Butterworth (filter design 1) or the standard bandpass Inverse Chebyshev (filter design 2) filter detects the SSCI condition. From Fig. 6.30 we can actually see the magnitude increasing earlier than that and a protection engineer could as well set the sensitivity of the system differently. As a matter of fact, the derivative of the magnitude shows an increase from the point that the radial condition happens. At t = 20.01 s, only 10 ms after the radial condition, it becomes very clear that an SSCI condition is happening. The detected frequencies are within the sub-synchronous range and both the magnitude and the derivative of magnitude are positive. The customized filter (filter design 3) performed even better, with a pickup time of only 40 ms, and it is possible to clearly visualize the faster response in all plots. This shows that the filter performance is of uttermost importance in an SSR detection system. This is an interesting conclusion, as most of the current literature that concerns SSR detection systems either do not discuss the impact of filters and/or consider ideal filters, or they do not provide a detection system that can be applied throughout the whole sub-synchronous

range (5 to 55 Hz), for example, by having to tune the filters to a more restricted frequency range.

The time-domain transient simulation results of item “6.3.2 - Time-domain transient simulation” performed during validation of the optimized frequency scanning tool and Fig. 6.10 show that the frequency of oscillation is 29.34 Hz with a magnitude of 113.94 MW. The errors are:

$$\frac{f_{SSR} - f_{detected}}{f_{SSR}} * 100\% = \frac{29.34 - 29.12}{29.34} * 100\% = 0.75\%$$

$$\frac{Magnitude_{SSR} - Magnitude_{detected}}{Magnitude_{SSR}} * 100\% = \frac{113.94 - 106.08}{113.94} * 100\% = 6.90\%$$

6.4.4.2 Case with the application of a short-circuit

Fig. 6.31 shows the results with the application of a three-phase fault as previously described at t = 19.95 s with subsequent tripping of the transmission line at t = 20 s.

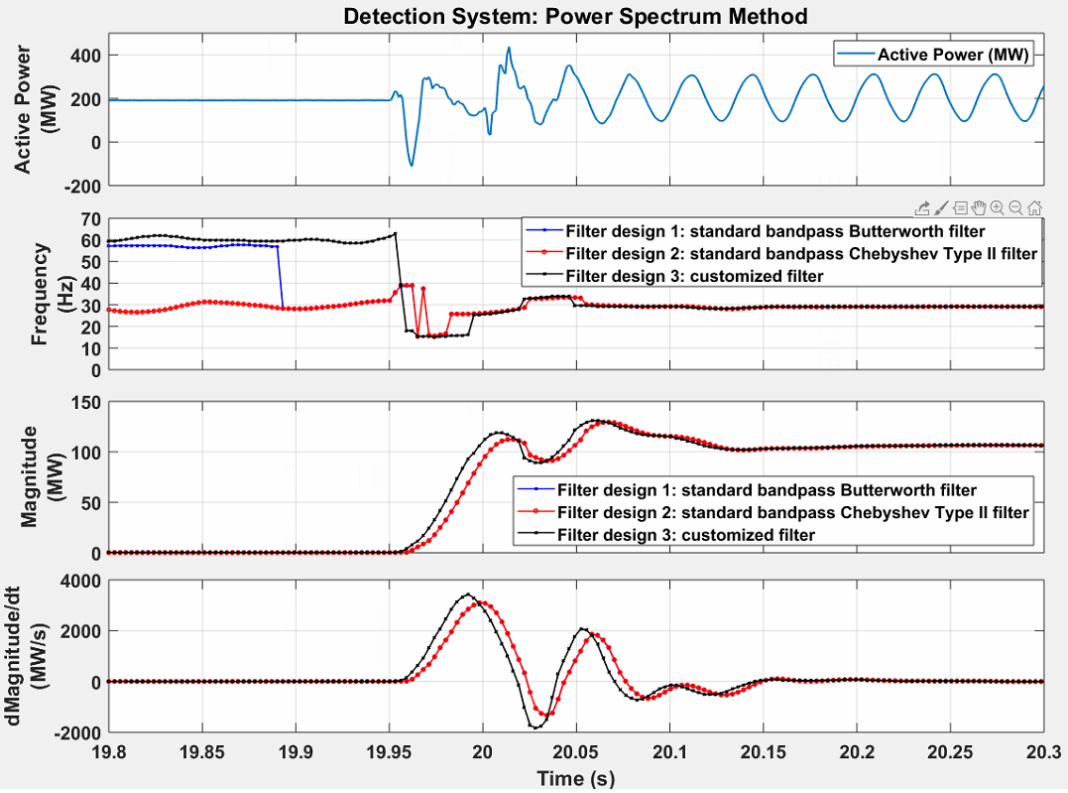

Fig. 6.31: Power Spectrum detection method with different filter designs under fault condition.

The final results for the short-circuit case are shown in Table 6.12 for the pickup times and for the final values taken at t = 20.8 s.

Table 6.12: Power spectrum method results for the short-circuit case.

Design 1 pickup time instant	19.964 seconds
Design 2 pickup time instant	19.964 seconds
Design 3 pickup time instant	19.960 seconds
Frequency of oscillation – final value	29.08 Hz
Magnitude of oscillation – final value	106.28 MW

The error values for the detected frequency and detected magnitude are:

$$\frac{f_{SSR} - f_{detected}}{f_{SSR}} * 100\% = \frac{29.34 - 29.08}{29.34} * 100\% = 0.89\%$$

$$\frac{Magnitude_{SSR} - Magnitude_{detected}}{Magnitude_{SSR}} * 100\% = \frac{113.94 - 106.28}{113.94} * 100\% = 6.72\%$$

These are very low values of errors for extremely fast detection systems that use a very restricted number of samples (N = 30 samples in this case). We could choose to increase the numbers of samples to improve accuracy at the expense of slower detection time. Different applications have different requirements. Protection systems that intend to trip a wind turbine, for example, have higher speed requirements than accuracy requirements. A mitigation scheme that uses the numerical results of the detection system may need to be more accurate. Monitoring systems for alarm and post-event analysis purposes may be slower, but with improved accuracy.

Moreover, in the case of a fault condition at t = 19.95 s, we can see that the SSCI modes are triggered even before the radial condition at t = 20 s due to the high perturbation of these modes. The detection system picked up at t = 19.964 s for the filter designs 1 and 2, only 14 ms after the large disturbance, and at t = 19.960 s for the filter design 3, only 10 ms after the fault. Despite the large disturbance, we can observe the fast trend of the detected frequency to converge to the final 29.08 Hz, showing the robustness of the proposed method.

6.4.5 Detection method comparison: power spectrum (proposed) vs matrix pencil

This item presents a comparison between the proposed power spectrum method and the matrix pencil (MP) method. The MP was chosen due to the fast performance of modal identification methods for sub-synchronous resonance applications. Other modal identification techniques include the Prony and the Eigensystem realization algorithm (ERA), whose performances for SSR detection were tested in reference [30], despite the shorter sub-synchronous frequency range used. The MP method is a more robust and computationally efficient algorithm that presents a low variance of the parameter estimates among modal identification techniques [90].

In this test, the customized filter (design 3) was used, as it presents the best performance. The window length was maintained at N = 30 samples and the case with the application of a short-circuit was used. The results are shown in Fig. 6.32 and Table 6.13.

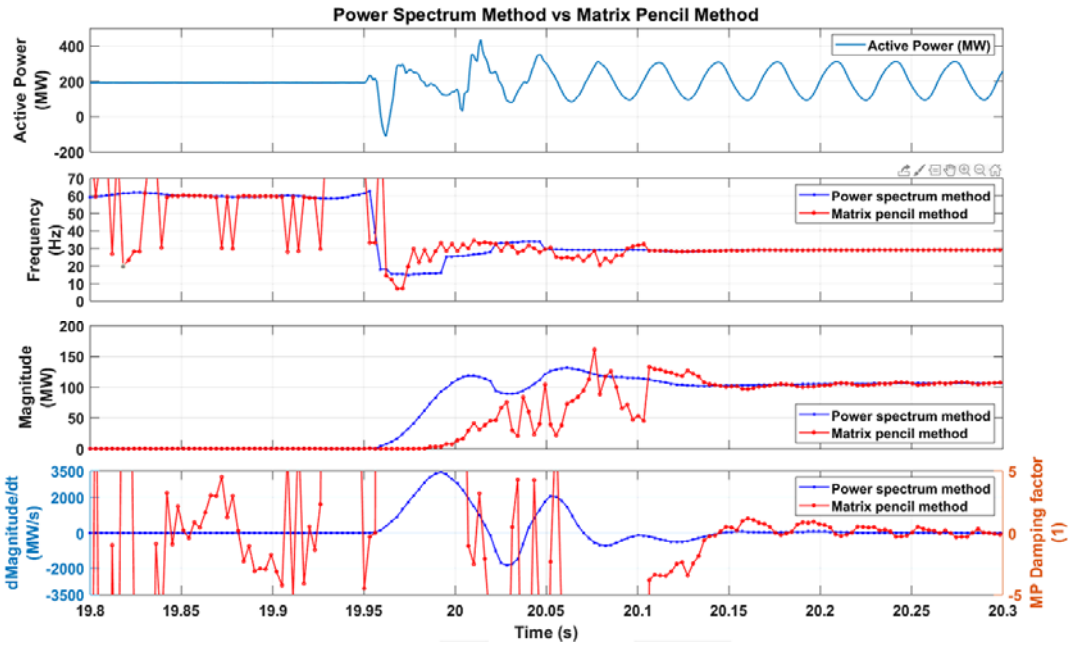

Fig. 6.32: Power spectrum method vs matrix pencil method results.

Table 6.13: Power spectrum method vs matrix pencil method results.

-	**Power Spectrum**	**Matrix Pencil**
Design 3 pickup time instant	19.960 seconds	19.990 seconds
Frequency of oscillation – final value	29.08 Hz	29.15 Hz
Magnitude of oscillation – final value	106.28 MW	107.01 MW

From the frequency plot, we can see that the MP method also starts detecting a sub-synchronous oscillation right after the fault applied at $t = 19.95\ s$, but the increase in the detected magnitude takes longer than in the proposed method, resulting in a pickup time 30 ms later.

The matrix pencil does not utilize the derivative of magnitude calculation. It utilizes the damping factor calculated from the eigenvalues (real part of the eigenvalue). An unstable system is represented by a positive damping factor – which is equivalent to an eigenvalue in the right-half plane of the s-plane. Therefore, both methods represent an unstable system by a positive value of the fourth subplot of Fig. 6.32, but the left y-axis is for the derivative for the power spectrum method while the right y-axis is for the damping factor of the matrix pencil method. We can observe that the proposed method is much more robust while the matrix pencil method is extremely sensitive. Eventually, it converges to approximately the same detected frequency and magnitude of the proposed method (29.15 Hz vs 29.08 Hz and 107.01 MW vs 106.28 MW). However, the variance in the detected magnitude is reflected in the damping factor (and so it would in a derivative calculation), which makes real-time decisions more difficult.

6.4.6 Computational burden

The detection system was thoroughly tested within the real-time system described in item “6.1 - Dual-modular-redundant monitoring system validation”. Each sample is processed in under 0.33 ms. For a sampling rate of 1000 Hz, the sampling period is 1 ms, which gives 0.67 ms of spare time between samples, equivalent to 67 % of spare time. Hence, the proposed algorithm should perform well in most real-time devices for these types of applications, aside from the differences in how instructions are performed in different processors and assuming equivalent or higher computational power.

7 CONCLUSION AND FUTURE WORK

This dissertation was focused on sub-synchronous resonance, especially the sub-synchronous control interaction phenomenon that DFIG-based wind farms are prone to experience. This type of interaction results in an extremely fast increase of sub-synchronous oscillations due to the purely electric nature of the phenomenon, that is, the mechanical inertia usually involved in some other types of interactions, such as torsional interaction, does not slow down the increase in oscillations. The action of controllers also plays a major role in these types of events, which are therefore greatly influenced by the increasing penetration of renewable generation and power-electronic-based devices. This dissertation was mainly divided into two main parts: risk assessment analysis and monitoring/detection.

For risk assessment, the harmonic injection method is a strong frequency scanning technique for black-box models with nonlinear devices, such as many that are present in active devices. The accuracy of this method is highly dependent on the number of injected frequencies in each simulation. Normally, the lesser the number of multiple frequencies, the higher the accuracy. The ideal case is performing one simulation per single-frequency injection. However, this accuracy is only achieved at the expense of time and financial costs. This dissertation proposes a technique to increase the accuracy of the scan results by optimizing the crest factor of a multi-frequency injection signal. This signal enables performing only one simulation per side of the grid, therefore drastically reducing the total simulation time while maintaining good accuracy. The proposed method was utilized to scan two wind farm black-box models and a VSC-based STATCOM to evaluate the risk of SSR in a portion of the Texas synthetic grid. The frequency scan results were benchmarked against the ideal case of multiple single-frequency injections and demonstrated high accuracy while being 11.71 times faster. Moreover, when compared with other methods, the proposed method showed superiority in terms of accuracy and robustness. Finally, time-domain transient simulations were conducted to validate the results of the frequency scan. Future work could include a deep analysis of nonlinearities that affect frequency scanning. Some nonlinearities may produce negative-sequence components with the injection of a positive-sequence signal. The correct modeling of such nonlinearities can be done by means of system identification approaches in the actual hardware under analysis, e.g., a doubly-fed induction generator (DFIG). System

identification consists of an input-output approach using, for example, different multi-frequency input signals to more accurately model the system response using nonlinear equations.

For the monitoring system, firstly, a dual modular redundancy (DMR) scheme was proposed containing a CPU-FPGA heterogeneous platform and several mechanisms to improve data redundancy, hardware redundancy, and overall reliability. The system was fully tested and proved to be functional and efficient. The hybrid platform was able to get the best of both domains. The FPGA is able to process large volumes of data while maintaining units synchronized, being well suited for the signal conditioning and SSR detection scheme. The CPU performs functions of low data rate and less frequent tasks, such as data display and data logging while keeping costs lower. All the functions implemented proved their effectiveness in improving reliability. As a majority-based voting system is not feasible in DMR configurations, a health indicator is built for each unit with the results of the developed self-monitoring schemes. A software-based voter implemented within the interface system uses the health indicators to decide which unit (main or backup) will forward the data to the subsystems ahead. Moreover, data redundancy is a subject frequently left aside regarding monitoring systems. This design included it in the same discussion of a whole redundant mechanism for monitoring systems by providing a redundant array of independent disks (RAID) configuration by means of a network-attached storage (NAS). Finally, future work could include other possibilities to improve the reliability of monitoring systems, such as duplicating the DC power supply, the controller power supply, the batteries, and the communication channels. However, the reliability-cost ratio should be assessed considering the specific needs of the companies installing the redundant system, as these additional features will also result in additional costs.

For the second part of the monitoring system, an SSR detection system was described along with signal conditioning and filtering techniques, which are as important as the detection algorithm itself, but not usually addressed in literature or with the assumption of ideal conditioning or limited range of efficacy. In this dissertation, a detection method based on the power spectrum of the input signal, a frequency/magnitude estimator and a derivative estimator was proposed. The techniques in this system considered the whole sub-synchronous range of 5 Hz to 55 Hz without any limitations in

the range, which can be achieved by properly designing a filter that provides the flattest response in the passband while sufficiently attenuating the stopband according to the grid requirements. Special attention should be paid to achieving the lowest possible filter order in order to reduce delay during signal processing. This method allows for the use of small windows, as long as they are properly tapered, therefore reducing the detection time. The choice of window length will depend on a tradeoff between speed and accuracy. The larger the window, the more accurate it will be, but it may result in longer detection times. Such windows may be used for post-event analysis. A shorter window can reduce detection time at the expense of accuracy. However, the Texas synthetic grid case study showed that accuracy was still high with frequency estimation errors of less than 1% and magnitude estimation errors in the order of only 6%, and is, therefore, a good choice for fast protection systems. The case studies showed a detection pickup time of 40 ms after the radial condition between the wind-farm region and the series-compensated line for the case without fault and, for the case with the application of a short-circuit, a detection pickup time of only 10 ms after the short-circuit due to the large perturbation of the natural modes of the system. Finally, medium-length windows may be used for other applications, such as mitigation mechanisms that require a certain level of accuracy within relatively short amounts of time.

The complete monitoring system was implemented in a real-time device to test its real-world time consumption and showed that all the signal and data processing takes only 33% of the sampling period for every new input sample processed, which gives 67% of stand-by time, therefore showing great usability in monitoring systems. Future work could include the development of mitigation schemes. These could be implemented by means of FACTS devices; real-time change of DFIG controller parameters; control of series-capacitors; control of damper windings; and several filtering solutions, among others. However, whenever viable, the preferred choice of mitigation should be modifying the power system design during grid planning or update efforts, although not always possible.

Publications

1. L. Zhao, Y. Zhou, **I. Matsuo**, S. Korkua and W. Lee, "The Design of a Remote Online Holistic Monitoring System for a Wind Turbine," in IEEE Transactions on Industry Applications, in press, 2019. doi: 10.1109/TIA.2019.2951088
2. **I. B. M. Matsuo**, F. Salehi, L. Zhao, Y. Zhou and W. Lee, "Optimized Frequency Scanning of Nonlinear Devices Applied to Sub-Synchronous Resonance Screening," in IEEE Transactions on Industry Applications.
3. Y. Zhou, L. Zhao, **I. Matsuo** and W. Lee, "An Improved Aggregated Equivalent Modeling of DFIG Wind Farm Based on Dynamic Clustering Strategy for Post-fault Analysis," 2019 IEEE Industry Applications Society Annual Meeting (IAS), Baltimore, MD, pp. 1-8, 2019.
4. L. Zhao, **I. Brandao Machado Matsuo**, Y. Zhou and W. Lee, "Design of an Industrial IoT-Based Monitoring System for Power Substations," in IEEE Transactions on Industry Applications, vol. 55, no. 6, pp. 5666-5674, Nov.-Dec. 2019.
5. F. Salehi, **I. B. M. Matsuo**, A. Brahman, M. Aghazadeh Tabrizi and W. Lee, "Sub-Synchronous Control Interaction Detection: A Real-Time Application," in IEEE Transactions on Power Delivery, in press, 2019. doi: 10.1109/TPWRD.2019.2930400
6. Y. Zhou, L. Zhao, **I. B. M. Matsuo** and W. Lee, "A Dynamic Weighted Aggregation Equivalent Modeling Approach for the DFIG Wind Farm Considering the Weibull Distribution for Fault Analysis," in IEEE Transactions on Industry Applications, vol. 55, no. 6, pp. 5514-5523, Nov.-Dec. 2019.
7. **I. B. M. Matsuo**, F. Salehi, L. Zhao, Y. Zhou and W. Lee, "An Optimized Frequency Scanning Tool for Sub-Synchronous Interaction Analysis of Non-Linear Devices," 2019 IEEE/IAS 55th Industrial and Commercial Power Systems Technical Conference (I&CPS), Calgary, AB, Canada, pp. 1-7, 2019.
8. Y. Zhou, L. Zhao, **I. B. M. Matsuo** and W. Lee, "A Dynamic Weighted Aggregation Equivalent Modeling Approach for the DFIG Wind Farm Considering the Weibull Distribution," 2019 IEEE/IAS 55th Industrial and Commercial Power Systems Technical Conference (I&CPS), Calgary, AB, Canada, pp. 1-7, 2019.
9. L. Zhao, **I. Matsuo**, Y. Zhou and W. Lee, "Design of an Industrial IoT-Based Monitoring System for Power Substations," 2019 IEEE/IAS 55th Industrial and Commercial Power Systems Technical Conference (I&CPS), Calgary, AB, Canada, pp. 1-6, 2019.
10. L. Zhao, Y. Zhou, **I. Matsuo**, S. K. Korkua and W. Lee, "The Design of a Holistic IoT-Based Monitoring System for a Wind Turbine," 2019 IEEE/IAS 55th Industrial and Commercial Power Systems Technical Conference (I&CPS), Calgary, AB, Canada, pp. 1-7, 2019.
11. L. Zhao, **I. B. M. Matsuo**, F. Salehi, Y. Zhou and W. Lee, "Development of a Real-Time Web-Based Power Monitoring System for the Substation of Petrochemical Facilities," in IEEE Transactions on Industry Applications, vol. 55, no. 1, pp. 43-50, Jan.-Feb. 2019.
12. F. Salehi, **I. B. M. Matsuo** and W. Lee, "Detection of Sub-Synchronous Control Interaction (SSCI) Using Modal Identification Analysis and FFT," 2018 North American Power Symposium (NAPS), Fargo, ND, pp. 1-5, 2018.

13. **I. B. M. Matsuo**, L. Zhao and W. Lee, "A Dual Modular Redundancy Scheme for CPU–FPGA Platform-Based Systems," in IEEE Transactions on Industry Applications, vol. 54, no. 6, pp. 5621-5629, Nov.-Dec. 2018.
14. L. Zhao, **I. Matsuo**, F. Salehi, Y. Zhou and W. Lee, "Development of a Real-Time Web-Based Power Monitoring system for the substation of petrochemical facilities," 2018 IEEE/IAS 54th Industrial and Commercial Power Systems Technical Conference (I&CPS), Niagara Falls, ON, pp. 1-6, 2018.
15. **I. B. M. Matsuo**, L. Zhao and W. Lee, "A CPU-FPGA heterogeneous platform-based monitoring system and redundant mechanisms," 2018 IEEE/IAS 54th Industrial and Commercial Power Systems Technical Conference (I&CPS), Niagara Falls, ON, pp. 1-6, 2018.

References

[1] D. N. Walker, C. E. J. Bowler, R. L. Jackson and D. A. Hodges, "Results of subsynchronous resonance test at Mohave," in IEEE Transactions on Power Apparatus and Systems, vol. 94, no. 5, pp. 1878-1889, Sept. 1975.

[2] M. Bahrman, E. V. Larsen, R. J. Piwko and H. S. Patel, "Experience with HVDC - Turbine-Generator Torsional Interaction at Square Butte," in IEEE Transactions on Power Apparatus and Systems, vol. PAS-99, no. 3, pp. 966-975, May 1980.

[3] L. C. Gross, "Sub-synchronous grid conditions: New event, new problem, and new solutions," in Proc. Western Protective Relay Conference, 2010, pp. 1–5.

[4] D. Kidd and P. Hassink, "Transmission operator perspective of Sub-Synchronous Interaction," PES T&D 2012, Orlando, FL, 2012, pp. 1-3.

[5] J. Adams, C. Carter and S. Huang, "ERCOT experience with Sub-synchronous Control Interaction and proposed remediation," PES T&D 2012, Orlando, FL, 2012, pp. 1-5.

[6] Y. H. Wan, "Synchronized phasor data for analyzing wind power plant dynamic behavior and model validation", National Renewable Energy Laboratory technical report, Tech. Rep. NREL/TP-5500-57342, Jan. 2013.

[7] L. Vanfretti, M. Baudette, J. L. Domínguez-Garcíaz, A. White, M. S. Almas and J. O. Gjerdeóy, "A PMU-based fast real-time sub-synchronous oscillation detection application," 2015 IEEE 15th International Conference on Environment and Electrical Engineering (EEEIC), Rome, 2015, pp. 1892-1897.

[8] K. Narendra et al., "New microprocessor based relay to monitor and protect power systems against sub-harmonics," 2011 IEEE Electrical Power and Energy Conference, Winnipeg, MB, 2011, pp. 438-443.

[9] Y. Zhao, H. Cui, H. Huo and Y. Nie, "Application of Synchrosqueezed Wavelet Transforms for Extraction of the Oscillatory Parameters of Subsynchronous Oscillation in Power Systems," in Energies (MDPI), June 2018.

[10] L. Wang, X. Xie, Q. Jiang, H. Liu, Y. Li and H. Liu, "Investigation of SSR in Practical DFIG-Based Wind Farms Connected to a Series-Compensated Power System," in IEEE Transactions on Power Systems, vol. 30, no. 5, pp. 2772-2779, Sept. 2015.

[11] X. Lu et al., "Mitigation of Sub-Synchronous Control Interaction in Wind Power systems with GA-SA tuned Damping Controller," in Elsevier International Federation of Automatic Control, vol. 50, no. 1, Jul. 2017.

[12] H. Liu et al., "Subsynchronous Interaction Between Direct-Drive PMSG Based Wind Farms and Weak AC Networks," in IEEE Transactions on Power Systems, vol. 32, no. 6, pp. 4708-4720, Nov. 2017.

[13] S. H. Huang and Y. Gong, "South Texas SSR", ERCOT ROS Meeting, May 2018. Available: http://www.ercot.com/content/wcm/key_documents_lists/139265/10._South_Texas_SSR_ERCOT_ROS_May_2018_rev1.pdf, accessed 10 October 2019.

[14] "Reader's guide to subsynchronous resonance," in IEEE Transactions on Power Systems, vol. 7, no. 1, pp. 150-157, Feb. 1992.

[15] A. E. Leon and J. A. Solsona, "Sub-synchronous interaction damping control for DFIG wind turbines," in IEEE Transactions on Power Systems, vol. 30, no. 1, pp. 419-428, Jan. 2015.

[16] "Terms, Definitions and Symbols for Subsynchronous Oscillations," in IEEE Transactions on Power Apparatus and Systems, vol. PAS-104, no. 6, pp. 1326-1334, June 1985.
[17] V.B. Virulkar, G.V. Gotmare, “Sub-synchronous resonance in series compensated wind farm: a review”, in Renewable and Sustainable Energy Reviews, vol. 55, pp. 1010-1029, 2016.
[18] M. Bongiorno and A. Petersson, "The impact of wind farms on subsynchronous resonance in power systems,” – Elforsk rapport 11:29, 2011.
[19] L. Fan, R. Kavasseri, Z. L. Miao and C. Zhu, "Modeling of DFIG-based wind farms for SSR analysis," in IEEE Transactions on Power Delivery, vol. 25, no. 4, pp. 2073-2082, Oct. 2010.
[20] Z. Miao, "Impedance-model-based SSR analysis for type 3 wind generator and series-compensated network," in IEEE Transactions on Energy Conversion, vol. 27, no. 4, pp. 984-991, Dec. 2012.
[21] P. Fischer de Toledo, L. Angquist and H. -. Nee, "Frequency-domain modelling of sub-synchronous torsional interaction of synchronous machines and a high voltage direct current transmission link with line-commutated converters," in IET Generation, Transmission & Distribution, vol. 4, no. 3, pp. 418-431, March 2010.
[22] F. Mei and B. C. Pal, "Modeling of doubly-fed induction generator for power system stability study," 2008 IEEE Power and Energy Society General Meeting - Conversion and Delivery of Electrical Energy in the 21st Century, Pittsburgh, PA, 2008, pp. 1-8.
[23] I. Erlich, J. Kretschmann, J. Fortmann, S. Mueller-Engelhardt and H. Wrede, "Modeling of wind turbines based on doubly-fed induction generators for power system stability studies," in IEEE Transactions on Power Systems, vol. 22, no. 3, pp. 909-919, Aug. 2007.
[24] Y. Zhou, L. Zhao, I. B. M. Matsuo and W. Lee, "A Dynamic Weighted Aggregation Equivalent Modeling Approach for the DFIG Wind Farm Considering the Weibull Distribution for Fault Analysis," in IEEE Transactions on Industry Applications, vol. 55, no. 6, pp. 5514-5523, Nov.-Dec. 2019.
[25] ERCOT nodal protocols: Sub-synchronous Resonance, ERCOT NPRR 562, 2018.
[26] L. Fan and Z. Miao, "Nyquist-stability-criterion-based SSR explanation for type-3 wind generators," in IEEE Transactions on Energy Conversion, vol. 27, no. 3, pp. 807-809, Sept. 2012.
[27] L. Piyasinghe, Z. Miao, J. Khazaei and L. Fan, "Impedance Model-Based SSR Analysis for TCSC Compensated Type-3 Wind Energy Delivery Systems," in IEEE Transactions on Sustainable Energy, vol. 6, no. 1, pp. 179-187, Jan. 2015.
[28] Y. Song and F. Blaabjerg, "Analysis of Middle Frequency Resonance in DFIG System Considering Phase-Locked Loop," in IEEE Transactions on Power Electronics, vol. 33, no. 1, pp. 343-356, Jan. 2018.
[29] L. Zhao, I. B. M. Matsuo, F. Salehi, Y. Zhou and W. Lee, "Development of a Real-Time Web-Based Power Monitoring System for the Substation of Petrochemical Facilities," in IEEE Transactions on Industry Applications, vol. 55, no. 1, pp. 43-50, Jan.-Feb. 2019.
[30] F. Salehi, I. Brandao Machado Matsuo, A. Brahman, M. Aghazadeh Tabrizi and W. Lee, "Sub-Synchronous Control Interaction Detection: A Real-Time Application," in IEEE Transactions on Power Delivery, in press, 2019. doi: 10.1109/TPWRD.2019.2930400

[31] H. K. Nia, F. Salehi, M. Sahni, N. Karnik and H. Yin, "A filter-less robust controller for damping SSCI oscillations in wind power plants," 2017 IEEE Power & Energy Society General Meeting, Chicago, IL, 2017, pp. 1-1.

[32] F. Salehi, I. B. M. Matsuo and W. Lee, "Detection of Sub-Synchronous Control Interaction (SSCI) Using Modal Identification Analysis and FFT," 2018 North American Power Symposium (NAPS), Fargo, ND, pp. 1-5, 2018.

[33] I. B. M. Matsuo, F. Salehi, L. Zhao, Y. Zhou and W. Lee, "Optimized Frequency Scanning of Nonlinear Devices Applied to Sub-Synchronous Resonance Screening," in IEEE Transactions on Industry Applications.

[34] I. B. M. Matsuo, F. Salehi, L. Zhao, Y. Zhou and W. Lee, "An Optimized Frequency Scanning Tool for Sub-Synchronous Interaction Analysis of Non-Linear Devices," 2019 IEEE/IAS 55th Industrial and Commercial Power Systems Technical Conference (I&CPS), Calgary, AB, Canada, 2019, pp. 1-7.

[35] M. S. Annakkage, C. Karawita and U. D. Annakkage, "Frequency Scan-Based Screening Method for Device Dependent Sub-Synchronous Oscillations," in IEEE Transactions on Power Systems, vol. 31, no. 3, pp. 1872-1878, May 2016.

[36] L. Yang, Z. Xu, J. Østergaard, Z. Y. Dong, K. P. Wong and X. Ma, "Oscillatory Stability and Eigenvalue Sensitivity Analysis of A DFIG Wind Turbine System," in IEEE Transactions on Energy Conversion, vol. 26, no. 1, pp. 328-339, March 2011.

[37] M. Sahni, D. Muthumuni, B. Badrzadeh, A. Gole and A. Kulkarni, "Advanced screening techniques for Sub-Synchronous Interaction in wind farms," PES T&D 2012, Orlando, FL, 2012, pp. 1-9.

[38] Y. Cheng, S. Huang, J. Rose, V. A. Pappu and J. Conto, "ERCOT subsynchronous resonance topology and frequency scan tool development," 2016 IEEE Power and Energy Society General Meeting (PESGM), Boston, MA, 2016, pp. 1-5.

[39] A. S. Subburaj et al., "Determination of Sub Synchronous Control Interaction between Wind Turbines and Series Compensated Transmission Lines," in International Journal of Renewable Energy Research, vol. 6, no. 3, pp. 987-994, 2016.

[40] A. M. Kulkarni, M. K. Das and A. M. Gole, "Frequency scanning analysis of STATCOM - network interactions," 2016 IEEE 6th International Conference on Power Systems (ICPS), New Delhi, 2016, pp. 1-6.

[41] X. Jiang and A. M. Gole, "A frequency scanning method for the identification of harmonic instabilities in HVDC systems," in IEEE Transactions on Power Delivery, vol. 10, no. 4, pp. 1875-1881, Oct. 1995.

[42] R. Pintelon and J. Schoukens, System Identification: A Frequency Domain Approach, New York: IEEE, 2001.

[43] C. Basso, 'Small-Signal Modeling and Analytical Analysis of Power Converters', Applied Power Electronics Conference and Exposition, 2013.

[44] IXYS, IXSH 35N120A High Voltage, High Speed IGBT. [Online]. Available: http://ixapps.ixys.com/datasheet/92774.pdf

[45] J. M. Guerrero, M. Leetmaa, F. Briz, A. Zamarron and R. D. Lorenz, "Inverter nonlinearity effects in high-frequency signal-injection-based sensorless control methods," in IEEE Transactions on Industry Applications, vol. 41, no. 2, pp. 618-626, March-April 2005.

[46] S. Boyd and L. Vandenberghe, Convex Optimization, New York: Cambridge University Press, 2004, pp. 215-223.

[47] J. Schoukens, R. M. Pintelon and Y. J. Rolain, "Broadband versus stepped sine FRF measurements," in IEEE Transactions on Instrumentation and Measurement, vol. 49, no. 2, pp. 275-278, April 2000.
[48] K. Ogata, Modern Control Engineering, 5th ed., New Jersey: Prentice Hall, 2010.
[49] N. W. Miller, J. J. Sanchez-Gasca, W. W. Price and R. W. Delmerico, "Dynamic modeling of GE 1.5 and 3.6 MW wind turbine-generators for stability simulations," 2003 IEEE Power Engineering Society General Meeting (IEEE Cat. No.03CH37491), Toronto, Ont., 2003, pp. 1977-1983 Vol. 3.
[50] A. B. Birchfield, T. Xu, K. M. Gegner, K. S. Shetye and T. J. Overbye, "Grid Structural Characteristics as Validation Criteria for Synthetic Networks," in IEEE Transactions on Power Systems, vol. 32, no. 4, pp. 3258-3265, July 2017.
[51] A. Stumpf, D. Elton, J. Devlin, and H. Lovatt, “Benefits of an FPGA-based SRM controller”, in IEEE Conference on Industrial Electronics and Applications, Jun. 2014.
[52] K. Trung, E. Dekneuvel, B. Nicolle, O. Zammit, C. Van, and G. Jacquemod, “Using FPGA for real time power monitoring in a NIALM system”, in IEEE International Symposium on Industrial Electronics, May. 2013.
[53] I. Matsuo, J. Jardini, W. Hokama, L. Magrini, F. Crispino, and P. Kayano, “Fast system for analysis of protection events”, in IEEE PES Innovative Smart Grid Technologies Latin America, Oct. 2015.
[54] S. Zhou and V. Prasanna, “Accelerating Graph Analytics on CPU-FPGA Heterogeneous Platform”, in IEEE International Symposium on Computer Architecture and High-Performance Computing, Oct. 2017.
[55] X. Wei, Y. Liang, T. Wang, S. Lu, and J. Cong, "Throughput optimization for streaming applications on CPU-FPGA heterogeneous systems," in IEEE 22nd Asia and South Pacific Design Automation Conference, pp. 488-493, 2017.
[56] L. Zhao, Y. Zhou, I. Matsuo, S. Korkua and W. Lee, "The Design of a Remote Online Holistic Monitoring System for a Wind Turbine," in IEEE Transactions on Industry Applications, in press, 2019. doi: 10.1109/TIA.2019.2951088
[57] T. Cormen, C. Leiserson, R. Rivest, and C. Stein, *Introduction to Algorithms*, London: MIT Press, 2009, pp. 147-228.
[58] S. Kuo, B. Lee and W. Tian, *Real-time digital signal processing: implementations and applications,* 2nd ed., Chippenham, Wilts:John Wiley and Sons, 2006.
[59] G. Meurant, *Algorithms and complexity*, Amsterdam, NH: Elsevier, 2014.
[60] National Instruments, *Signal processing toolset: user manual*, Austin, TX: National Instruments Corporation, 2001.
[61] IEEE task force on identification of electromechanical modes, “Identification of electromechanical modes in power systems”, PES-TR15 technical report, Power and Energy Society, June 2012.
[62] T. K. Sarkar and O. Pereira, "Using the matrix pencil method to estimate the parameters of a sum of complex exponentials," in IEEE Antennas and Propagation Magazine, vol. 37, no. 1, pp. 48-55, Feb. 1995.
[63] W. Press, S. Teukolsky, W. Vetterling and B. Flannery, *Numerical recipes: the art of scientific computing*, 3rd ed., New York, NY: Cambridge University Press, 2007.
[64] D. Eberly, “Derivative approximation by finite differences,” Geometric Tools, 2016.
[65] S. H. Mneney, An introduction to digital signal processing: a focus on implementation, Aalborg, DK: River Publishers ApS, 2009.

[66] F. Salehi, A. Brahman, R. Keypour, and W. Lee, “Reliability assessment of automated substation and functional integration,” in IEEE Industry Applications Society Annual Meeting, Oct. 2016.
[67] N. Jazdi, “Dynamic calculation of the reliability of factory automation applications: industry 4.0 applications”, in IEEE International Conference on Automation, Quality and Testing, Robotics, May. 2016.
[68] M. Shooman, Reliability of Computer Systems and Networks: Fault Tolerance, Analysis, and Design, New York: John Wiley & Sons, 2002.
[69] R. Larabee and K. Schlapkohl, “Case Study/Overview of Applying an IEC 61850 Parallel Redundant Protocol Communications Network on a University Campus Power Micro Grid Distribution and Generating System”, in IEEE Conference for Protective Relay Engineers, Nov. 2017.
[70] T. Koskiahde and J. Kujala, “PTP Monitoring in Redundant Network”, in IEEE International Symposium on Precision Clock Synchronizations for Measurement, Control, and Communication, Sep. 2016.
[71] TI Designs, “Parallel Redundancy Protocol (PRP) Ethernet Reference Design for Substation Automation”, Mar. 2016.
[72] M. H. Rahman, S. Rafique, and M. S. Alam, “A fault tolerant voter circuit for triple modular redundant system”, in Journal of Electrical and Electronic Engineering, Vol. 5, No. 5, pp.149-159, Sep. 2017.
[73] H. Soltani, M. Dolatshahi, and M. Sadeghi, “Comparing the reliability in systems with triple and five modular redundancy”, in International Conference on Computer Science and Network Technology, pp. 437-442, Dec. 2016.
[74] Y. Li, Y. Li, and H. Jie, "Feedback-Based Low-Power Soft-Error-Tolerant Design for Dual-Modular Redundancy," in IEEE Transactions on Very Large Scale Integration Systems, pp. 1-5, Apr. 2018.
[75] NI White Paper, “Redundant System Reference Design for LabVIEW Real Time, LabVIEW FPGA, and CompactRIO”, Aug. 2013.
[76] I. B. M. Matsuo, L. Zhao, and W. Lee, “A CPU-FPGA heterogeneous platform-based monitoring system and redundant mechanisms,” in IEEE/IAS 54th Industrial and Commercial Power Systems Technical Conference, May 2018.
[77] I. B. M. Matsuo, L. Zhao and W. Lee, "A Dual Modular Redundancy Scheme for CPU–FPGA Platform-Based Systems," in IEEE Transactions on Industry Applications, vol. 54, no. 6, pp. 5621-5629, Nov.-Dec. 2018.
[78] U. Troppens, R. Erkens, W. Muller-Friedt, R. Wolafka, and N. Haustein, Storage Networks Explained: Basics and Application of Fibre Channel SAN, NAS, iSCSI, InfiniBand and FCoE, New York: John Wiley & Sons, 2009.
[79] A. Cooke, “The Killer-App – Combined Embedded Processors, FPGAs and Smart Software”, in IFT International Telemetering Conference Proceedings, Nov. 2016.
[80] M. Zheng, Z. Wang, and L. Li, “DAO: dual module redundancy with and/or logic voter for FPGA hardening,” in IEEE International Conference on Reliability Systems Engineering, Oct. 2015.
[81] P. Włodarczyk, S. Pustelny, D. Budker, and M. Lipiński, “Multi-channel data acquisition system with absolute time synchronization”, Elsevier Nuclear Instruments and Methods in Physics Research - Section A: Accelerators, Spectrometers, Detectors and Associated Equipment, vol.763, pp. 150-154, Nov. 2014.

[82] J. Kurose and K. Ross, Computer networking: a top-down approach, 7th ed., Pearson, 2017.
[83] Rapid, “DC Power Supply”, Available: https://www.rapidonline.com/pdf/554305_v1.pdf . [Accessed: 05-Jun-2018].
[84] National Instruments, “cRIO-9039 CompactRIO Controller”, Available: http://www.ni.com/en-us/support/model.crio-9039.html . [Accessed: 05-Jun-2018].
[85] Xilinx, “Xilinx Kintex 7 325-T FPGA”, Available: https://www.xilinx.com/products/silicon-devices/fpga/kintex-7.html . [Accessed: 05-Jun-2018].
[86] Trimble, “ Trimble GPS Antennas”, Available: http://www.trimble.com/embeddedsystems/pdf/022542-024_gps_antenna_ds_1210_us_lr.pdf . [Accessed: 05-Jun-2018].
[87] Seagate, “Business Storage 4-Bay NAS”, Available: https://www.seagate.com/support/external-hard-drives/network-storage/business-storage-4-bay-nas/ . [Accessed: 05-Jun-2018].
[88] Netgear, “Managed Switch GS108E”, Available: https://www.netgear.com/business/products/switches/web-managed/GS108E.aspx . [Accessed: 05-Jun-2018].
[89] IEEE Standard for Synchrophasor Measurements for Power Systems, IEEE Standard C37.118.1-2011, 2011.
[90] T. K. Sarkar and O. Pereira, "Using the matrix pencil method to estimate the parameters of a sum of complex exponentials," in IEEE Antennas and Propagation Magazine, vol. 37, no. 1, pp. 48-55, Feb. 1995.

APPENDIX A – ENBW VALUES OF TAPERED WINDOW FUNCTIONS

References [58] and [65] provide more details of possible tapered window functions commonly used in signal processing. The following table shows the ENBW values of some functions. Besides the rectangle window, which has the most spectral leakage issues, the Hamming window is the one with the least ENBW among these options.

Window function	**ENBW**
Rectangle	1.0
Hanning	1.5
Hamming	1.362826
Blackman-Harris	1.708538
Exact Blackman	1.693699
Blackman	1.726757
Blackman Nuttall	1.9761117
Flat Top	3.770246506303

APPENDIX B – TEXAS SYNTHETIC GRID PARAMETERS

PARAMETERS OF THE 161 KV TRANSMISSION LINES ON A 100 MVA BASE

From	To	R (p.u)	X (p.u)	B (p.u)
RALLS 1 2	RALLS 2	0.006	0.024	0.011
SILVERTON	RALLS 2	0.039	0.171	0.08
CHILDRESS	SILVERTON	0.019	0.079	0.04
CHILDRESS	MEMPHIS	0.023	0.099	0.046
MEMPHIS	PH 6	0.019	0.083	0.039
PH 2 1	PH 6	0.02	0.089	0.041
PH 5	PH 2 1	0.01	0.045	0.021
PH 2 1	PH 3	0.012	0.053	0.026
PH 4 1	PH 5	0.012	0.051	0.024
PH 1	PH 2 1	0.01	0.042	0.021
WHITE DEER	PH 3	0.014	0.058	0.029
WHITE DEER	WHEELER	0.025	0.105	0.053
PH 1	WHITE DEER	0.005	0.023	0.011
WHEELER	MIAMI 1	0.012	0.053	0.025

PARAMETERS OF THE 500 KV TRANSMISSION LINES ON A 100 MVA BASE

From	To	R (p.u)	X (p.u)	B (p.u)
PH 4	MIAMI	9E-04	0.011	0.718
PH 2	MIAMI	0.001	0.013	0.868
PH 4	RALLS 1	0.003	0.031	2.038
MIAMI	DENTON	0.01	0.1	3
MIAMI	WICHITA FALLS	0.033	0.043	2.3

PARAMETERS OF THE TRANSFORMERS

From	Bus kV	To	Bus kV	R (p.u)	X (p.u)	B (p.u)	MVA
PH 4	500	PH 4 1	161	5E-04	0.05	0.0002	271
PH 2	500	PH 2 1	161	4E-04	0.035	0.0002	461
MIAMI	500	MIAMI 1	161	7E-04	0.062	0.0003	308
RALLS 1	500	RALLS 1 1	230	1E-04	0.007	6E-05	836
RALLS 1 2	161	RALLS 1 1	230	0.002	0.133	0.0009	146

APPENDIX C – COMPLEMENTARY FREQUENCY IN THE POWER SIGNAL

This appendix shows why the power signal contains the complementary frequency to the fundamental frequency when a sub-synchronous oscillation is also present in the voltage/current signals.

Take a single-phase system with a voltage and a current signal with two components each, a synchronous (fundamental frequency) and a sub-synchronous frequency component.

$$\begin{aligned} v(t) &= v_s(t) + v_{ss}(t) \\ i(t) &= i_s(t) + i_{ss}(t) \end{aligned} \tag{C-1}$$

Each component is as follows:

Voltage synchronous component:	$v_s(t) = V_s \sin(\omega_s t + \theta_s)$
Voltage sub-synchronous component:	$v_{ss}(t) = V_{ss} \sin(\omega_{ss} t + \theta_{ss})$
Current synchronous component:	$i_s(t) = I_s \sin(\omega_s t + \varphi_s)$
Current sub-synchronous component:	$i_{ss}(t) = I_{ss} \sin(\omega_{ss} t + \varphi_{ss})$

(C-2)

where:

V: Voltage amplitude

I: Current amplitude

ω: Angular frequency

θ: Angle of the voltage

φ : Angle of the current

$_s$: subscript for synchronous components (at the fundamental frequency)

$_{ss}$: subscript for sub-synchronous components

We can calculate the instantaneous power with the following equation:

$$p(t) = v(t)\, i(t) = [v_s(t) + v_{ss}(t)][i_s(t) + i_{ss}(t)] \tag{C-3}$$

which leads to:

$$p(t) = p_1(t) + p_2(t) + p_3(t) + p_4(t) \tag{C-4}$$

where:

$$\begin{aligned} p_1(t) &= v_s(t)i_s(t) \\ p_2(t) &= v_s(t)i_{ss}(t) \\ p_3(t) &= v_{ss}(t)i_s(t) \\ p_4(t) &= v_{ss}(t)i_{ss}(t) \end{aligned} \tag{C-5}$$

Take the trigonometric product relationship:

$$\sin(x)\sin(y) = \frac{1}{2}\left[\cos(x-y) - \cos(x+y)\right] \tag{C-6}$$

Applying (C-6) to (C-5), we have:

$$p_1(t) = \frac{V_s I_s}{2}\left[\cos(\theta_s - \varphi_s) - \cos(2\omega_s t + \theta_s + \varphi_s)\right] \tag{C-7}$$

$$p_2(t) = \frac{V_s I_{ss}}{2}\left[\cos\left((\omega_s - \omega_{ss})t + \theta_s - \varphi_{ss}\right) - \cos\left((\omega_s + \omega_{ss})t + \theta_s + \varphi_{ss}\right)\right] \tag{C-8}$$

$$p_3(t) = \frac{V_{ss} I_s}{2}\left[\cos\left((\omega_{ss} - \omega_s)t + \theta_{ss} - \varphi_s\right) - \cos\left((\omega_s + \omega_{ss})t + \theta_{ss} + \varphi_s\right)\right] \tag{C-9}$$

$$p_4(t) = \frac{V_{ss} I_{ss}}{2}\left[\cos(\theta_{ss} - \varphi_{ss}) - \cos(2\omega_{ss} t + \theta_{ss} + \varphi_{ss})\right] \tag{C-10}$$

For a three-phase system, considering the above equations are valid for phase A, the same equations will apply for phases B and C with a phase difference of $-120°$ added to the voltage and current angles of phase B and a phase difference of $+120°$ added to the voltage and current angles of phase C, e.g., $\theta_s \rightarrow \theta_s - 120°$ for phase B. This is valid for both the synchronous and sub-synchronous components, therefore, it is valid for θ_s, φ_s, θ_{ss} and φ_{ss}.

The following equation is the three-phase instantaneous power:

$$p_{3\emptyset}(t) = p_a(t) + p_b(t) + p_c(t) \tag{C-11}$$

Applying equations (C-7) through (C-10) to each phase considering the phase differences in each, we can calculate $p_a(t)$, $p_b(t)$ and $p_c(t)$ for each phase using (C-4). Applying the results to (C-11), we have:

$$p_{1_{3\emptyset}}(t) = \left[\frac{3V_s I_s}{2}\cos(\theta_s - \varphi_s) + \frac{3V_{ss} I_{ss}}{2}\cos(\theta_{ss} - \varphi_{ss})\right] + \cdots$$
$$\cdots \left[\frac{3V_s I_{ss}}{2}\cos\big((\omega_s - \omega_{ss})t + \theta_s - \varphi_{ss}\big) + \frac{3V_{ss} I_s}{2}\cos\big((\omega_s - \omega_{ss})t - \theta_{ss} + \varphi_s\big)\right] \quad \text{(C-12)}$$

In equation (C-12), the terms inside the first pair of brackets are the three-phase DC component in the presence of a sub-synchronous oscillation. The terms inside the second pair of brackets are the three-phase AC component, which has an angular frequency of $(\omega_s - \omega_{ss}) = (2\pi f_s - 2\pi f_{ss}) = 2\pi(f_s - f_{ss})$.

In the presence of a sub-synchronous oscillation, the power will then have a frequency component of:

$$f_{SSO,power} = (f_s - f_{ss}) \quad \text{(C-13)}$$

As we can see, a component with a frequency complementary to the fundamental frequency is present in the power signal. Let $f_s = 60$ Hz and $f_{ss} = f_{SSO}$ and we have the same equation presented in chapter 4, herein repeated:

$$f_{SSO,power} = 60 - f_{SSO} \quad \text{Equation (4-26)}$$

where: $f_{SSO} = f_{SSO,voltage/current}$